COLD-CRACKING CONTROL
IN
LOW-ALLOY STEEL WELDS

by

Vivek Pavaskar, B. Tech.

A Thesis

Submitted to the School of Graduate Studies

in Partial Fulfilment of the Requirements

for the Degree of

MASTER OF ENGINEERING

McMaster University

Hamilton, Ontario

September 1979

COLD-CRACKING CONTROL
IN
LOW-ALLOY STEEL WELDS

MASTER OF ENGINEERING (1979) McMASTER UNIVERSITY
(Metallurgy and Materials Science) Hamilton, Ontario

TITLE: Cold-Cracking Control in Low-Alloy Steel Welds

AUTHOR: Vivek Pavaskar, B.Tech. (Indian Institute of Technology, Bombay)

SUPERVISOR: Dr. J. S. Kirkaldy

NUMBER OF PAGES: xiii, 148

ABSTRACT

HAZ microstructure, stress and hydrogen level are the fundamental factors influencing the cold cracking susceptibility of the HAZ. Implant testing at various hydrogen levels over a range of steel compositions and heat inputs shows how the HAZ microstructure and hydrogen level influence the critical stress necessary for cold-cracking.

Based on implant test data, a correlation formula predicting the critical stress necessary for cold cracking for given HAZ hardness, % martensite in the HAZ and hydrogen level, is proposed. Employing this correlation, together with prediction of % martensite in the HAZ and HAZ hardness, based on heat transfer calculations, % martensite-composition-cooling rate relations and hardness-composition-cooling rate relations, an algorithm which can predict the critical stress necessary for cracking for given implant composition, cooling rate and hydrogen level, is constructed.

This method of predicting the critical stress necessary for cold cracking is an improvement over the existing regression formulas for estimating cold-cracking susceptibility.

This formula has been successfully adapted to predict cold-cracking susceptibility data as obtained through other tests such as rigid restraint, and to recommend preheat levels necessary to avoid cold-cracking. Development and use of an implant testing machine with an automatic welding and loading facility is also reported.

ACKNOWLEDGEMENTS

The author is indebted to his supervisor, Dr. J. S. Kirkaldy, for suggesting the problem dealt with here, and for his continuous guidance throughout the course of this work. Thanks are also due to many of the staff and graduate students in the Department of Metallurgy and Materials Science, for their advice and assistance. I would also like to thank the technical staff of the Department of Metallurgy and Materials Science, and the machine shop for their assistance in developing the Implant Testing Equipment. Thanks are also due to Mrs. Sue Saracini for the excellent typing of this thesis.

Financial support of the Natural Sciences and Engineering Research Council of Canada is gratefully acknowledged.

TABLE OF CONTENTS

LIST OF TABLES

LIST OF FIGURES

CHAPTER 1

INTRODUCTION

Hydrogen induced cold-cracking has been one of the major problems in welding steels. Cracks of this type can take many forms, although they have some general characteristics and are influenced by common basic factors.

As the name implies, these cracks form at low temperatures -- generally below 200°C, and often exhibit a delay phenomenon. Even after the weld has cooled to room temperature, there may be a further lapse of time ranging from a few minutes to several hours.

Cold-cracks are not tolerated in a structure, and since they are often difficult to detect and expensive to repair, it becomes essential for the fabricator to take precautions during welding to prevent their formation.

Even though the general causes of hydrogen cracking and the means of preventing these cracks are known, recent industrial surveys have shown that cold-cracking is still widely encountered, indicating that the ability to satisfactorily predict cold-cracking susceptibility has not been developed.

Hence, development of a reliable, quick and economic method for predicting hydrogen cracking in a real welded joint is desirable to determine when conventional welding techniques can be used without the likelihood of failure from hydrogen cracking. In addition, needless expense of preheating and low-hydrogen techniques could be avoided; re-

sulting welds would be more reliable, and welding repair costs would be lower.

Chapter 2 of the present study reviews the existing linear empirical weldability formulas and demonstrates the superiority of Implant Testing over other weldability tests for assessing cold-cracking susceptibility in terms of the Lower Critical Implant Fracture Stress (σ_{CR}).

In Chapter 3, published implant test data is analysed for the influence of Heat Affected Zone (HAZ) microstructure on the Lower Critical Implant Fracture Stress (σ_{CR}) and a modified correlation formula for σ_{CR} is proposed with HAZ % martensite and HAZ hardness as parameters. The influence of hydrogen level on σ_{CR} is also incorporated into the correlation formula on the basis of published implant test data for various hydrogen levels, and the role of hydrogen in influencing σ_{CR} is analysed by calculating the combinations of stress intensity and hydrogen level in the region of maximum triaxiality in front of the notch of the implant specimen, for different HAZ microstructures, bulk hydrogen levels, and the corresponding σ_{CR}.

Chapter 4 presents the method of predicting the HAZ % martensite and HAZ hardness by using heat transfer calculations, % martensite-composition - cooling rate relations, and hardness-composition-cooling rate relations. Comparisons between predicted and experimentally observed HAZ % martensite and hardness show a good agreement. Together with the correlation formula proposed in Chapter 3, σ_{CR} is predicted for given plate thickness, plate composition, preheat level and residual hydrogen level. It is shown that predicted σ_{CR} effectively serves as a parameter for observed weld cracking % over a wide range of low-alloy steel com-

positions.

In Chapter 5, employing a criterion that the reaction stress developed in the weld due to joint restraint should not exceed the Lower Critical Implant Fracture Stress (σ_{CR}) for the same welding conditions, preheat levels necessary to prevent cold-cracking are predicted. The influence of preheat on σ_{CR} is predicted in terms of the contribution of preheat towards altering the HAZ microstructure and the residual hydrogen level. Hydrogen diffusion calculations are used for predicting the residual hydrogen level, on the basis of difference in cooling time between 450°C and 100°C for thermal conditions with and without preheat. Assuming that the intensity of restraint varies linearly with the plate thickness, preheat levels for fillet welds are predicted and compared with the recommended (British Welding Standard) preheat levels over a wide range of plate thicknesses, heat inputs and hydrogen levels.

Chapter 6 describes the development and use of an implant testing machine with automatic welding and loading facility. Details of standardising the implant testing are presented. Results of the preliminary experiments carried out on two steels under the same welding conditions are reported.

Conclusions of the present study are listed in Chapter 7.

CHAPTER 2

ASSESSING THE COLD CRACKING SUSCEPTIBILITY OF THE HEAT-AFFECTED ZONE (HAZ) IN STEEL WELDMENTS

2.1 Weldability Formulas for Assessing Cold-Cracking Susceptibility

Since Dearden and O'Neill[1] suggested a carbon equivalent formula in 1940, a number of weldability formulas have been proposed to assess cold-cracking susceptibility. The formulas of this type are intended to:

1) estimate the weldability of a newly developed steel with minimum expense and work;

2) to serve as a guide to safe welding procedures;

3) to provide directions for developing new types of steel.

All the formulas developed relate crack susceptibility to the hardenability of the steel. A limit of 350 D.P.N. on maximum hardness in the Heat Affected Zone (HAZ) was first suggested by Dearden and O'Neill[1] as a criterion for crack-free welds. Taking this limit on the maximum HAZ hardness, various researchers have recommended maximum carbon-equivalents for welding without having to take precautions.

Winterton[11] has presented an excellent review of various carbon-equivalent (C.E.) formulas based on correlations with HAZ cracking and weldability data. Table I shows various formulas proposed.

Some of the qualifications to be noted are:

1) various weldability tests (Reeve, bend angle, bead-on-plate, controlled thermal severity (CTS)) have been used for

assessing weldability;

2) maximum allowable HAZ hardness criterion has been used to suggest the maximum C.E. that could be welded without precautions;

3) different tests suggest different carbon equivalents and prescribe different C.E. limits for good weldability;

4) different tests offer different restraint levels. Hence, carbon equivalents derived from these tests only help to arrange different steels in an "order of weldability" for the restraint characteristic of each test.

Based on his proposed carbon equivalent (Formula 10) scale, Winterton[11] suggested welding precautions as shown in Table II.

Later, Bradstreet[13] conducted a series of controlled thermal severity (CTS) tests and assigned a weldability index based on the thermal severity number (TSN) required to cause cracking (see Table III). He expressed the weldability index in terms of the critical cooling rate at 300°C, required for cracking. He further suggested an approximate relationship between carbon equivalent (Formula 10) and weldability index for low hydrogen electrodes (see Table IV). Finally, with a relation between

1) Heat Input (E)

2) Thermal Severity Number (N)

3) Initial Plate Temperature Factor (T = 300 - t°C)

4) Cooling Rate at 300°C (R)

given by

$$\frac{1}{\sqrt{R}} = \frac{E + 1000N}{54T\ (1 + T/1000)(N + 1/2)} \qquad (12)$$

TABLE I

Formulas Developed to Assess Cold-Cracking of HAZ in Steel Weldments

Authors	Test Method	Carbon Equivalent	Carbon Equivalent limit for good weldability
1. Dearden and O'Neill[1]	Reeve Test on 1/2" plates	$C + \frac{Mn}{6} + \frac{Ni}{15} + \frac{Cr}{5} + \frac{Mo}{4}$ (1) To be used with DPN=1200xC.E.-200 (2)	0.45
2. Kihara, Suzuki and Tamura[2]	Modification to carbon-equivalent (Formula (1))	$C + \frac{Si}{24} + \frac{Mn}{6} + \frac{Ni}{15} + \frac{Cr}{5} + \frac{Mo}{4}$ (3) To be used with $H_{max}=(666 \times C.E. + 40)\pm 40$ (4)	
3. Voldrich, Martin and Harder[3]	Bend angle on notched bead slow bend test, 1/2", 3/4" and 1" plates	$C + \frac{Mn}{4} + \frac{Si}{4}$ (5)	0.54
4. William, Roach, Martin and Voldrich[4]	Bead-on-plate cracking	$C + \frac{Mn}{4} + \frac{Si}{4}$ (5)	0.38 0.42 150°F 0.57 250°F
5. Voldrich and Harder[5]	Bead-on-plate cracking	$C + \frac{Mn}{6}$ (6)	0.60 1/4" 0.50 1/2" 0.45 1" 0.40 2"
6. Sims and Banta[6]	Bead-on-plate	$C + \frac{Mn}{7} + \frac{Si}{25} + \frac{Cr}{51} + \frac{Mo}{31} + \frac{V}{13}$ (7)	

continued ....

Authors	Test Method	Carbon Equivalent	Carbon Equivalent limit for good weldability
7. Reeve[7]	CTS tests	$C + \frac{Mn}{6} + \frac{Ni}{15} + \frac{Cr}{5} + \frac{Mo}{4}$ (1)	0.45
8. Cottrell and others (8, 9)	CTS cracking and dilatometric changes (start of Transformation)	$\frac{930 - MS}{540} = C\% + \frac{Mn}{9} + \frac{Si}{27} + \frac{Ni}{18} + \frac{Cr}{14} + \frac{Mo}{27}$ (8)	
9. Bradstreet[10]	CTS cracking and end of Transformation Temperature	$C + \frac{Mn}{20} + \frac{Ni}{15} + \frac{Cr + Mo + V}{10}$ (9)	
10. Winterton[11]	CTS cracking and 90% Transformation Temperature	$C + \frac{Mn}{a} + \frac{Ni}{20} + \frac{Cr}{10} - \frac{Mo}{50} - \frac{V}{10} + \frac{Cu}{40}$ (10) a changing with carbon content	See Table II
11. IIW Commission IX Subcommission G Technical Report 1967 (12)		$C + \frac{Mn}{6} + \frac{Cr + Mo + V}{5} + \frac{Ni + Cu}{15}$ (11)	

TABLE II

Welding Precautions for Various Carbon Equivalents

Carbon Equivalent	Welding Procedure
<0.40	No precautions .
0.40-0.48	Weldable with: (a) ordinary electrodes and low preheat (200-400°F) or (b) low hydrogen electrodes
0.48-0.55	Weldable with: (a) ordinary electrodes and moderate preheat (400-700°F) or (b) austenitic electrodes or (c) gas metal arc welding
>0.55	Weldable with: (a) low hydrogen electrodes and moderate and high preheat or (b) austenitic electrodes or (c) gas-metal-arc welding

and the critical cooling rate at 300°C as per weldability indices, he prescribed welding conditions for prevention of cold-cracking, as shown in Table V.

Based on the HAZ hardness criterion for good weldability, Bailey[14] later developed a system to determine safe welding procedures in terms of critical cooling rate at 300°C. Figure 1 shows a nomogram illustrating his system. It is important to note that Bailey has introduced the effect of hydrogen by taking 350 D.P.N. as the critical hardness for normal welding procedures, 400 D.P.N. for low hydrogen processes, and 450 D.P.N. for very low hydrogen processes.

Experience with HAZ cold-cracking has shown that susceptibility of HAZ to cracking is mainly governed by:

1) microstructural characteristics of the HAZ,

2) stress level in the HAZ,

3) hydrogen level in the HAZ.

Thus, the HAZ cracking susceptibility has to be assessed in terms of the influence of HAZ microstructural characteristics, stress level and hydrogen level.

Bradstreet's[13] welding procedures based on CTS tests and the Bailey[14] nomogram based on the maximum hardness criterion, are lacking in a quantitative assessment of the susceptibility of HAZ toward cracking for different stress and hydrogen levels in the HAZ.

Ito and Bessyo[15,16] conducted a series of y groove restraint tests and proposed an empirical parameter (Pw) based on the correlation between % weld cracking, and plate composition, plate restraint, and hydrogen level. This cracking parameter (Pw) which is designed to

TABLE III

Weldability Index Proposed by Bradstreet

WELDABILITY INDEX FROM CTS TESTS

Critical Cooling Rate (at 500°C) above which cracks occur (°C/sec)	*TSN for cold cracking in CTS Test (1/4" leg length fillets)* *Present with TSN*	*Absent with TSN*	*Weldability*
Over 32	—	12 and under	A
20—32	12 and over	8 and under	B
11—20	8 and over	6 and under	C
6—11	6 and over	4 and under	D
4—6	4 and over	3 and under	E
2—4	3 and over	2 and under	F
Under 2	2 and over	—	G

TABLE IV

Relation Between Carbon Equivalent and Weldability Index for Low Hydrgen Electrodes

WELDABILITY INDEX FROM STEEL COMPOSITION

(for low hydrogen electrodes)

*Range of carbon equivalents, % *	*Weldability Index*
Up to 0.40	A
0.41—0.45	B
0.46—0.50	C
0.51—0.55	D
0.56—0.60	E
0.61—0.65	F
More than 0.65	G

TABLE V

Welding Procedure for Prevention of Cold-Cracking

WELDING CONDITIONS FOR THE PREVENTION OF COLD CRACKING

Joint Severity	Weldability Index of steel	Minimum plate temperature (°F)* for welds made with the following arc energies (Kilojoules/inch)						
		20	30	40	50	60	70	80
TSN 2..... (Two 1/4 in. plates, etc.)	A	W	W	—	—	—	—	—
	B	W	W	—	—	—	—	—
	C	25	W	—	—	—	—	—
	D	125	W	—	—	—	—	—
	E	225	100	—	—	—	—	—
	F							
TSN 3..... (Two 3/8 in plates, or three 1/4 in. plates, or 1/4 in. on 1/2 in. plate, etc.)	A	W	W	W	W	—	—	—
	B	25	W	W	W	—	—	—
	C	150	0	W	W	—	—	—
	D	225	125	25	W	—	—	—
	E	325	225	125	25	—	—	—
	F							
TSN 4..... (Two 1/2 in. plates, or three 1/3 in. plates, or 1/4 in. on 3/4 in. plate etc.)	A	W	W	W	W	W	W	W
	B	25	W	W	W	W	W	W
	C	125	W	W	W	W	W	W
	D	225	100	25	W	W	W	W
	E	275	175	75	25	W	W	W
	F	350	275	200	125	75	0	W
TSN 6..... (Two 3/4 in. plates, or three 1/2 in. plates, or 1/2 in. on 1 in. plate, etc.)	A	100	W	W	W	W	W	W
	B	225	125	W	W	W	W	W
	C	300	200	0	W	W	W	W
	D	350	275	200	125	50	W	W
	E	400	350	300	250	200	150	100
	F							
TSN 8..... (Two 1 in. plates, or three 2/3 in. plates, or 1/2 in. on 1-1/2 in. plate, etc.)	A	100	W	W	W	W	W	W
	B	175	75	W	W	W	W	W
	C	275	175	100	25	W	W	W
	D	350	275	200	125	75	25	W
	E	375	325	275	200	150	100	50
	F	450	400	350	300	275	225	175
TSN 12..... (Two 1 1/2 in. plates, or three 1-in. plates, or 1 in. on 2 in. plate, etc.)	A	175	75	0	W	W	W	W
	B	250	175	100	25	W	W	W
	C	325	275	200	150	100	25	W
	D	400	350	300	250	200	150	100
	E	425	375	350	300	250	225	175
	F	475	450	400	375	350	325	275
TSN 16..... (Two 2-in. plates, or three 1-1/3 in. plates, or 1-in. on 3 in. plate, etc.)	A	175	75	25	W	W	W	W
	B	250	200	125	75	50	0	W
	C	350	300	250	225	175	125	75
	D	400	375	325	300	250	225	200
	E	450	400	375	350	325	275	250
	F	475	450	425	425	400	375	350
TSN 24..... (Two 3-in. plates, or three 2 in. plates, or any larger joint)	A	175	75	25	W	W	W	W
	B	250	200	125	75	50	0	W
	C	350	300	250	225	175	150	125
	D	400	375	325	300	275	250	250
	E	450	400	375	350	350	325	300
	F	475	450	425	425	400	400	375

* Temperatures are quoted in 25°F steps.
W denotes a temperature below —50°F.

Poor Copy

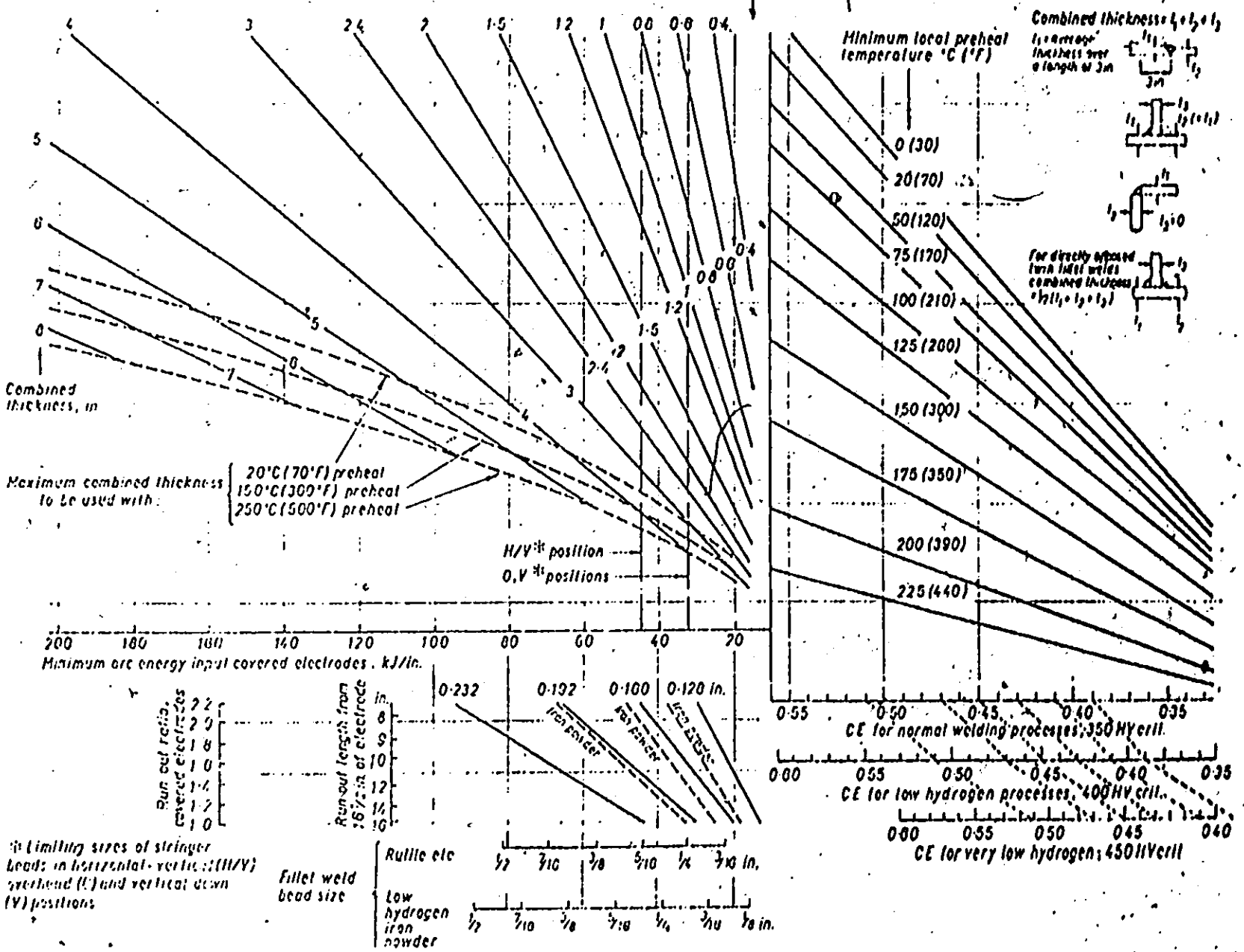

Figure 1 Bailey's Nomogram of Safe Welding Procedures for C-Mn Steels

assess the influence of plate composition, HAZ stress and HAZ hydrogen levels, is given by:

$$Pw = C + \frac{Si}{30} + \frac{Mn}{20} + \frac{Ni}{60} + \frac{Cr}{20} + \frac{Mo}{15} + \frac{V}{10} + 5B + \frac{H}{60} + \frac{K}{40x10^3} \qquad (13)$$

where K is the intensity of restraint.

Relating Pw to the critical time necessary between 300°C and 100°C to avoid cracking, Ito-Bessyo suggested a system to determine safe welding procedures with the criterion that for given Pw, the actual time of cooling between 300°C and 100°C should be greater than the critical time necessary to avoid cracks (see Figure 2).

The Ito-Bessyo[15,16] system is indeed an advance over that offered by Bailey since:

1) it has been observed that HAZ hardness alone cannot fully characterize the HAZ microstructural condition for assessing its cracking susceptibility (see Figures 6 and 7),
2) it includes the influence of hydrogen level as well as stress level on the cracking susceptibility.

However, the Ito-Bessyo approach is completely linear and empirical. In order to get the correct understanding of the problem, we must be able to relate and explain the difference in the HAZ cracking susceptibility in terms of:

1) the microstructural characteristics of the HAZ, like % of various HAZ microconstituents, maximum HAZ hardness, HAZ toughness, etc.,
2) specific role of hydrogen in assisting cracking,
3) influence of stress conditions.

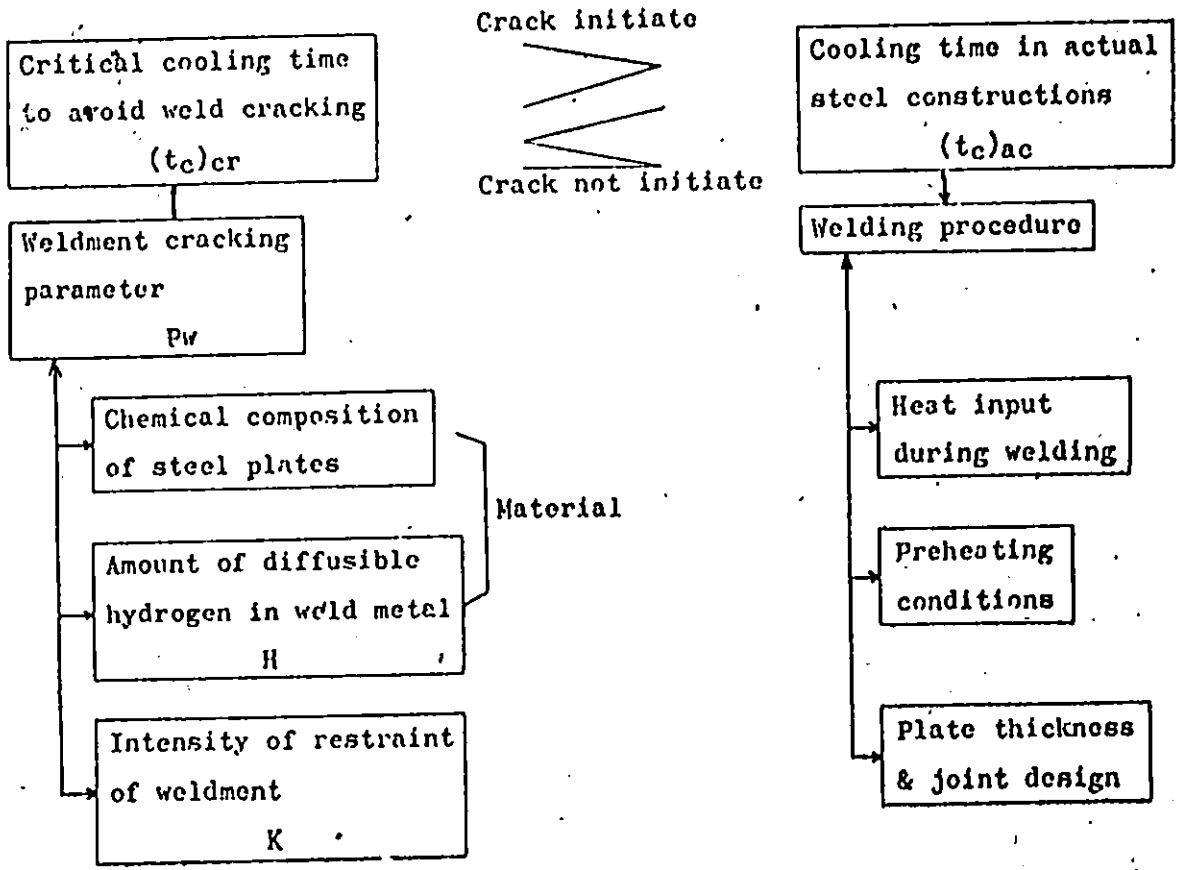

Figure 2 Ito-Bessyo system For Determining Safe Welding Procedures (16)

2.2 Implant Testing for Assessing Cold-Cracking Susceptibility

Several research workers have carried out tests with a simulated HAZ. However, a simulated HAZ seems to depart considerably from the actual HAZ conditions in regard to microstructural as well as hydrogen distribution characteristics.

Of the variety of laboratory weldability tests like bead-on-plate, cruciform, Leighih, Tekken, CTS, RRC, TRC, simulated HAZ notch tensile tests, etc., the Implant Test has emerged as the most successful laboratory test for quantitative assessment of HAZ cold-cracking susceptibility in terms of HAZ microstructure, stress condition and hydrogen level.

The Implant Test introduced by Grajon[17] involves implanting a cylindrical specimen of the steel to be tested into a mild steel plate by welding, as shown in Figure 3. The cylindrical specimen has a circular notch (see Figure 4) which is located in such a way that, upon welding, it lies in the HAZ. After welding, the specimen is subjected to a constant tensile load and the time to fracture is noted. As the tensile load is decreased (see Figure 5), the time to fracture increases and the tensile stress at the notch section, below which fracture does not occur for 24 hours, is reported as the lower critical implant fracture stress (σ_{CR}).

σ_{CR} is the measure of the susceptibility of the HAZ towards cracking. The advantage of the implant test over other laboratory weldability tests lies in the fact that this test allows quantitative assessment of the cold-cracking susceptibility of the real HAZ, in terms of

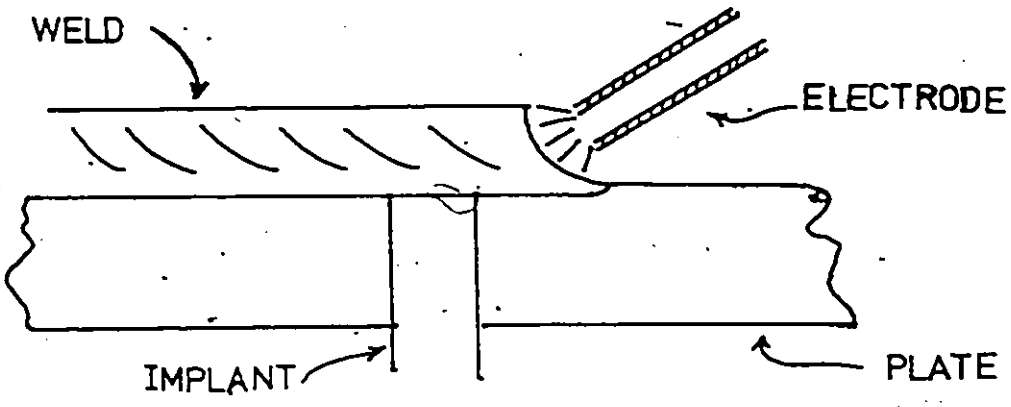

Figure 3 Implanting Steel Specimen by Welding

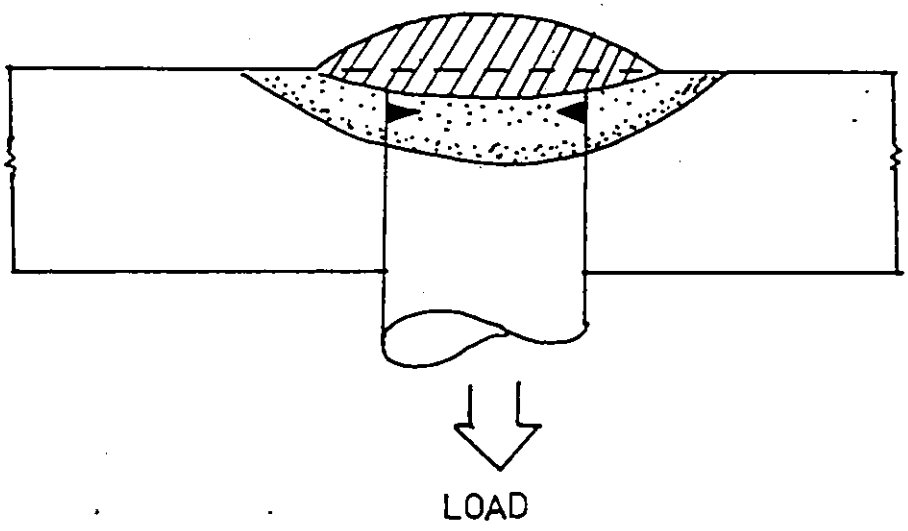

Figure 4 Schematic Diagram Showing Implant Test

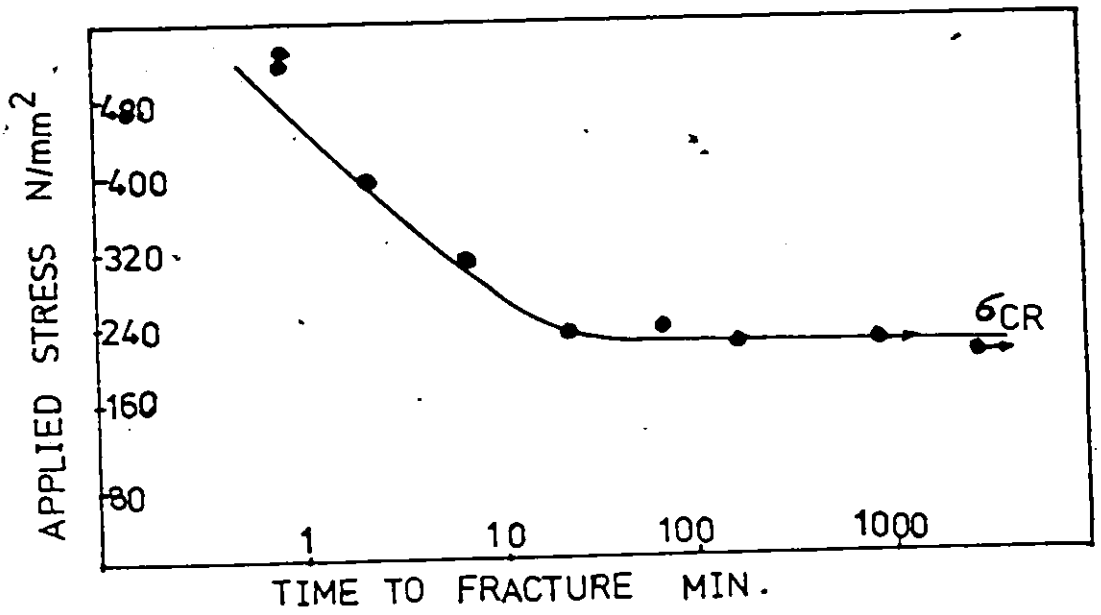

Figure 5 A Typical Stress vs Fracture Time Curve

For an Implant Test

the lower critical fracture stress, below which cracking will not occur for the given HAZ microstructural characteristics and hydrogen level.

Implant testing of steels of various compositions at different welding heat inputs, preheat levels, plate thicknesses and hydrogen levels offers a complete quantitative evaluation of the influence of the HAZ microstructural characteristics and hydrogen level on σ_{CR}.

Correlations based on implant test data can allow us to predict the HAZ cold-cracking susceptibility for given welding parameters (heat input, preheat), plate composition, joint design and restraint, and hydrogen level.

CHAPTER 3

INFLUENCE OF HAZ MICROSTRUCTURE ON THE LOWER CRITICAL IMPLANT FRACTURE STRESS

3.1 Correlation Formulas Based on Implant Test Data

Since 1969 when H. Grajon[17] introduced the idea of implant testing, Christensen et al, Augland et al, Hart and Watkinson, and Savage et al[18] have carried out implant testing on various steels.

In 1970, Augland et al[19] reported that the σ_{CR} correlates very well with C + Mn/8, after testing C/Mn steels with carbon ranging from 0.049 to 0.218% and manganese from 0.92 to 1.47%.

In 1971, Christensen[20] presented a correlation between HAZ hydrogen level and σ_{CR} as:

$$\sigma_{CR} = A - B \log [H] \qquad (14)$$

where A and B depend on HAZ microstructural characteristics, and H is the hydrogen level in ppm measured by IIW procedure (IIW/IIS-315-68).

Hart and Watkinson[21], in 1972, reported a correlation as follows:

$$\sigma_{CR} = 923 - 2250(C\%) - 0.28(\text{yield strength } N/mm^2) + 40(\text{arc energy kJ/mm}) - 3.1(\text{plate thickness mm}) \qquad (15)$$

In 1973,[22,23] Christensen et al, based on their implant test data, suggested a correlation

$$\sigma_{CR} = a + b(1 - m)^{1/2} \qquad (16)$$

where a and b are functions of hydrogen level, and m is the martensite fraction in the vicinity of the fusion boundary.

Combining Equations (14) and (16), they presented the correlation as:

$$\sigma_{CR} = a^* - b^* \log [H] + a^{**}(1 - m)^{1/2} - b^{**}(1 - m)^{1/2} \log [H] \quad (17)$$

This correlation is very useful as it relates HAZ microstructural characteristic and hydrogen level in regard to their combined influence on σ_{CR}.

3.2 Influence of HAZ % Martensite and Hardness on σ_{CR}

Even though a general increase in HAZ hardness decreases the σ_{CR} it is known that HAZ hardness alone cannot fully characterize the HAZ condition for assessing HAZ cracking susceptibility (see Figures 6 and 7).

Christensen's[23] correlation based on % M in the vicinity of the fusion boundary, may be explained in terms of the mechanism of the mixed structure failure, advanced by Berry and Allan.[24] The sequence of events that they outlined to explain their observation that the HAZ cracks at the intersection of the areas of mixed structure of martensite and high temperature transformation product, is as follows:

1) Plastic flow occurs in bainitic-ferrite and dislocations pile up against the lath boundary.
2) Martensite attempts to relieve the stress built up due to pile up in bainitic ferrite.
3) Dislocations in martensite move in several intersecting systems (i.e., work hardening occurs rapidly) and no further relief of stress can be achieved.

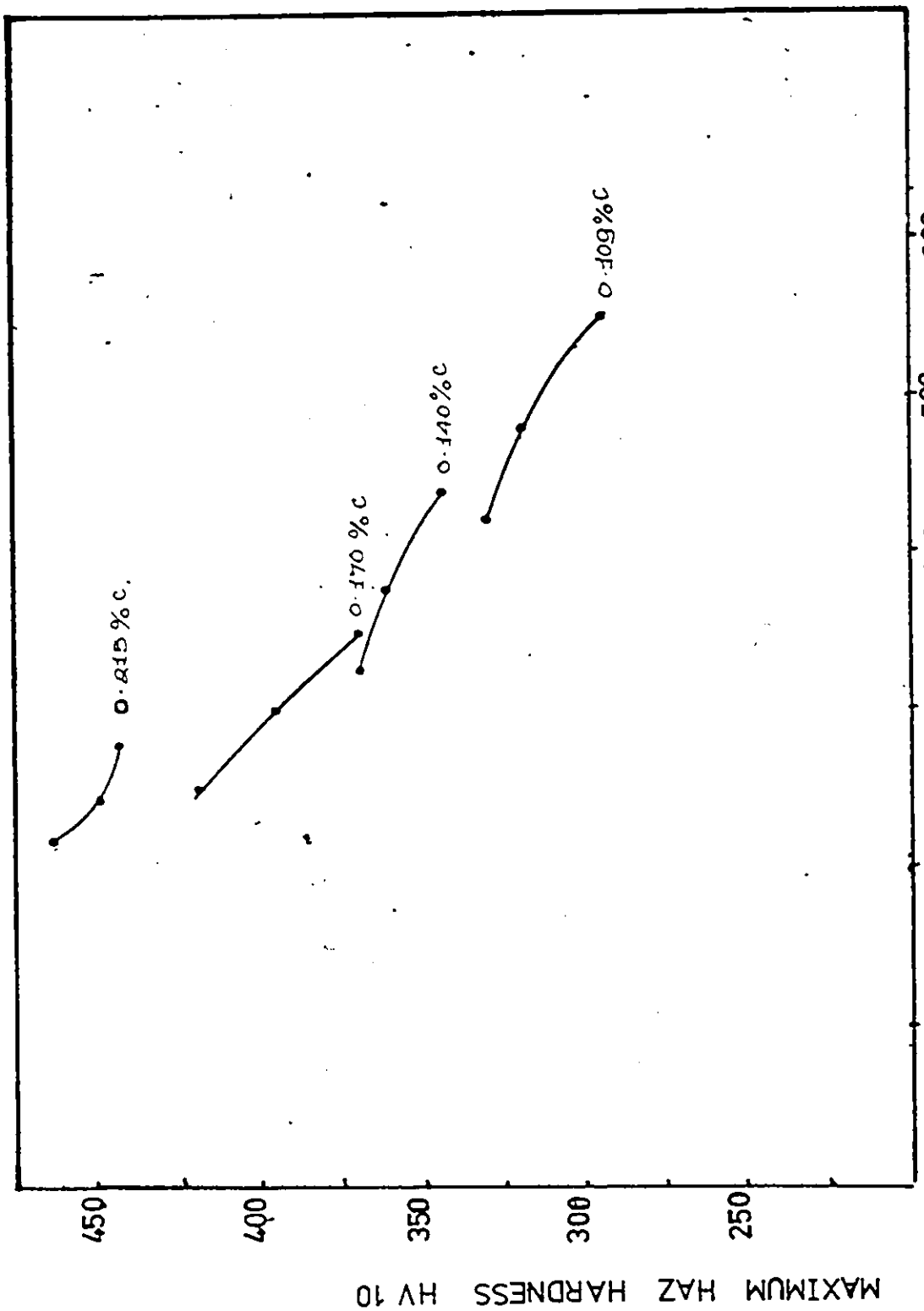

Figure 6 Variation of σ_{CR} with HAZ Hardness [23]

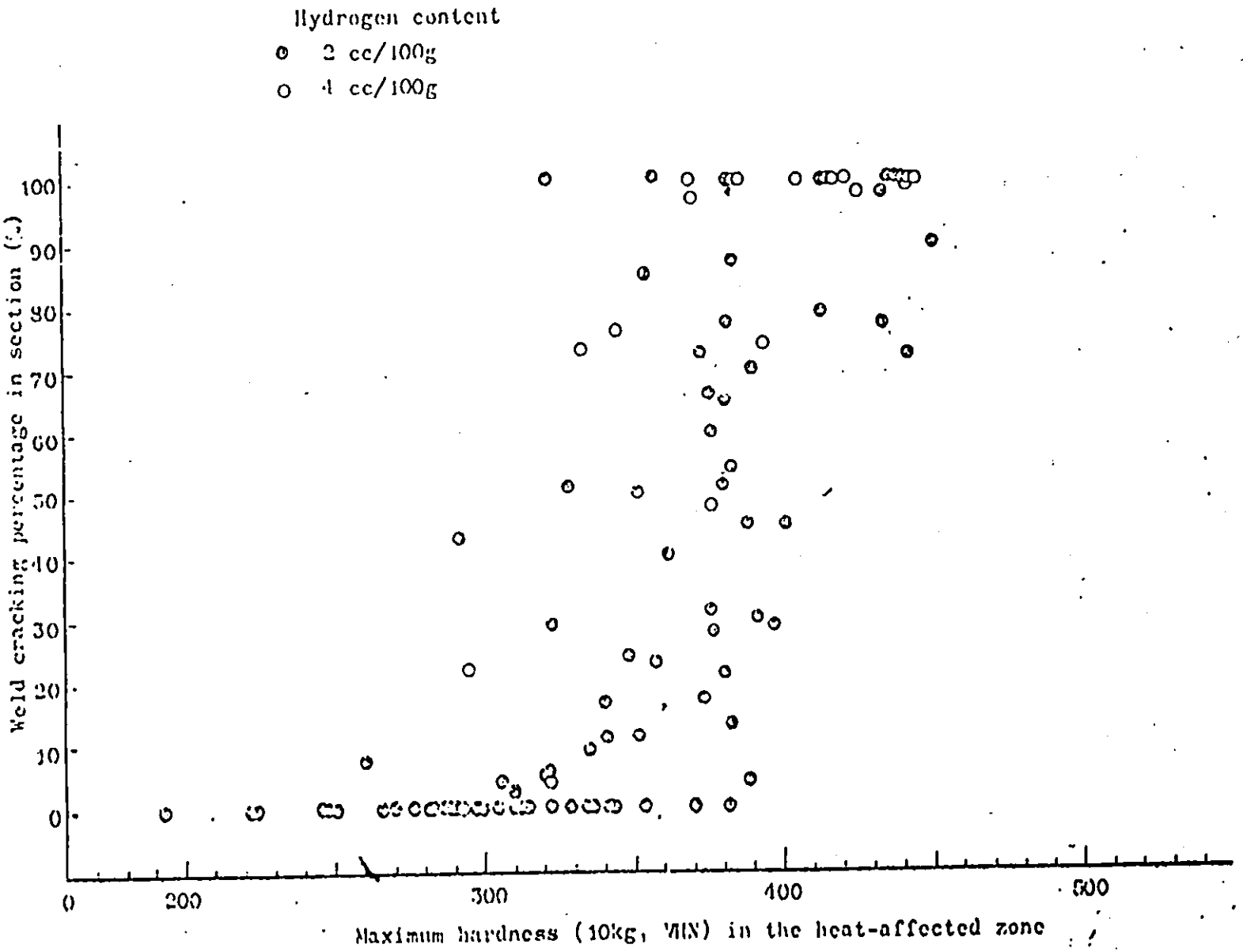

Figure 7. % Weld Cracking and HAZ Hardness Plot (15)

4) Fracture starts on or near lath boundary (possibly by the coalescence of edge dislocations in bainitic ferrite), and follows such boundaries in an "unzipping" motion.

Thus, martensite can be said to be contributing towards lowering of HAZ fracture toughness by:

1) providing stress concentration sites at the boundary separating the martensite and high temperature transformation product;

2) raising the HAZ yield strength level.

For a given composition, an increase in the % martensite increases the HAZ hardness and HAZ yield strength. However, the HAZ hardness depends both on the % martensite and the hardness of the martensite itself. Since the hardness of martensite is affected strongly by its carbon content, we can see that % martensite by itself cannot be an adequate measure of the HAZ yield strength level. Thus, characterization of the HAZ by % martensite alone would only partially take into account the contribution of martensite towards the lowering of the fracture toughness by raising the HAZ yield strength. Hence, both % martensite and maximum HAZ hardness (measure of HAZ yield strength) should be the correlation parameters for assessing cold-cracking susceptibility of the HAZ.

3.3 Modified Correlation Formula for σ_{CR}

From the analysis in Section 3.2, we used Christensen's[23] data on implant tests (see Table VI) to look for a correlation with % martensite as well as HAZ hardness as parameters. We observed that implant fracture stress σ_{CR} correlates very well with the HAZ INDEX given by:

TABLE VI

Christensen's Impalnt Test Data*

No.	C	Mn	Si	% Martensite	HAZ Hardness V 10kg	σ_{CR} N/mm^2	Heat Input kJ/mm
1	0.109	1.61	0.43	67	330	420	0.9
2	0.109	1.61	0.43	53	320	480	1.3
3	0.109	1.61	0.43	36	295	550	1.7
4	0.140	1.57	0.43	86	370	325	0.9
5	0.140	1.57	0.43	77	363	375	1.3
6	0.140	1.57	0.43	70	345	440	1.7
7	0.170	1.59	0.43	94	420	250	0.9
8	0.170	1.59	0.43	88	395	300	1.3
9	0.170	1.59	0.43	79	370	350	1.7
10	0.215	1.59	0.43	97	465	215	0.9
11	0.215	1.59	0.43	94	450	240	1.3
12	0.215	1.59	0.43	91	445	275	1.7

* Hydrogen level 7 ppm.

HAZ INDEX = [1565 - 10 x (% martensite) - (maximum HAZ hardness)] (18)

where HAZ hardness is measured on Vickers 10 kg scale. See Figures 8 through 11 and Table VII for the correlation process.

Our correlation based on both % martensite and HAZ hardness as parameters shows a standard deviation of 8.3 N/mm^2. Christensen's[23] correlation based on % martensite alone has a standard deviation of 17.8 N/mm^2.

Further, including Christensen's implant test data at various hydrogen levels (Table VIII), we find that σ_{CR} correlates very well with the HYDROGEN INDEX and HAZ INDEX in the form:

$$\sigma_{CR} = (\text{HAZ INDEX})^{1/2} \times (\text{HYDROGEN INDEX})$$

$$= (1565 - 10 \times \%M - \bar{H})^{1/2} \times (31 - 15.5 \log [H]) \quad (19)$$

where $\bar{H}$ is the maximum HAZ hardness. Figures 12 and 13 show the correlation diagrams.

3.4 Role of Hydrogen in Affecting σ_{CR}

In regard to the role of hydrogen in affecting the cracking susceptibility, several interactions have been put forth in literature:

1) Hydrogen absorbed on the iron surfaces decreases the cohesion across the cubic cleavage planes as postulated by Pfeil[25], or absorbed hydrogen lowers the surface energies of cubic cleavage planes as postulated by Petch and Stables[26], and Uhling.[27]

2) Accumulated molecular hydrogen produces "pressure" effects as described by Zapffe and Sims[28], Simalowski[29], Tetel-

TABLE VII

Comparison Between Our's and Christensen's Correlation

No.	Heat Input kJ/mm	C	Mn	Si	Reported σ_{CR} N/mm^2	Our Correlated σ_{CR} N/mm^2	Christensen's Correlated σ_{CR} N/mm^2
1	0.9	0.109	1.61	0.43	420	429	440
2	1.3	0.109	1.61	0.43	480	481	500
3	1.7	0.109	1.61	0.43	550	543	562
4	0.9	0.140	1.57	0.43	325	329	332
5	1.3	0.140	1.57	0.43	375	374	389
6	1.7	0.140	1.57	0.43	440	410	426
7	0.9	0.170	1.59	0.43	250	258	262
8	1.3	0.170	1.59	0.43	300	306	317
9	1.7	0.170	1.59	0.43	350	362	377
10	0.9	0.215	1.59	0.43	215	205	223
11	1.3	0.215	1.59	0.43	240	238	262
12	1.7	0.215	1.59	0.43	275	261	292

* Hydrogen Level 7 ppm

Christensen's Correlation $\sigma_{CR} = 130 + 540(1 - m)^{1/2}$ N/mm^2

Our Correlation $\sigma_{CR} = 18 \times (1565 - 10 \times M - \bar{H})^{1/2}$ N/mm^2

Standard Deviation for our Correlation 8.3 N/mm^2

Standard Deviation for Christensen's Correlation 17.8 N/mm^2

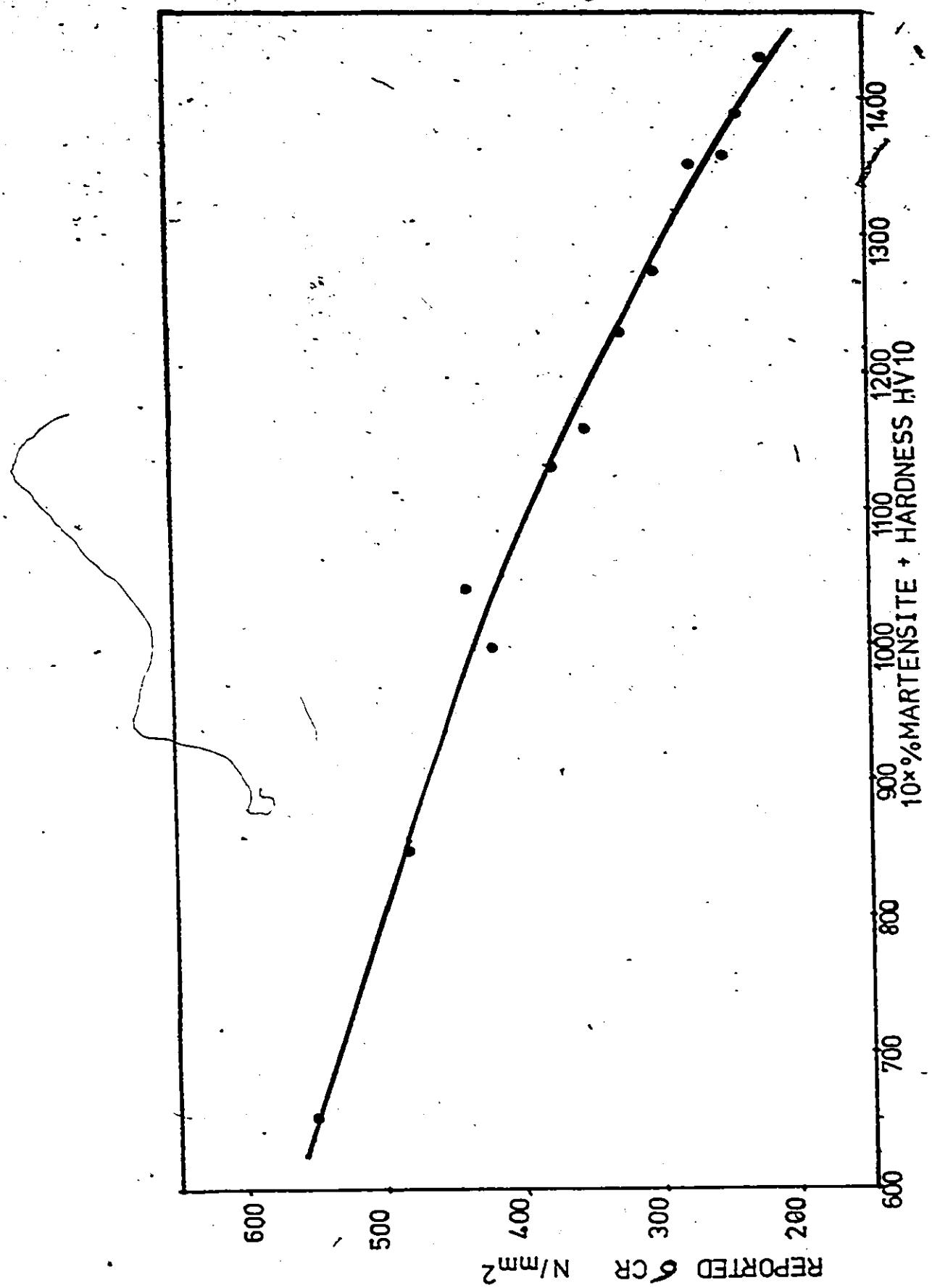

Figure 8 Correlation Between σ_{CR} and Both % Martensite and Hardness as Parameters

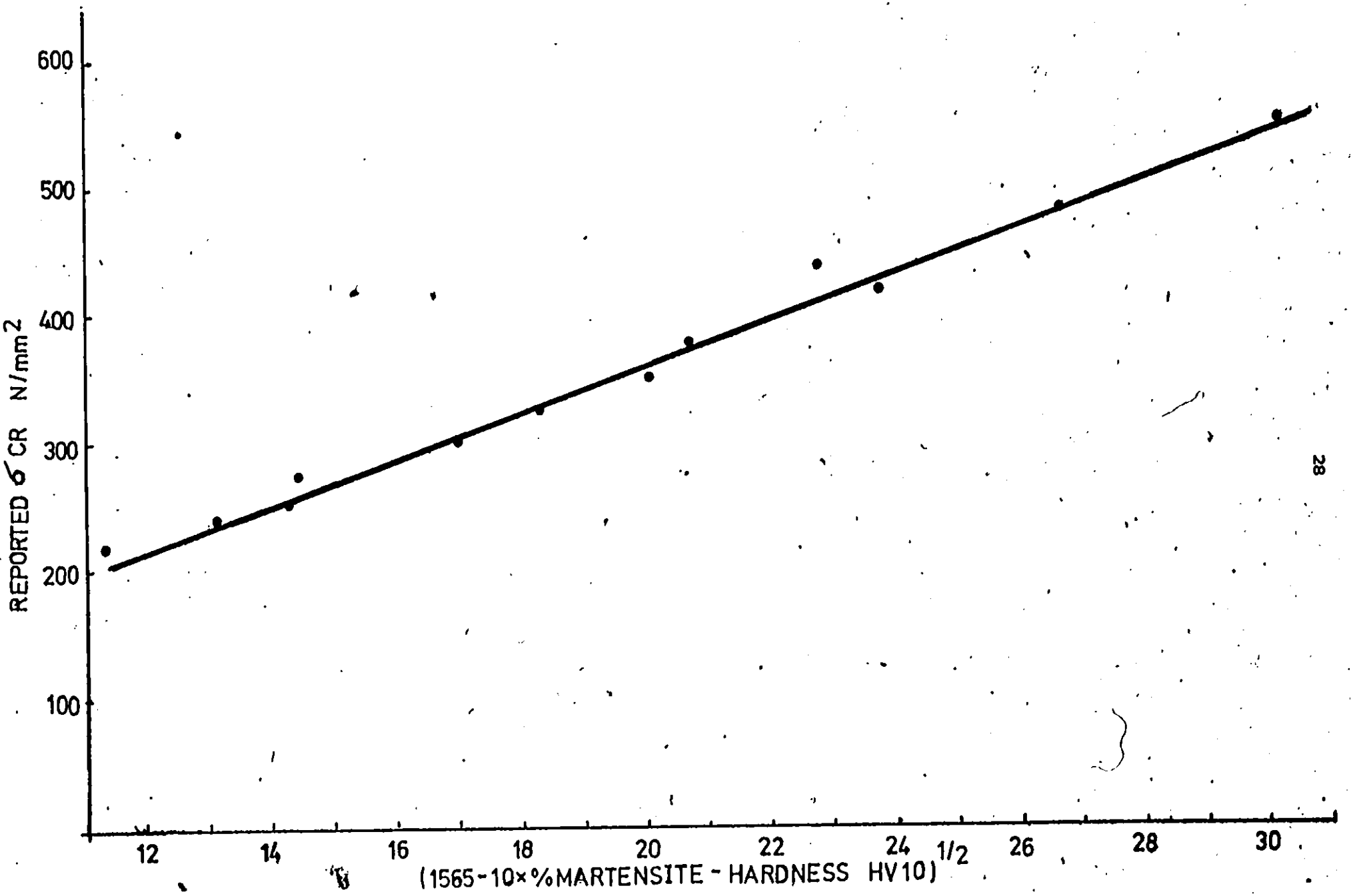

Figure 9 Correlation Between σ_{CR} and HAZ INDEX

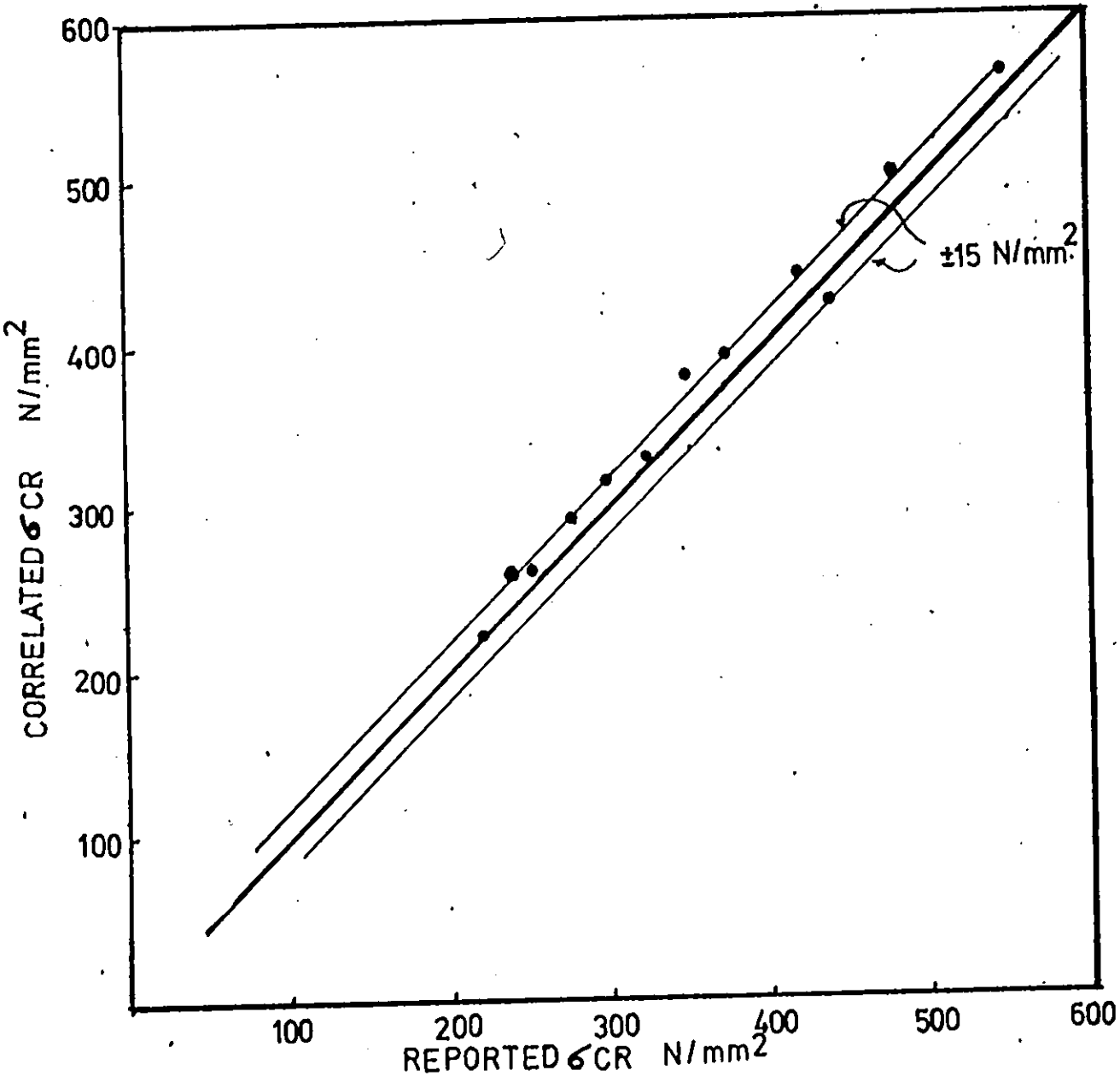

Figure 10 Comparison Between Correlated and Observed σ_{CR} With % Martensite as Parameter

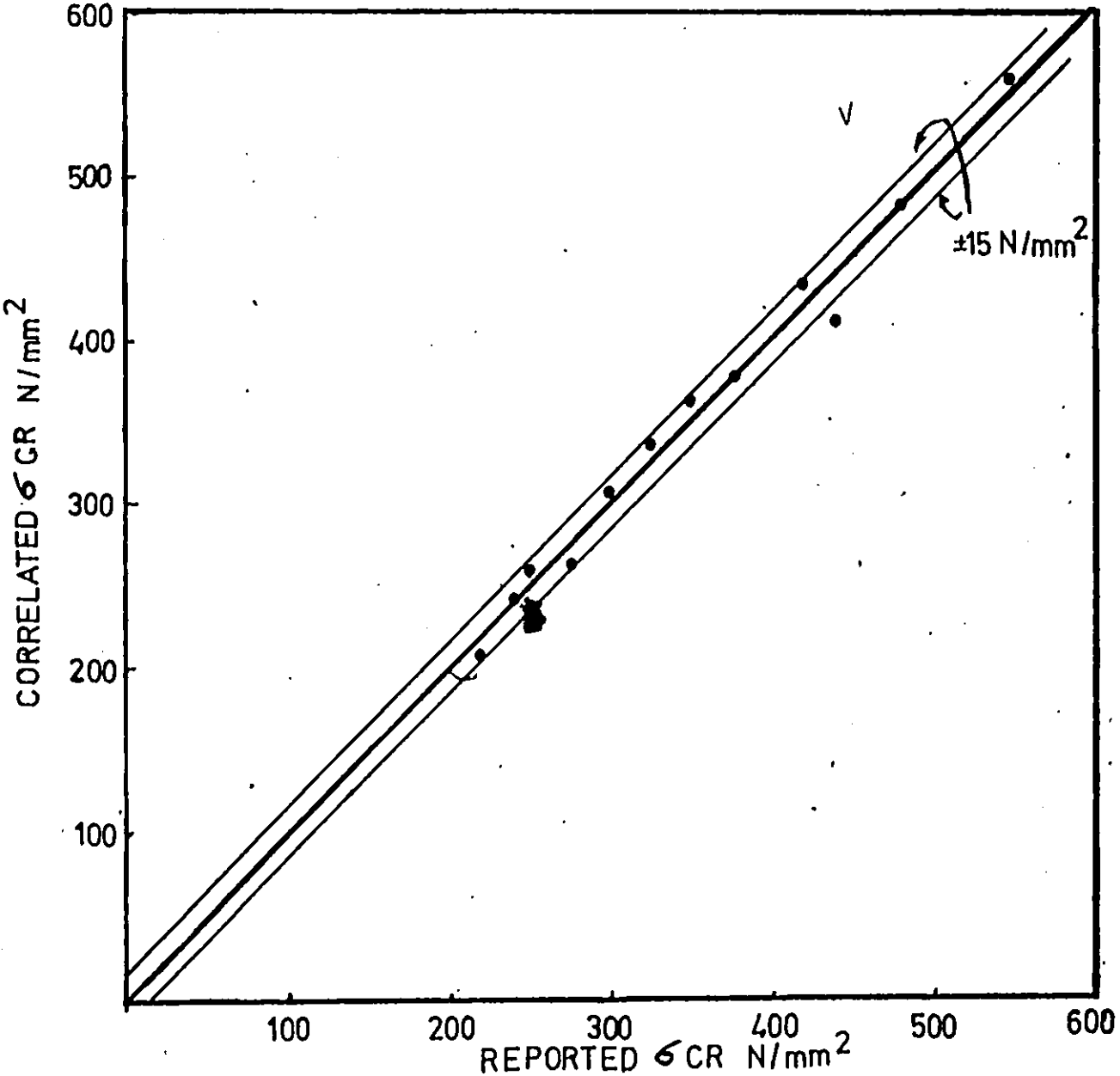

Figure 11 Comparison Between Correlated and Observed σ_{CR} With % Martensite and Hardness as Parameters

TABLE VIII

Influence of Hydrogen Level on σ_{CR}

No.	Heat Input kJ/mm	C	Mn	Si	Hydrogen ppm	σ_{CR} N/mm^2
1	1.3	0.140	1.57	0.43	3	500
2	1.3	0.140	1.57	0.43	7	375
3	1.3	0.140	1.57	0.43	30	175
4	1.3	0.170	1.59	0.43	3	400
5	1.3	0.170	1.59	0.43	7	300
6	1.3	0.170	1.59	0.43	30	130
7	1.3	0.215	1.59	0.43	3	320
8	1.3	0.215	1.59	0.43	7	240
9	1.3	0.215	1.59	0.43	30	100

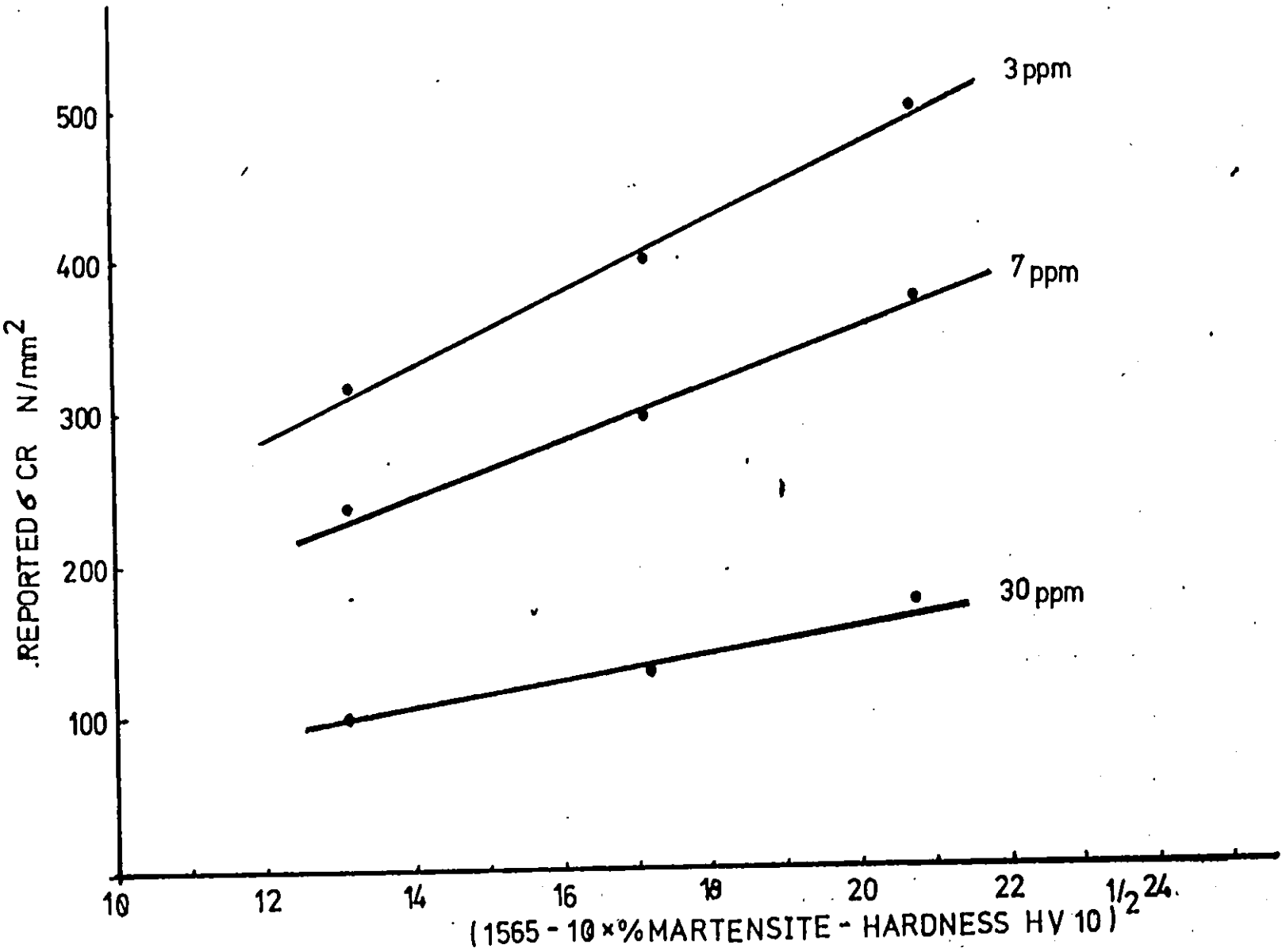

Figure 12 Influence of Hydrogen Level on σ_{CR}

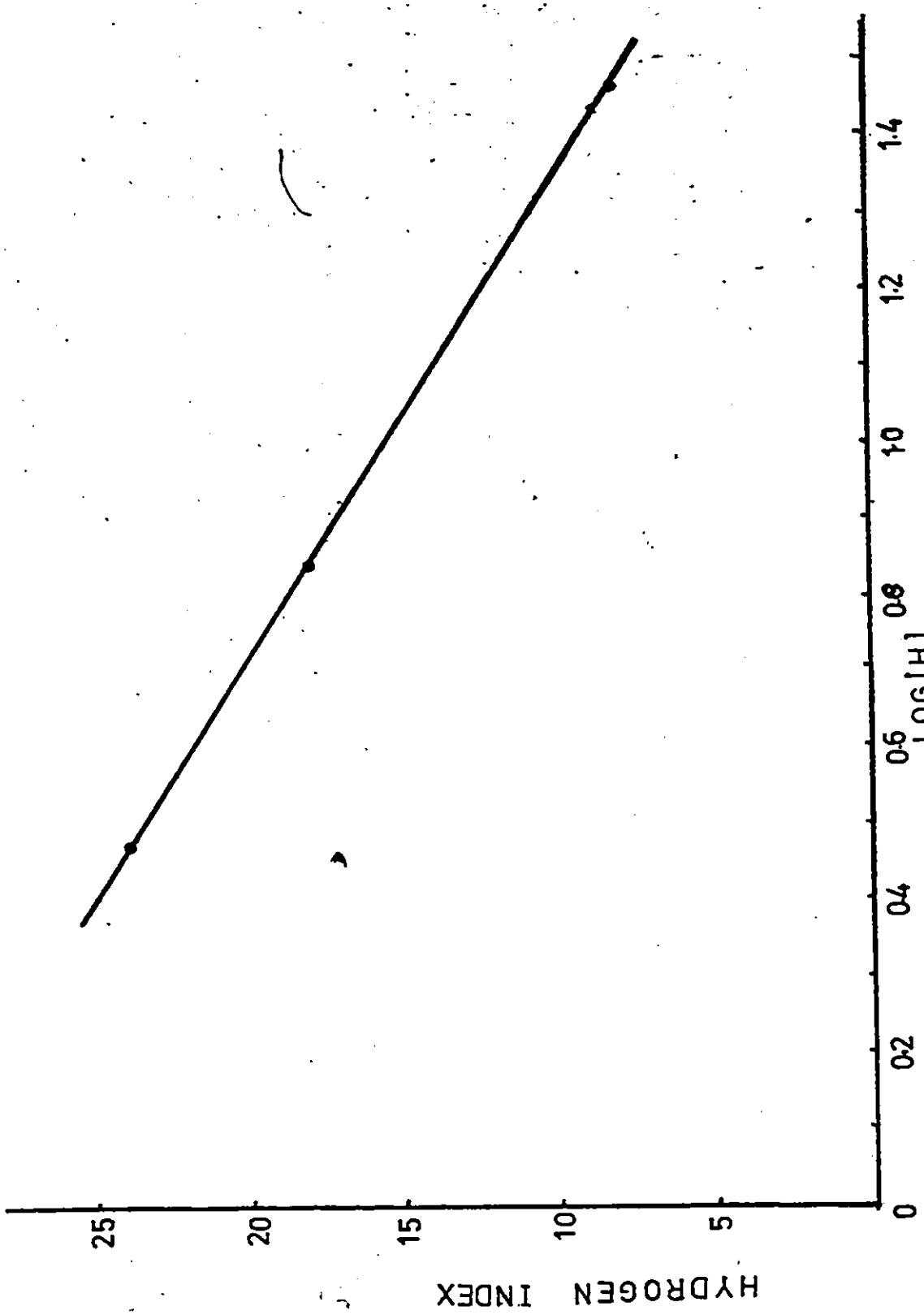

Figure 13 Variation of Hydrogen Index With Hydrogen Level

man[30] and Robertson and Tetelman.[31]

3) Embrittlement produced by the presence of brittle hybrides as postulated by Welchselfelder[32], or hydrogen rich phases as suggested by Westlake.[33]

Beachem[27], in his new model for hydrogen-assisted cracking, puts forth the easing of dislocation motion or generation or both, as the basic hydrogen-steel interaction, suggesting that hydrogen aids whatever deformation processes the microstructure will allow.

Beachem's[34] model puts forth two important aspects regarding the role of hydrogen in influencing cracking susceptibility:

1) For a given microstructural characteristic, cracking will occur at critical combinations of stress intensity and hydrogen concentration.

2) Since hydrogen merely assists cracking by aiding dislocation motion or generation or both, it only "adds" to the effect of externally applied stress and its internal stress intensification. Hence, at higher hydrogen concentrations, the stress intensity required for cracking will be lower, as represented in Figure 14.

The second aspect of the Beachem[34] model for hydrogen-assisted cracking is very important since it is opposed to the theory which says that for a given microstructure, the hydrogen concentration required for cracking is independent of the stress intensity level. In other words, a definite critical hydrogen concentration, characteristic of the microstructure, has to be reached before cracking, regardless of the stress intensity level.

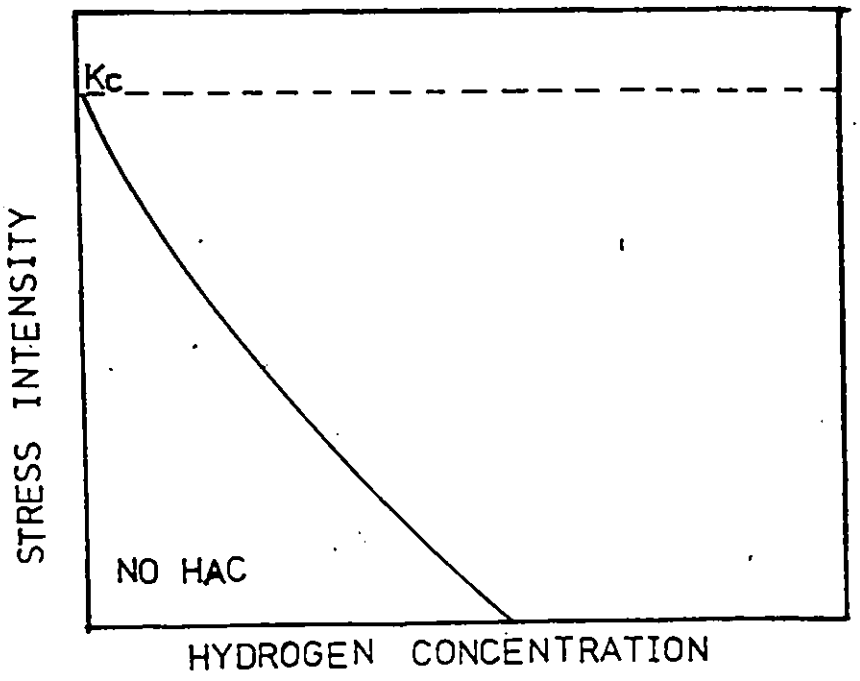

Figure 14 Stress Intensity and Hydrogen Concentration Combinations For Fracture as Suggested by Beachem (34)

Troiano[35] has demonstrated that hydrogen cracking occurs in the region of high triaxial tensile stresses in front of the notch on the specimen. Hydrogen migrates to that region by stress-induced diffusion (see Figure 15). Thus, analysis of the implant test data in terms of the stress intensity in front of the notch on the specimen, and the stress induced diffusion of hydrogen to that region, can give us information on the role of hydrogen in HAZ cracking.

3.4.1 Calculation of Hydrogen Concentration and Stress Intensity in the Region of Maximum Triaxiality

Urednicek[36] has analysed the stress induced diffusion of hydrogen to the maximum triaxial stress region in front of the notch on the implant specimen. His analysis gives the equilibrium concentration of hydrogen attained in the region of maximum triaxiality as follows:

$$\ln\left(\frac{H_{CR}}{H_I}\right) = \frac{V_H \alpha''(\sigma y)_I}{RT} \left\{\ln\left[(k_{TH})_I \frac{\alpha'}{\rho_o E} + 1\right] + \frac{1}{2}\right\} \qquad (20)$$

for a mode I crack under elastic-plastic plane strain condition where

H_{CR} is the equilibrium hydrogen concentration reached in the maximum triaxiality region,

H_I is the concentration governed initial hydrogen content in that region,

V_H is the partial molar volume of hydrogen,

α'' constant = 2,

$(\sigma y)_I$ is the yield stress of the microstructure in the critical region of the HAZ,

R is the universal gas constant,

T is temperature in kelvin,

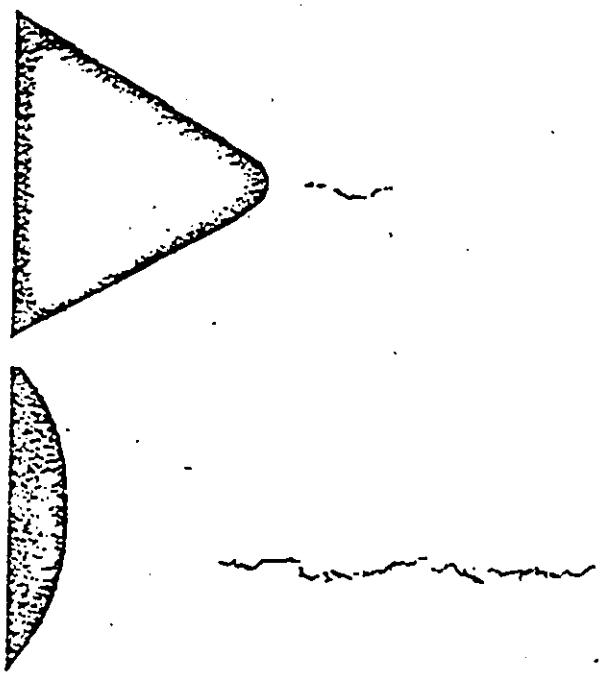

Figure 15 Influence of Notch Radius on the Location of Hydrogen Assisted Cracking [35]

$(k_{TH})_I$ is the implant test threshold intensity,

α' constant = 3,

E = Young's Modulus of Elasticity,

ρ_o constant = 2.2×10^{-4} $m^{\frac{1}{2}}$ = 13.91×10^{-4} $\sqrt{INCH}$

Assuming, after Urednicek[36], that the concentration governed hydrogen content in the critical region of the HAZ to be 0.4 H, where H is the initial hydrogen content of the weld, and carrying out appropriate substitutions in the formula (for details see Appendix 1), we have:

$$\ln \left(\frac{H_{CR}}{0.4H}\right) = 1.6393 \times 10^{-3}(\sigma y) \left\{\ln \left[3.23 \times 10^{-3}(\sigma_{CR}) + 1\right] + \frac{1}{2}\right\} \quad (21)$$

where stress is expressed in N/mm^2.

For Christensen[23] data, we calculated the H_{CR} values at different hydrogen levels for the same microstructure from Equation 21 with the HAZ yield stress estimated from HAZ Hardness. Table IX shows the calculated H_{CR} values for hydrogen levels of 1, 3 and 7 ppm. Figure 16 shows the combinations of H_{CR} and stress intensity levels for different HAZ microstructures and hydrogen levels.

3.4.2 Discussion

From Figure 16, we can see that for a given microstructure, the H_{CR} required in the critical region for cracking is not independent of the stress intensity. This is in agreement with Beachem's[34] model for hydrogen assisted cracking. Thus, the role of hydrogen in influencing the cracking susceptibility seems to be that of just aiding or assisting the applied stress so that cracking can occur.

This suggests that Urednicek's[36] procedure of extending the results of the implant tests to actual welds by treating the hydrogen

TABLE IX

Calculated Stress Intensity and H_{CR} Levels at σ_{CR}

No.	%M	Hardness	Hydrogen Bulk ppm	σ_{CR} N/mm^2	K_{TH} $KSI\sqrt{INCH}$	H_{CR} ppm
1	77	363	1	660	28.6	10
2	77	363	3	500	21.7	21
3	77	363	7	375	16.7	36
4	88	395	1	520	22.6	9.5
5	88	395	3	400	17.4	20
6	88	395	7	300	13.8	37
7	94	450	1	430	18.7	13
8	94	450	3	320	13.9	26
9	94	450	7	240	10.5	44

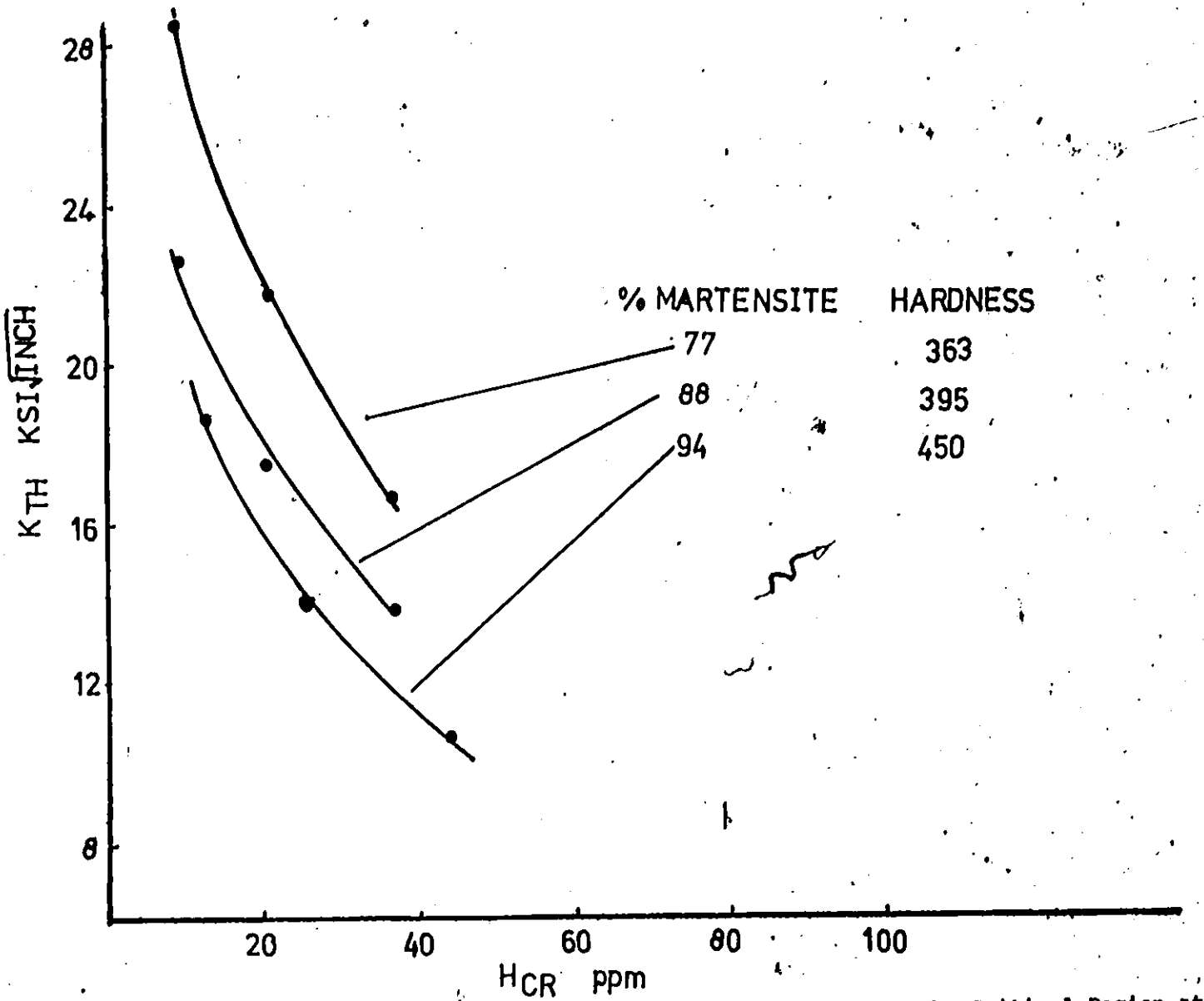

Figure 16 Combination of Stress Intensity and Hydrogen Concentration in the Critical Region at σ_{CR}

concentration (H_{CR}) needed at the critical region as remaining independent of the stress intensity for a given microstructure to crack, is in serious error. For the same microstructure, HAZ cracks at different hydrogen concentrations in the critical regions, depending upon the stress intensity. The higher the stress intensity in the critical region of the HAZ, the lower the hydrogen concentration needed in that region for cracking to occur.

CHAPTER 4

PREDICTION OF σ_{CR} ON THE BASIS OF HEAT-INPUT, PLATE THICKNESS, PLATE COMPOSITION AND HYDROGEN LEVEL

4.1 General Remarks

In the last chapter, we presented a correlation between σ_{CR}, maximum hardness, % martensite and hydrogen level by:

$$\sigma_{CR} = (31 - 15.5 \times \log [H])(1565 - 10 \times \%M - \overline{H})^{1/2} \quad (19)$$

Prediction of σ_{CR} on the basis of heat input, plate thickness, plate composition and hydrogen level can greatly aid in evaluating various welding procedures for different steels at low cost and in minimal time.

The system of prediction is shown in the block diagram in Fig.17.

(a) Based on the heat input and plate thickness, we first predict the cooling rate by heat transfer calculations.

(b) With cooling rate and plate composition as inputs, we predict the HAZ, % martensite and hardness.

(c) Finally, we obtain σ_{CR} through the correlation formula for the expected hydrogen level in the weld.

4.2 Prediction of Heat Affected Zone Cooling Rate

4.2.1 Heat Transfer With 3D Heat Flow

Heat flow by conduction can be characterized by 3D, 2D or 2.5D, as shown in Figure 18. For our analysis, we neglect the surface losses through convection and radiation.

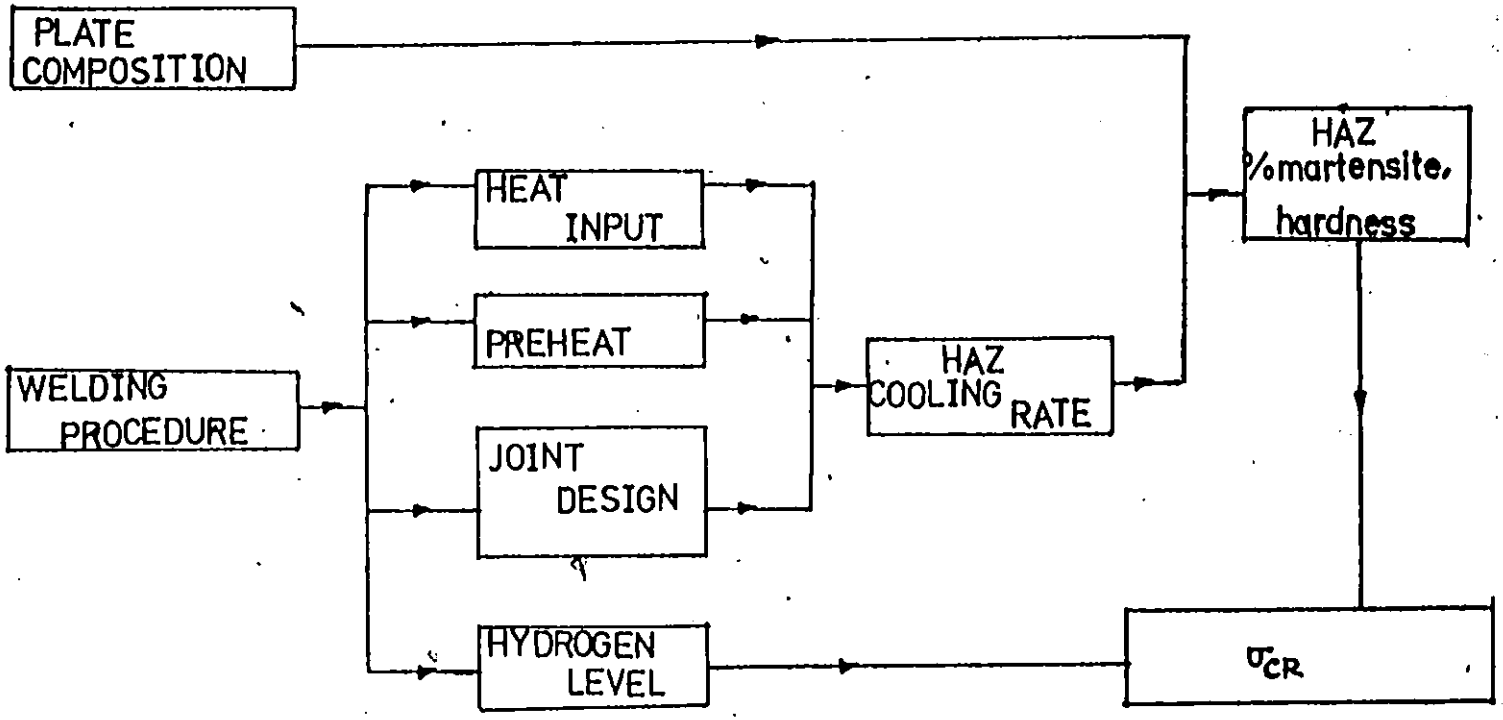

Figure 17 Block Diagram for Predicting σ_{CR} on the Basis of Welding Heat Input, Plate Composition, and Hydrogen Level.

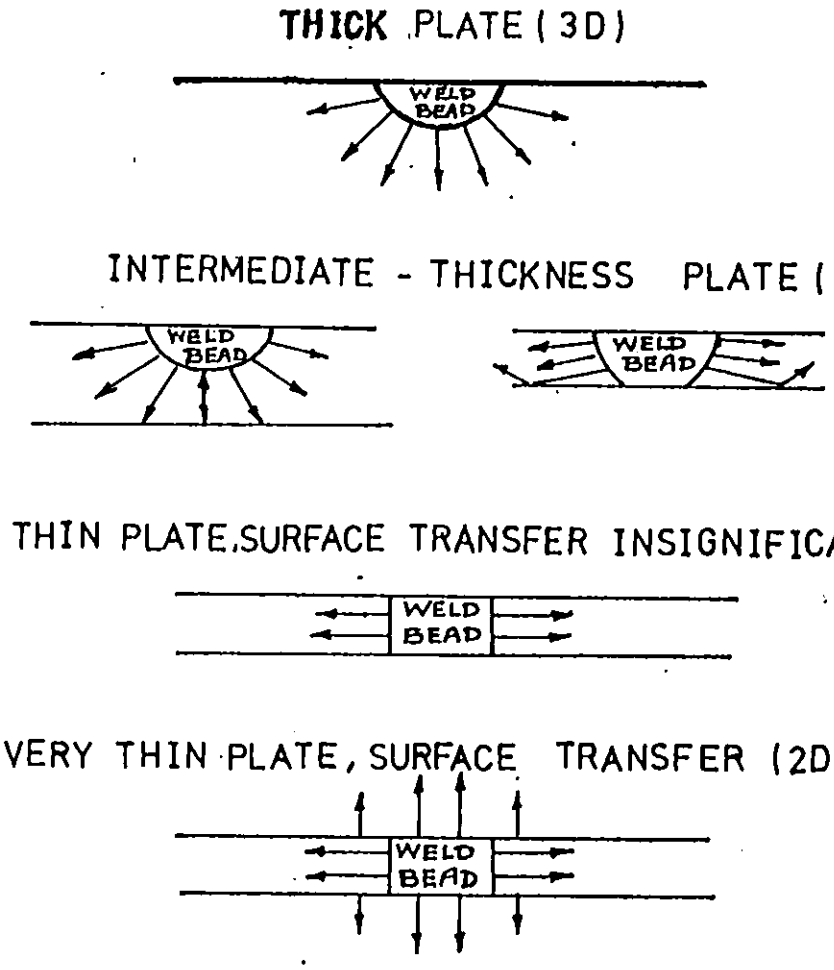

Figure 18 Heat Flow Conditions In Welding

Rosenthal's[37] analysis of the 3D and 2D heat flow during welding has been used by many researchers for characterizing the thermal cycle of the welding operation.

For plate thicknesses over 1 inch, it is observed that 3D mode of heat flow prevails. Rosenthal's equation for the 3D mode temperature distribution is given by:

$$T - T_o = \frac{q}{4\pi k} e^{-\lambda v \xi} \frac{e^{-\lambda v R}}{R} \qquad (22)$$

where T - temperature

T_o - initial temperature of the plate

q - heating rate

λ - $\frac{\text{specific heat x density}}{\text{thermal conductivity}}$

ξ - distance along weld line, relative to the point source

$\xi = x - vt$

v - speed of the source

R - $\sqrt{\xi^2 + y^2 + z^2}$ position of the point of interest relative to the source

t - time

If we consider the center line of the weld, we have $y = z = 0$,

therefore $|R| = |\xi|$

and when the source passes the point of interest;

$$\xi = -vt$$

where t is the time, since the source passed the point of interest. Thus, for a point on the weld center line, the temperature is given by:

$$T - T_o = \frac{q}{4\pi k} \times \frac{1}{|\xi|}$$

or

$$T - T_o = \frac{q}{4\pi k} \times \frac{1}{vt} \tag{23}$$

Equation (23) assumes a plate bounded by planes $z \pm \infty$. However, for welding conditions, we have the plate bounded by $z = 0$ and $z = g$, where g is the plate thickness. Equation (23) then becomes:

$$T - T_o = \frac{q}{2\pi k} \times \frac{1}{vt} \tag{24}$$

In Equation (24), q is the rate of heat actually supplied to the plate. In terms of the heat input (q') given by welding arc voltage and current, we can write:

$$q = (I.F.)q'$$

where (I.F.) is the efficiency factor.

Equation (24) then becomes:

$$T - T_o = (\frac{1}{2\pi k}) \times (I.F.) \times (\frac{q'}{v}) \times \frac{1}{t} \tag{25}$$

The factor $(\frac{q'}{v})$ can be taken as characteristic of the heat input. Calling $(\frac{q'}{v}) = E$ = heat input per unit weld length, we have:

$$T - T_o = (\frac{1}{2\pi k}) \times (I.F.) \times E \times \frac{1}{t} \tag{26}$$

4.2.1.1 Application of 3D Heat Flow Relations

Equation (26) does not take into account the variation of thermal conductivity with temperature. Also, the effects of release of heat of fusion, phase transformations, surface and radiation losses are ignored. Hence, Equation (26) is not precise in predicting actual temperature profile.

However, Dorshu,[38] Signes,[39] and Graville[40] measured actual cooling rates in welding and found that the form of the Rosenthal Equa-

tion (26) can be retained by introducing proper values of the constant involving thermal conductivity. Rearranging Equation (26), we have:

$$(T - T_o) \times t = \left(\frac{1}{2\pi k}\right) \times (I.F.) \times E \qquad (27)$$

Differentiating Equation (27) with respect to 't' and substituting for 't' from Equation (26), we have:

$$\frac{dT}{dt} = -\frac{2\pi k}{(I.F.)} \times \frac{1}{E} \times (T - T_o)^2 \qquad (28)$$

Introducing a constant $B_{3D} = 2\pi k_{effective}$ and $A_{3D} = \frac{2\pi k_{effective}}{(I.F.) \times E}$, Equation (28) can be written as:

$$\frac{dT}{dt} = \frac{B_{3D}}{(I.F.) \times E} \times (T - T_o)^2 \qquad (29)$$

$$\frac{dT}{dt} = A_{3D} \times (T - T_o)^2 \qquad (30)$$

Graville[40] observed that for cooling rate measurements at a given temperature for various heat inputs E, A_{3D} in Equation (30) varies inversely as E (see Figure 19). This shows that Rosenthal's[37] equations can be used with appropriate constants to predict actual cooling rates. Graville[40] also obtained the variation of B_{3D} in Equation (29) with the temperature at which the cooling rate was measured. Thus, in Figure 20, we see that the value of B_{3D} varies linearly from 5.5×10^{-3} $^oC^{-1}sec^{-1}kJ\ in^{-1}$ at 300°C to 3.6×10^{-3} $^oC^{-1}sec^{-1}kJ\ in^{-1}$ at 600°C.

Signes[39] has also carried out similar experiments and has reported the value of B_{3D} at 700°C to be $3.02 \times 10^{-3} {}^oF^{-1}sec^{-1}kJ\ in^{-1}$ or $5.44 \times 10^{-3} \times {}^oC^{-1}sec^{-1}kJ\ in^{-1}$. Dorshu[38] reported the constant B_{3D} at 700°C to be 3.03×10^{-3} $^oF^{-1}sec^{-1}kJ\ in^{-1}$ or $5.45 \times {}^oC^{-1}sec^{-1}kJ\ in^{-1}$.

Both Dorshu[38] and Signes[39] used Gas Metal Arc Welding (GMAW)

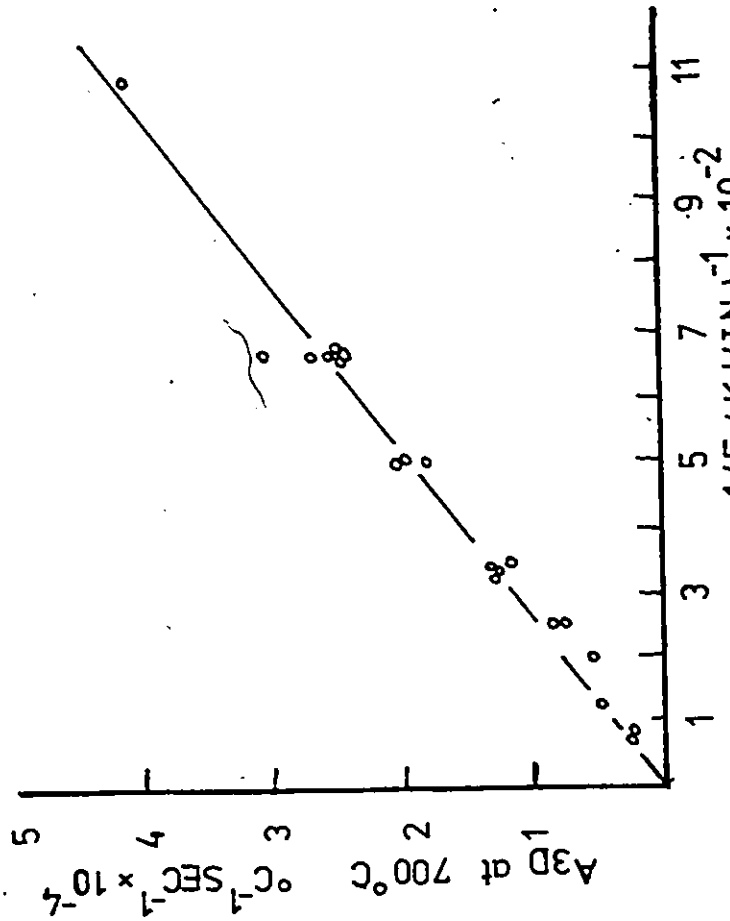

Figure 19 Variation of A_{3D} with Heat Input[40]

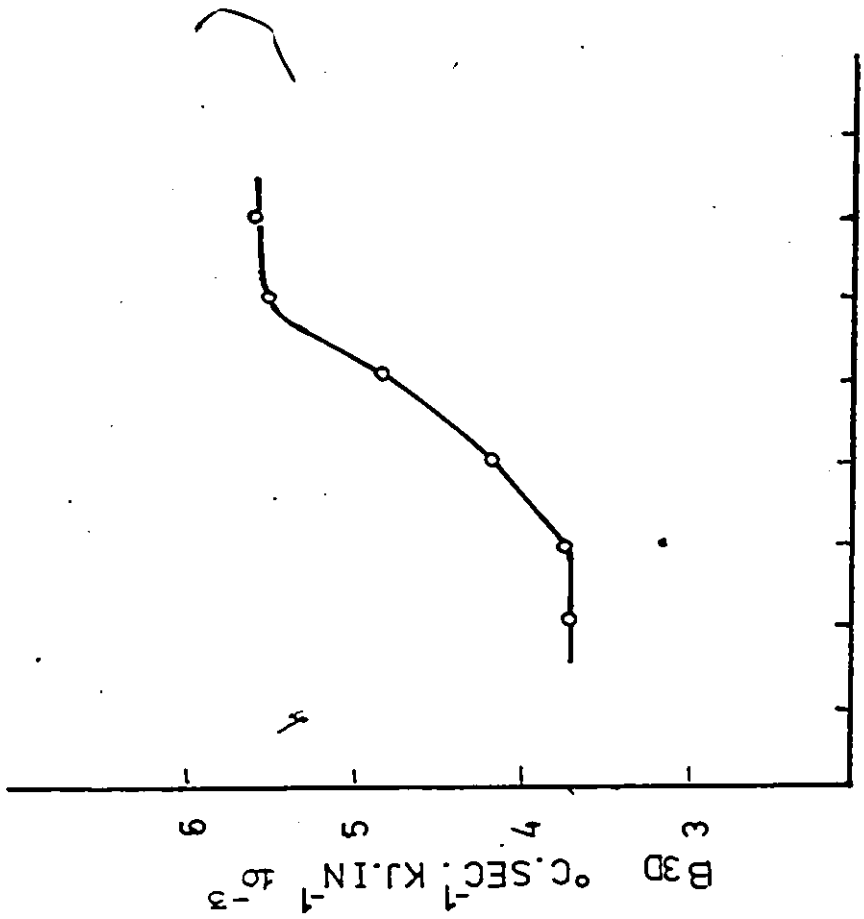

Figure 20 Variation of B_{3D} with Temperature[40]

while Graville used Submerged Metal Arc (SAW). Thus, the difference in arc efficiency can explain the difference in the values of the constant B_{3D}.

4.2.1.2 Prediction of Cooling Time Between 800°C and 500°C

The cooling time between 800°C and 500°C has been used by many researchers to correlate the HAZ hardness and microstructure with the cooling rate. Rosenthal's[37] equations and the values of constants (B_{3D}) determined from actual welding thermal cycles can allow us to predict the cooling time between 800°C and 500°C for a given heat-input and plate thickness.

For the time Δt between 800°C and 500°C, we can write, from Equation (26):

$$\underset{800\text{-}500°C}{\Delta t} = \left(\frac{1}{2\pi k}\right) \times (I.F.) \times E \times \left[\frac{1}{(500-T_o)} - \frac{1}{(800-T_o)}\right] \qquad (31)$$

Introducing $B_{3D} = 2\pi k_{effective}$, we have:

$$\underset{800\text{-}500°C}{\Delta t} = \left(\frac{1}{B_{3D}}\right) \times (I.F.) \times E \times \left[\frac{1}{(500-T_o)} - \frac{1}{(800-T_o)}\right] \qquad (32)$$

Inserting the average value of the variation in B_{3D} reported by Graville, Equation (32) becomes:

$$\underset{\substack{800\text{-}500°C \\ \text{seconds}}}{\Delta t} = 5.74 \times 10^3 \times (I.F.) \times E \times \left[\frac{1}{(500-T_o)} - \frac{1}{(800-T_o)}\right] \qquad (33)$$

where E is in kJ/mm; q, T_o is in °C.

4.2.2 Heat Transfer With 2D Heat Flow

In the previous sections, we have restricted outselves only to 3D heat flow. However, for plate thicknesses lower than 1 inch, 2.5D or

2D heat transfer prevails. Thus, to be able to predict cooling time between 800 and 500°C for plate thicknesses less than 1 inch, we have to look into the analysis of the 2.5D and 2D mode of heat flow. For the 2D mode of heat flow, the equations are well defined. Corresponding to 3D equations (26), (28), and (32), we have 2D heat flow equations as follows:

$$T - T_o = \frac{1}{2\sqrt{kc\rho\pi}} \times \frac{(I.F.)xE}{g} \times \frac{1}{\sqrt{t}} \tag{34}$$

$$\frac{dT}{dt} = B_{2D} \times \frac{g^2}{E^2x(I.F.)^2} \times (T - T_o)^3 \tag{35}$$

where $B_{2D} = 2\pi kc\rho$

and

$$\Delta t_{800-500°C} = \frac{1}{2B_{2D}} \times (I.F.)^2 \times \frac{E^2}{g^2} \times \left[\frac{1}{(500-T_o)^2} - \frac{1}{(800-T_o)^2} \right] \tag{36}$$

4.2.3 Heat Transfer WIth 2.5D Heat Flow

2D and 3D heat flow modes represent two extreme conditions of conduction of heat through "thin" and "thick" plates. For both 2D and 3D modes, we can see from Equations (26) and (34) a unique dependence upon arc energy input represented by E, which has dimensions of energy per unit length. It is not the speed with which energy is introduced, but rather the amount of energy per unit length of the weld which determines the cooling rate.

The problem can thus be reduced to determination of the temperature distributions and cooling rates which follow instantaneous release of a specified quantity of heat along a straight line which lies on one surface of a flat plate. Jhaveri, Moffatt, Adams et al[41] have given the general representation of the results of such an analysis by the use

of dimensionless parameters as follows:

Temperature:

$$Y = \frac{2\pi\rho C v g^2 (T-T_o)}{q} \tag{37}$$

Time:

$$X = \frac{\alpha t}{g^2} \qquad \alpha = \text{thermal diffusivity} \tag{38}$$

In terms of these parameters, Adams et al represent the temperature at the location of the line source by the equation

$$y = \frac{2}{x}\left[\frac{1}{2} + \sum_{1}^{\infty} e^{-n^2/x}\right] \tag{39}$$

and the cooling rate by the equation

$$\frac{dy}{dx} = -\frac{2}{x^2}\left[\frac{1}{2} - \sum_{1}^{\infty} \left(\frac{n^2}{x} - 1\right) e^{-n^2/x}\right] \tag{40}$$

For "thick" plates (3D mode), the series terms in Equations (39) and (40) disappear, and the time, X, can be eliminated algebraically to give:

$$\frac{dy}{dx} = -y^2 \tag{41}$$

Equation (41) is identical to Equation (28).

Similarly, for "thin" plates (2D mode), it can be shown that Equations (39) and (40) reduce to:

$$\frac{dy}{dx} = \frac{-y^3}{2\pi} \tag{42}$$

Equation (42) is identical to Equation (35).

4.2.4 Graphical Representation of Heat Flow Conditions as Functions of Plate Thickness

Thus, in order to get into the region of 2.5D mode of heat flow, or, in other words, to relate absolute cooling rate to plate thickness

between the 2D and 3D regions of heat flow, Adams et al introduced a graphical relation, as shown in Figure 21. In terms of the dimensionless parameters defined above, Figure 21 is a plot of

$$(1/y^2)(dy/dx) \quad \text{vs} \quad Y/2\pi.$$

In the coordinates of Figure 21, Equation (28) is represented by the horizontal at 1.0 (i.e., top edge of the graph) and Equation (35) by the straight line of 45° slope. The curve corresponds to the cooling rates on the top surface of the plate and have been calculated using Equations (39) and (40).

Clearly, for the values less than 0.35 on the horizontal scale, Equation (35) quite accurately predicts cooling rates throughout the thickness of the plate. In this region, heat flow is almost purely 2D.

For the values on the horizontal scale greater than 1.2, heat flow is 3D and Equation (28) is accurate. In between in the 2.5D region where neither 3D nor 2D equations apply with great accuracy and hence, in this region, the graph in Figure 21 is useful in calculating cooling rates.

4.2.5 Procedure for Predicting Cooling Rate

The procedure to predict the cooling rate for a plate of any thickness can then be put down as follows:

1) first calculate 3D cooling rate for the given heat input. For example, 3D cooling rate at about 700°C can be obtained from $\Delta t_{800-500°C}$ by Equation (32).

$$R_{3D} = 300/(5.74 \times 10^3) \times (\text{I.F.}) \times E \times \left[\frac{1}{(500-T_o)} - \frac{1}{(800-T_o)}\right] \quad (43)$$

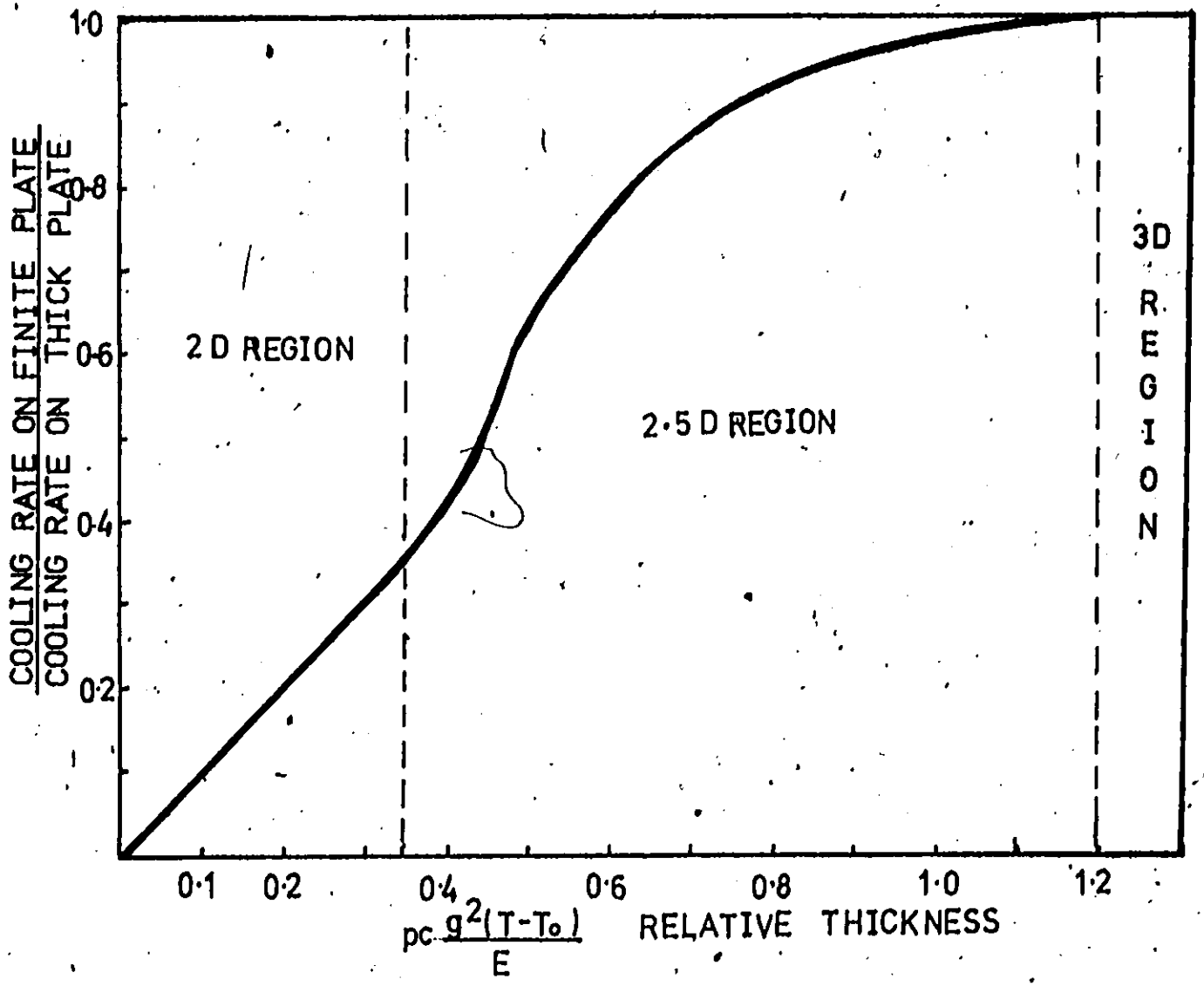

Figure 21 Variation of Cooling Rate With Plate Thickness

2) using Figure 21, calculate the actual cooling rate for the plate thickness of interest.

For example, after calculating R_{3D}, we enter Figure 21 with abscissa

$$x = \rho c g^2 (700-T_o) \left(\frac{v}{q}\right) x \left(\frac{1}{I.F.}\right) \quad (44)$$

and find the corresponding ordinate 'O'

If $x > 1.2$ R actual = R_{3D}

If $x < 0.35$ R actual = $R_{3D} * x$

If $0.35 < x < 1.2$ R actual = $R_{3D} * O$

4.2.6 Discussion

Christensen[22] has reported the cooling time between 800 and 500°C for different heat inputs, with single beads deposited on 30 mm thick plate. Table X shows the comparison between the predicted and observed cooling times between 800 and 500°C for an arc efficiency of 0.85.

It is important to note that Equation (32) has been derived for cooling conditions which prevail on the center line of the weld. The distribution of the cooling rates around the weld center line can also be calculated, but computation is somewhat involved. However, the cooling rate is maximum on the weld center line and the shape of the cooling rate distribution is such that the center line cooling rate is only 5 to 10% higher than that in the weld HAZ[41] and is therefore representative of the cooling rate in the HAZ region.

TABLE X

Comparison Between Reported & Calculated Cooling Times Between 800°C - 500°C

No.	Heat Input kJ/mm	Plate Thickness mm	Reported Cooling Time (sec.)	Calcualted Cooling Time (sec.)	Arc Efficiency
1	0.9	30	3.6	3.5	0.85
2	1.3	30	5.1	5.1	0.85
3	1.7	30	6.6	6.6	0.85

4.3 Prediction of Heat Affected Zone Microstructure

4.3.1 % Microconstituent - Composition - Cooling Rate Relations

On the basis of CCT diagrams, Dolliet-Maynier et al[42] have developed linear regression formulas to predict microstructure as a function of chemical composition, log cooling rate derived from cooling time between 800 and 500°C, and an austenization parameter.

The formulas are in the form of critical cooling rates necessary to yield 100, 90 and 50% martensite (M), given by V_1^{100}, V_1^{90}, and V_1^{50} respectively. Similarly, there are formulas for critical cooling rates necessary for 0, 10 and 50% ferrite-pearlite (F-P) given by V_2^{100}, V_2^{90}, and V_2^{50} respectively. For a given steel composition, V_1^{100}, V_1^{90}, V_1^{50} points separate martensite and bainite regions, and V_2^{100}, V_2^{90}, and V_2^{50} separate the bainite and ferrite-pearlite regions. Figure 22 illustrates this.

The formulas for the critical cooling rates are as follows:

$$\log(V_1^{100}) = 9.81 - (4.62 \times C + 1.10\ Mn + 0.54\ Ni + 0.50\ Cr + 0.66\ Mo + 0.0018\ Pa) \quad (45)$$

$$\log(V_1^{90}) = 8.76 - (4.04\ C + 0.96\ Mn + 0.49\ Ni + 0.58\ Cr + 0.97\ Mo + 0.0010\ Pa) \quad (46)$$

$$\log(V_1^{50}) = 8.50 - (4.13\ C + 0.86\ Mn + 0.57\ Ni + 0.41\ Cr + 0.94\ Mn + 0.0012\ Pa) \quad (47)$$

$$\log(V_2^{100}) = 10.17 - (3.80\ C + 1.07\ Mn + 0.7\ Ni + 0.57\ Cr + 1.58\ Mo + 0.0032\ Pa) \quad (48)$$

$$\log(V_2^{90}) = 10.55 - (3.65\ C + 1.08\ Mn + 0.77\ Ni + 0.67\ Cr + 1.49\ Mo + 0.0040\ Pa) \quad (49)$$

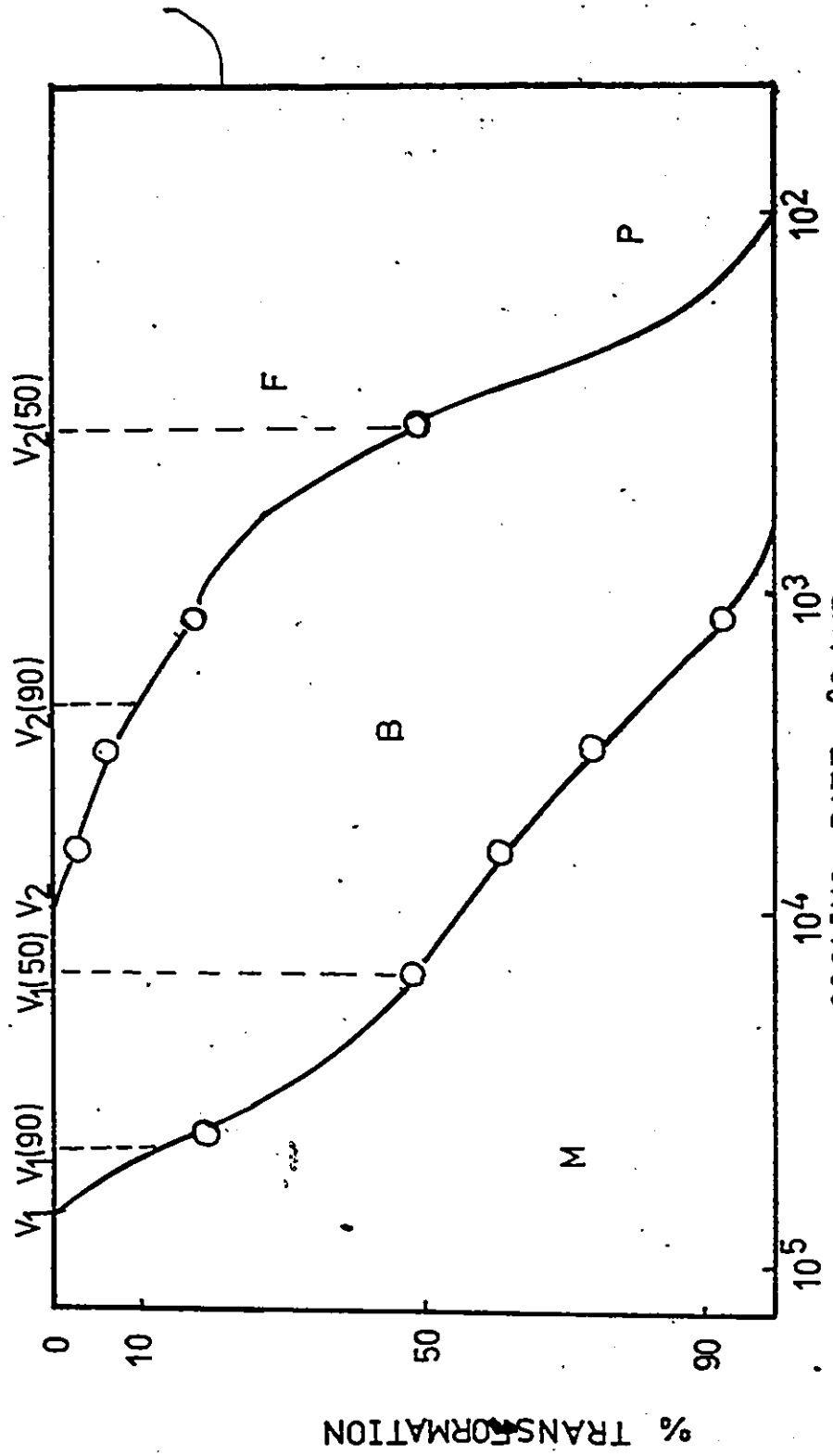

Figure 22 Transformation and Cooling Rate Chart[41]

$$\log(V_2) = 8.74 - (2.23C + 0.86\,Mn + 0.56\,Ni + 0.59\,Cr + 1.60\,Mo + 0.0032\,Pa) \quad (50)$$

where cooling rates are in °C/hr.

Pa is the austenization parameter for grain size, given by

$$Pa = \left(\frac{1}{T} - \frac{2.303 \times 1.987}{110 \times 10^3} \times \log\frac{t}{to}\right)^{-1} \quad (51)$$

T is the austenizing temperature in °k, t is the holding time at T, to is the unit of time used.

4.3.2 Hardness - Composition - Cooling Rate Relations

Dolliet and Maynier et al[42] have also developed linear regression formulas which give hardness of martensite (M), bainite (B) and ferrite-pearlite (F-P) as a function of chemical composition and cooling rate. The formulas are as follows:

Hardness of martensite (HM) Vickers 10 kg

$$= 127 + 949\,C + 27\,Si + 11\,Mn + 8\,Ni + 16\,Cr + 21\log(R) \quad (52)$$

Hardness of bainite (HB) Vickers 10 kg

$$= 185\,C - 323 + 330\,Si + 153\,Mn + 65\,Ni + 144\,Cr + 191\,Mo + \log(R)\,(98 + 53\,C - 55\,Si - 22\,Mn - 10\,Ni - 20\,Cr - 33\,Mo) \quad (53)$$

Hardness of ferrite-pearlite (HF-P) Vickers 10 kg

$$= 42 + 223\,C + 53\,Si + 30\,Mn + 12.6\,Ni + 7\,Cr + 19\,Mo + \log(R)\,(10 - 19\,Si + 4\,Ni + 8\,Cr + 130\,V) \quad (54)$$

where R is the cooling rate in °C/hr.

4.3.3 Prediction of HAZ % Martensite and Hardness

Using the Dolliet-Maynier formula for % martensite and hardness, together with the analysis of Section 4.2 for predicting cooling rates, we can predict HAZ microstructural characteristics by the following

procedure:

1) Using the analysis in Section 4.2 on prediction of HAZ cooling rate, we first obtain the actual cooling rate in the HAZ for given plate thickness, heat-input and preheat

2) For calculating the austenization parameter, the welding cycle is assumed to be equivalent to be 1400° - 1 sec. austenizing condition. Substituting this in Equation (51) we get:

$$Pa = \left(\frac{1}{1400 + 273} - \frac{2.303 \times 1.987}{110 \times 103} \log \frac{1}{3600}\right)^{-1} \quad (55)$$

$$= 1067° - 1 \text{ hr.}$$

3) For the given steel composition, Dolliet-Maynier formulas are then used to obtain critical cooling rates in terms of v_1^{100}, v_1^{90}, v_1^{50}, v_2^{100}, v_2^{90}, and v_2^{50}.

4) On the basis of critical cooling rates found in Step (3), the curve between these points is obtained. The curve between 100 and 90% martensite is obtained on the basis of v_1^{100} and v_1^{90}. Similarly, the curve between 90 and 50% martensite is obtained on the basis of v_1^{90} and v_1^{50} (see Figures 23 to 25).

5) With the shape of the % product vs log cooling rate established for the steel composition of interest, we use the cooling rate from Step (1) to obtain % martensite, bainite and ferrite-pearlite in HAZ.

6) Using the hardness formulas, we calculate the hardness of martensite, bainite and ferrite-pearlite.

7) HAZ hardness is then estimated as the weighted average based

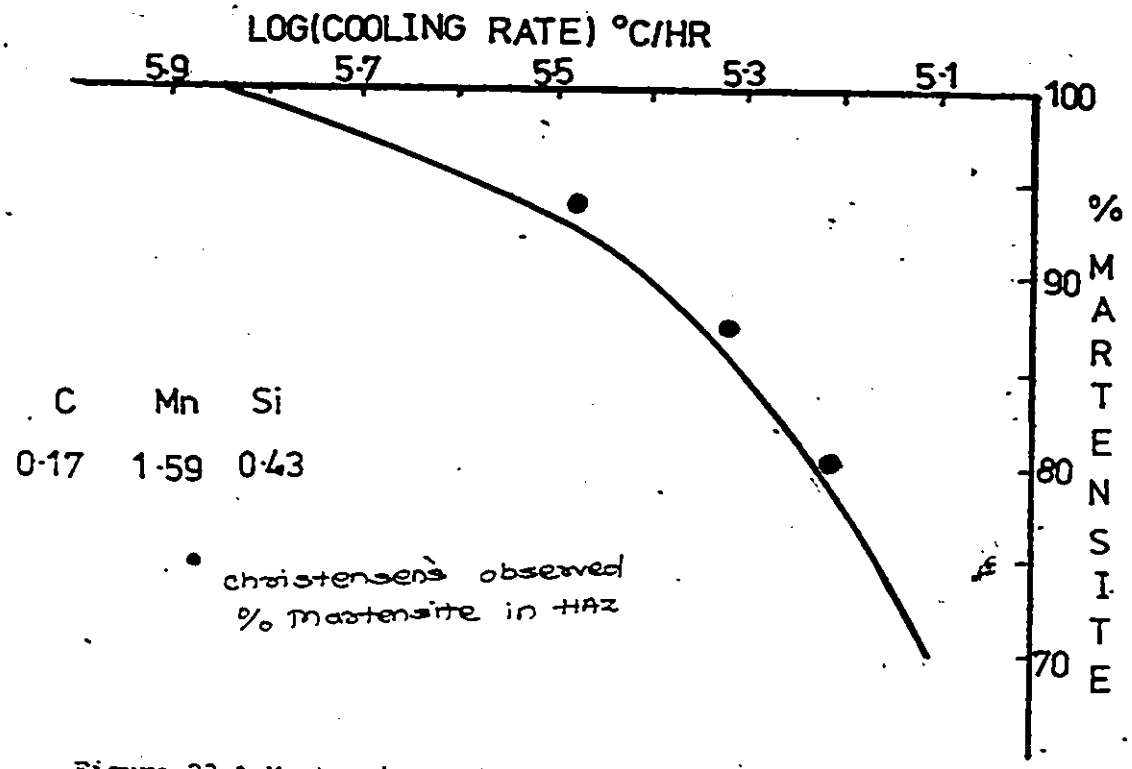

Figure 23 % Martensite and Cooling Rate Curve

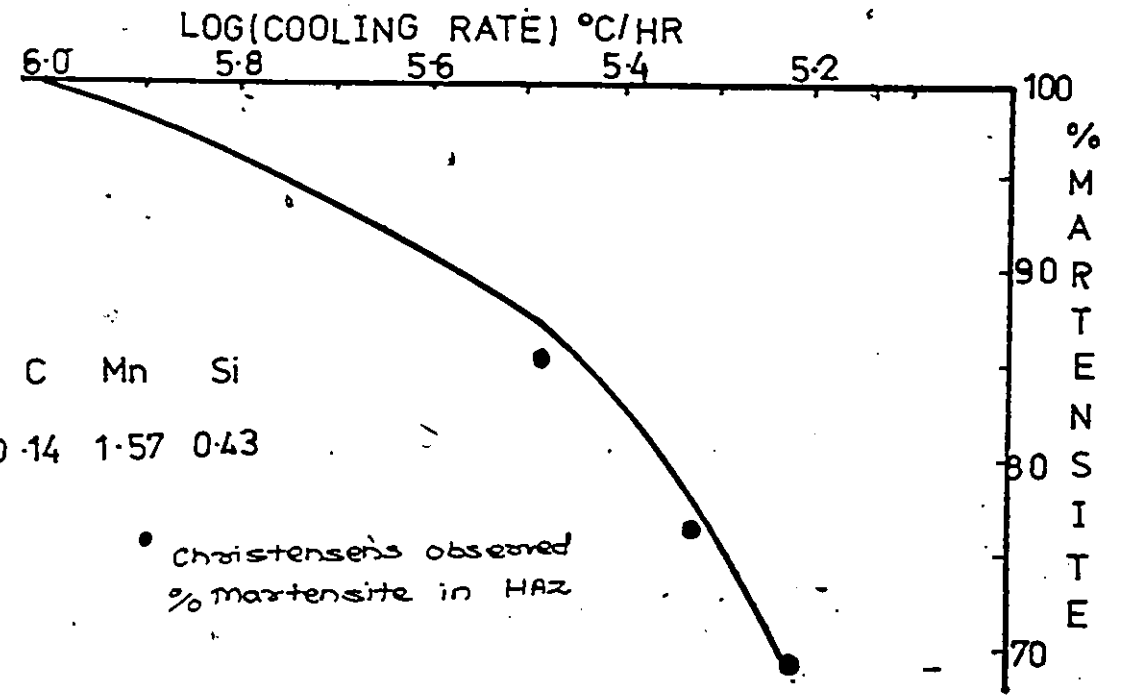

Figure 24 % martensite and Cooling Rate Curve

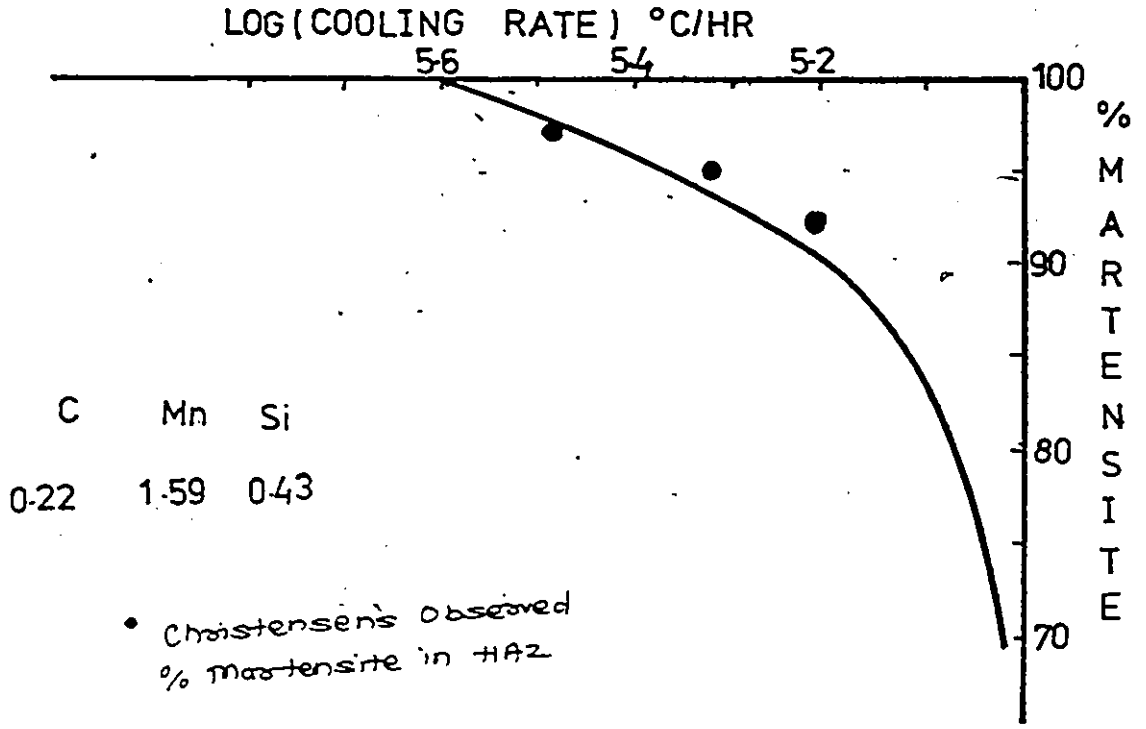

Figure 25 : Martensite and Cooling Rate Curve

on % products obtained in Step (5).

Thus, starting from the welding heat input, plate thickness and chemical composition, we can predict the HAZ % martensite and HAZ hardness.

Figures 26 and 27 show the comparison between the predicted and observed HAZ % martensite and HAZ hardness for Christensen's data.

Figure 28 shows a comparison between observed and predicted HAZ hardness for Ito-Bessyo data (Table XII).

4.3.4 Discussion

It is important to note that our prediction below 70% martensite loses accuracy in comparison to that between 100% and 70%. This limitation arises from the fact that we determine the curve between 90% and 50% martensite on the basis of V_1^{90} and V_1^{50}. In fact, over a large range of 40%, V_1^{90} and V_1^{80} cannot form a sound basis on which the curve can be founded. Only the availability of more basis points like V_1^{70}, V_1^{60}, etc. can improve the accuracy down to 50% martensite.

At this point, we are capable of predicting σ_{CR} for a given heat input, plate thickness, plate composition, preheat level and hydrogen level.

Section 4.2 predicts cooling rate. Section 4.3 predicts HAZ % martensite and hardness, and the correlation from Equation (19) gives us the σ_{CR}.

Figure 29 shows the comparison between the predicted and observed σ_{CR} for the Christensen's data given in Table XI.

Figures 30 and 31 show the Ito-Bessyo % weld cracking data

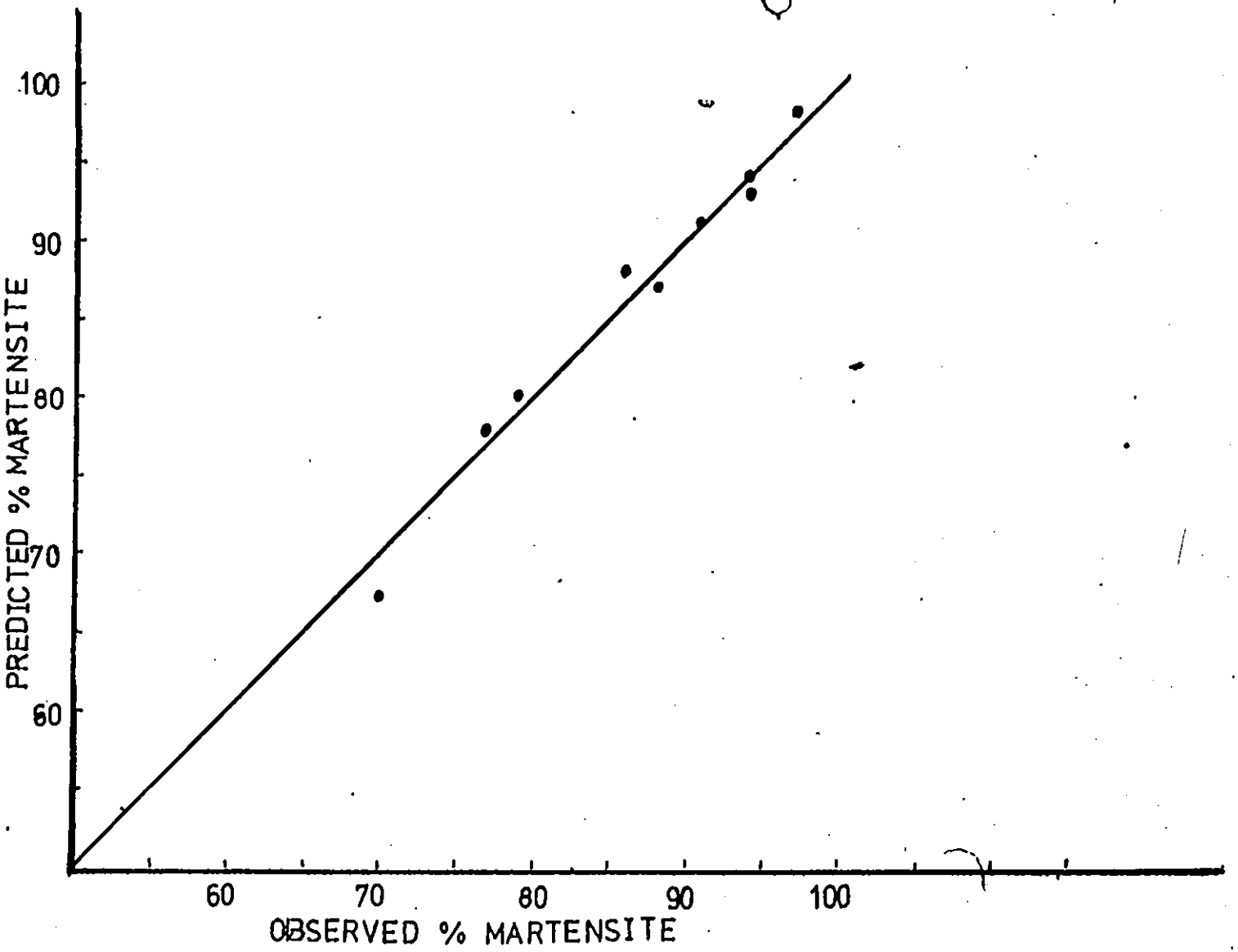

Figure 26 Comparison Between Predicted and Observed % Martensite for Christensen's Data

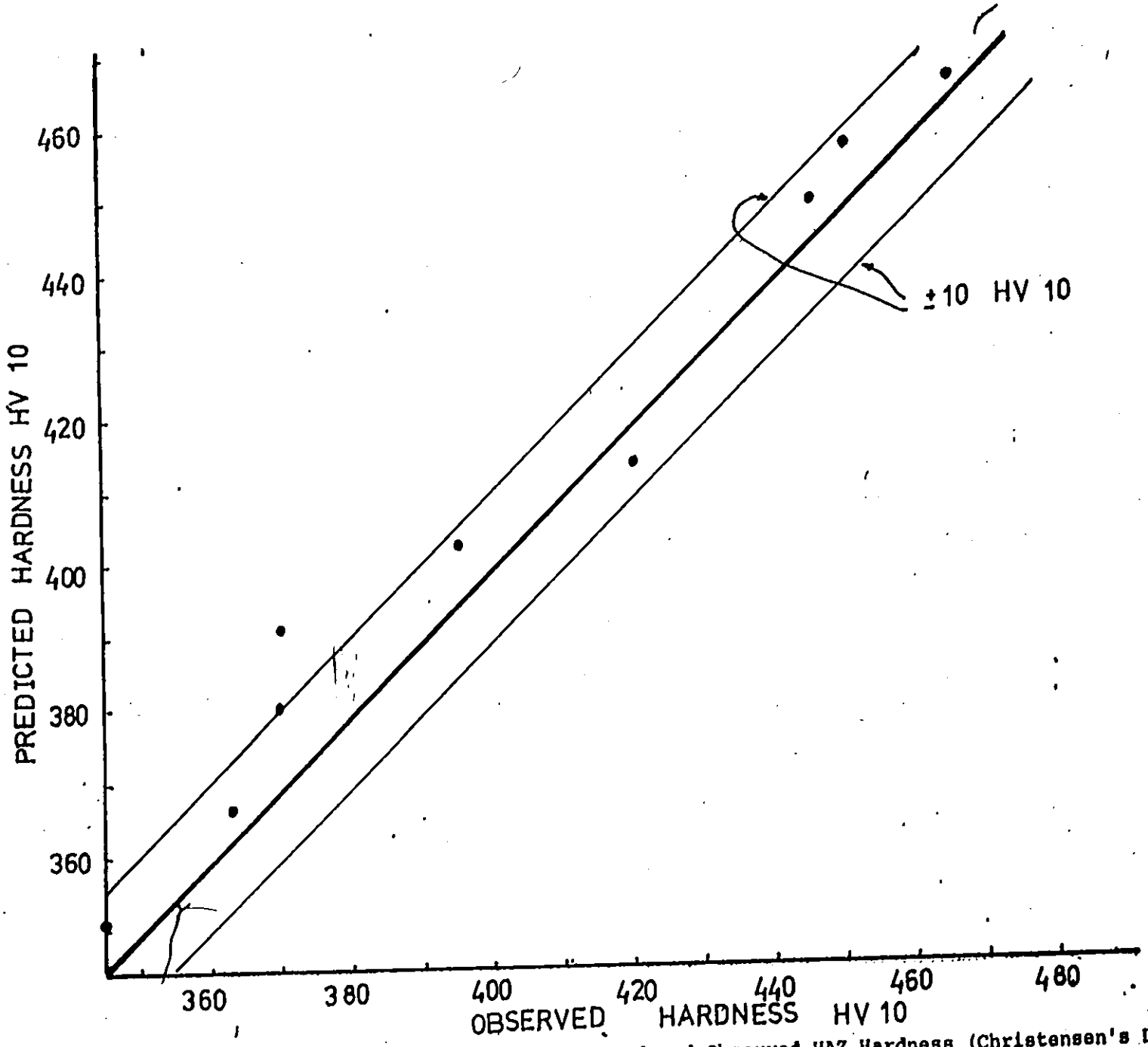

Figure 27 Comparison Between Predicted and Observed HAZ Hardness (Christensen's Data)

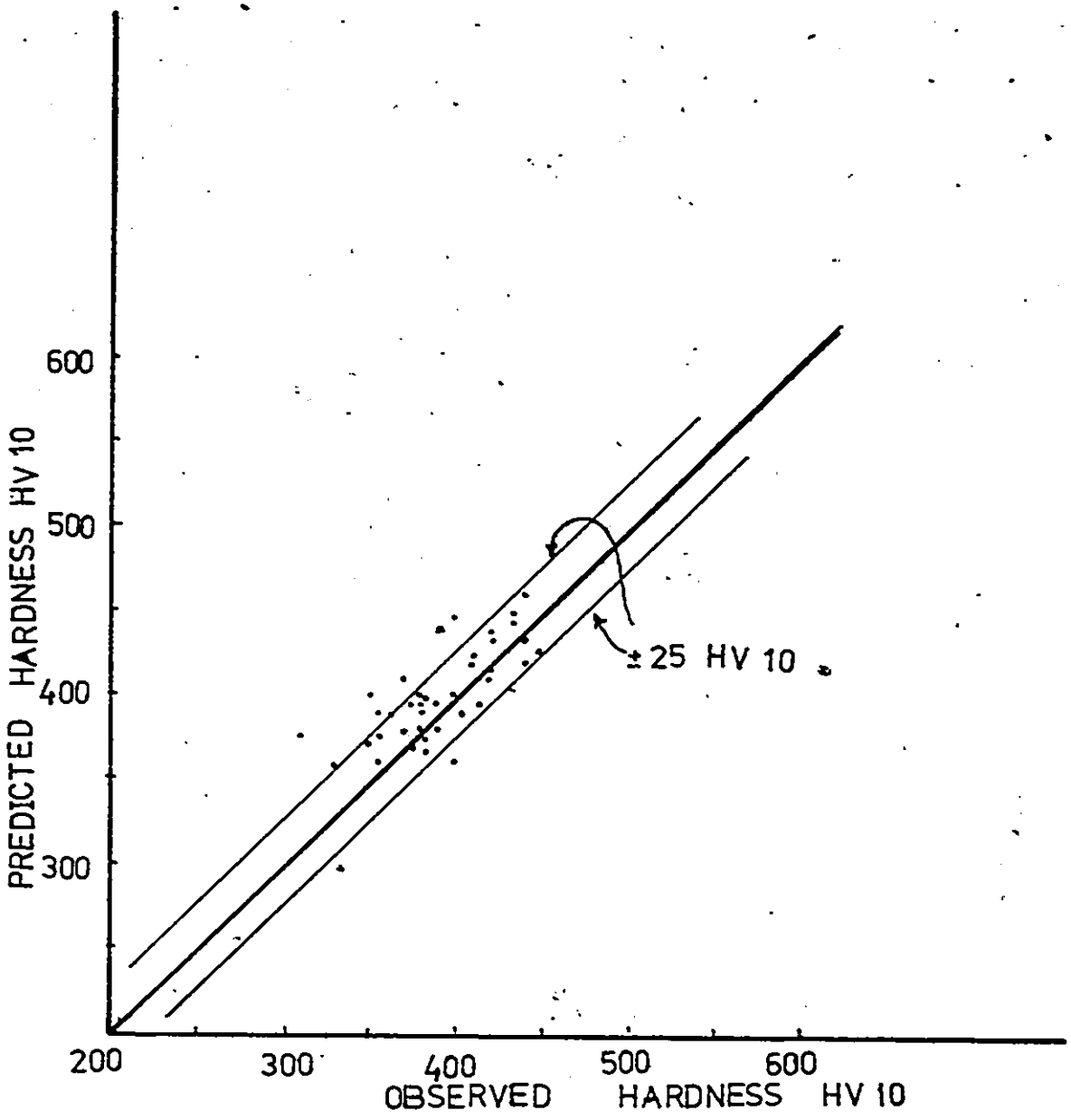

Figure 28 Comparison Between Predicted and Observed HAZ Hardness for Ito-Bessyo Data

TABLE XI

Prediction of σ_{CR} on the Basis of Heat Input, Plate Thickness, Plate Composition and Hydrogen Level

No.	Heat Input kJ/mm	C	Mn	Si	Hydrogen ppm	Observed σ_{CR} N/mm²	Predicted σ_{CR} N/mm²
1	0.9	0.140	1.57	0.43	7	325	313
2	1.3	0.140	1.57	0.43	3	500	483
3	1.3	0.140	1.57	0.43	7	375	366
4	1.3	0.140	1.57	0.43	30	175	166
5	1.7	0.140	1.57	0.43	7	440	417
6	0.9	0.170	1.59	0.43	7	250	266
7	1.3	0.170	1.59	0.43	3	400	403
8	1.3	0.170	1.59	0.43	[illegible]	300	306
9	1.3	0.170	1.59	0.43	30	130	138
10	1.7	0.170	1.59	0.43	7	350	346
11	0.9	0.215	1.59	0.43	7	215	194
12	1.3	0.215	1.59	0.43	3	320	305
13	1.3	0.215	1.59	0.43	7	240	231
14	1.3	0.215	1.59	0.43	30	100	105
15	1.7	0.215	1.59	0.43	7	275	256

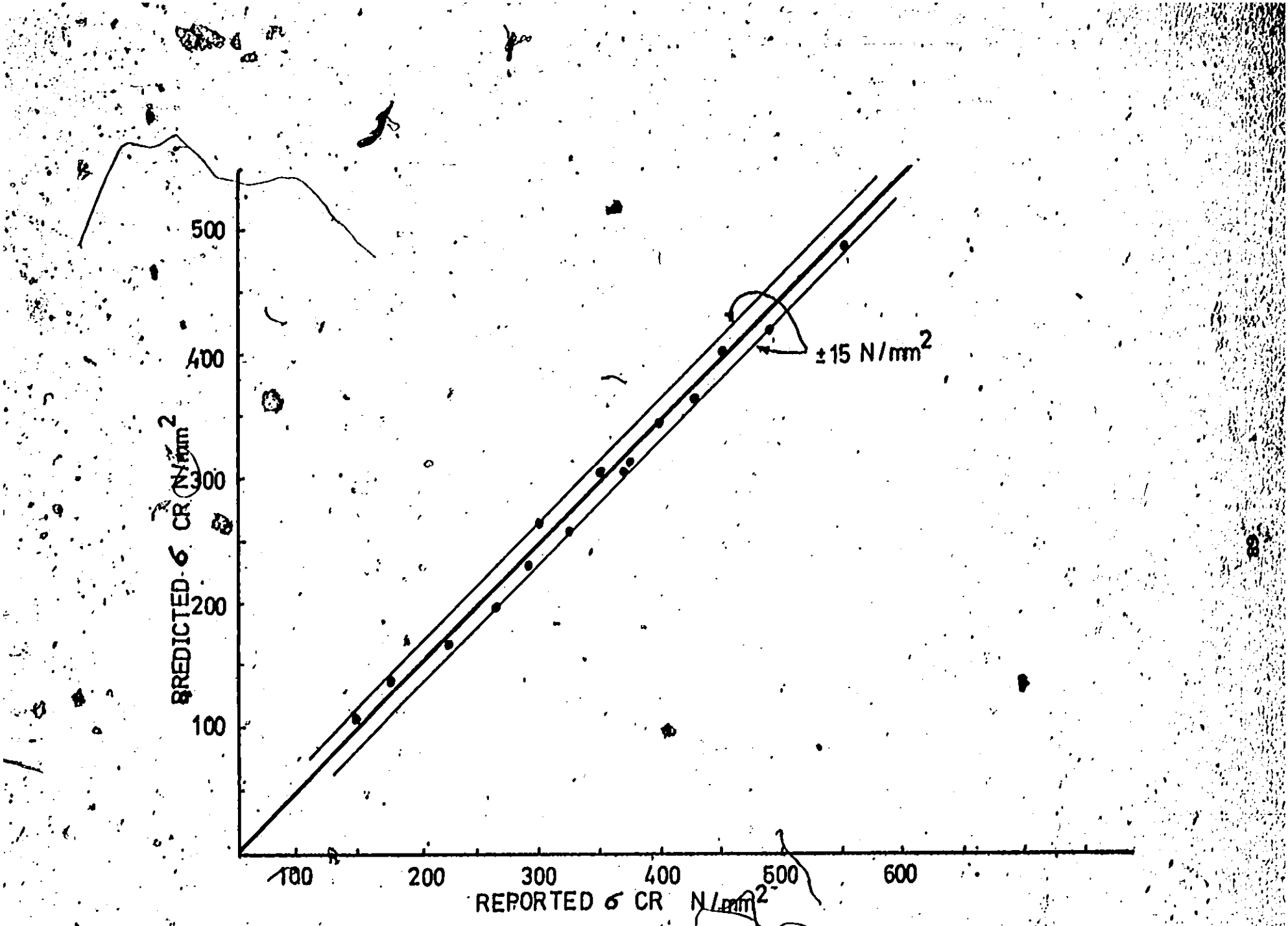

Figure 29 Comparison Between Predicted and Observed σ_{CR} for Christensen's Data

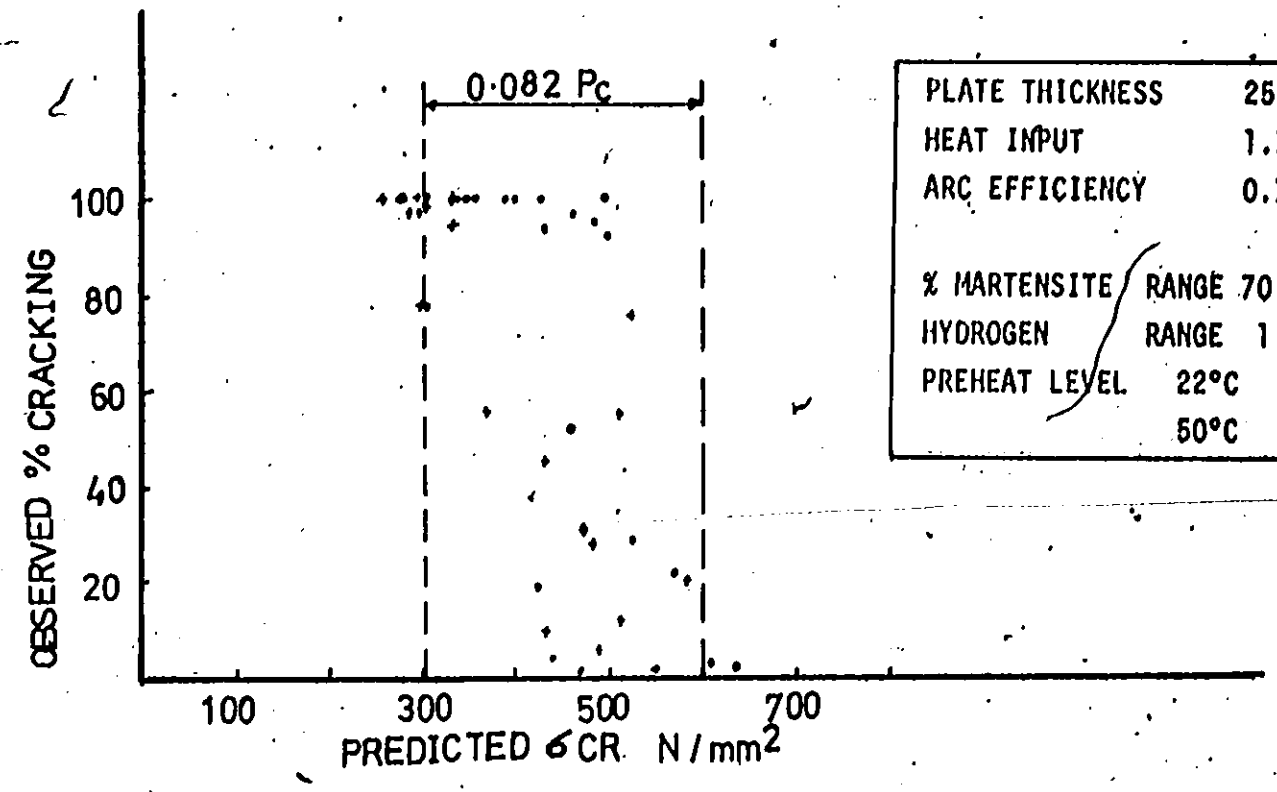

Figure 30 Plot of % Weld Cracking Against Predicted σ_{CR} for Ito-Bessyo Data

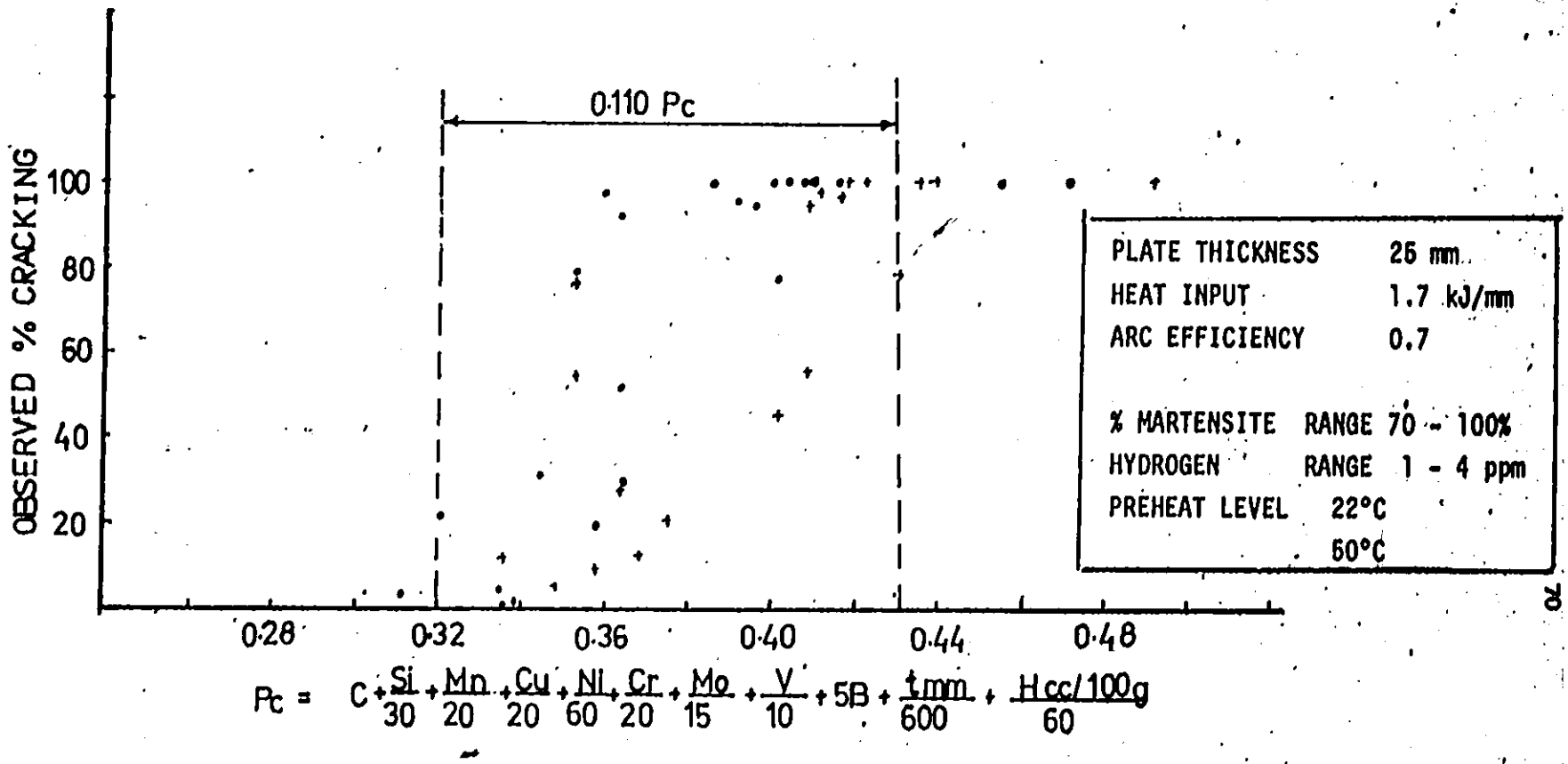

$$Pc = C + \frac{Si}{30} + \frac{Mn}{20} + \frac{Cu}{20} + \frac{Ni}{60} + \frac{Cr}{20} + \frac{Mo}{15} + \frac{V}{10} + 5B + \frac{t\,mm}{600} + \frac{H\,cc/100g}{60}$$

Figure 31 Plot of % Weld Cracking Against Ito-Bessyo Cracking Parameter P_c

(Table XII) plotted against predicted σ_{CR} and the cracking parameter P_c, respectively. One can see that for the Ito-Bessyo cracking parameter (P_c), obtained with linear optimization, the scatter band for % weld cracking is 0.110 P_c units. Our predicted σ_{CR} as a parameter operating without optimization on the same % weld cracking data shows a reduced scatter band of 0.082 P_c units. This comparison clearly shows that the predicted σ_{CR} based on HAZ % martensite, hardness and hydrogen level can serve as a very effective cracking parameter.

Thus, we can see that our system of prediction of σ_{CR} on the basis of heat input, plate thickness, plate composition and hydrogen level using heat transfer calculations, % martensite - composition - cooling rate relations, hardness - composition - cooling rate relations, and implant test correlation, provides a reliable, rapid and economic assessment of cold-cracking susceptibility of steel weldment.

It is important to remark here on the parameters which were adjusted to correctly predict the welding cooling rates, HAZ % martensite and hardness using the heat transfer calculations and published % martensite - composition - relations and hardness - composition - relations.

In the heat transfer calculations, the effective constant B_{3D} and arc efficiency are used as adjustable parameters to accurately predict cooling rates and time appropriate to the welding conditions and temperatures of interest. In regard to the % martensite - composition - cooling rate - relations and hardness - composition - cooling rate relations, the base constants in the linear relations have been slightly adjusted for Christensen's[23] HAZ % martensite and hardness observations

pertaining to the welding conditions.

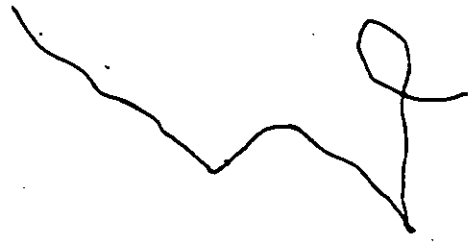

TABLE XII

Prediction of HAZ Hardness and σ_{CR} for the Ito-Bessyo Data

ID NO.	C	Mn	Si	Ni	Cr	Mo	V	Plate Thick ness	Heat Input Lovl.	Pre-Heat Lovl.	% Mart ensi to.	HAZ hard- ness Obsvd.	HAZ hard- ness Prodl	Hydr ogen Lovl	% Crac king	σ_{CR}
								mm	KJ/mm	°C		VHN 10Kg	VHN 10Kg	ppm		N/mm²
10	0.16	0.86	0.29	0.00	0.85	0.60	0.00	25	1.7	22	93	450	425	2	100	398
12	0.15	0.92	0.52	1.06	0.00	0.62	0.07	38	1.7	22	95	433	420	2	98	389
13	0.16	1.37	0.28	1.10	0.87	0.00	0.07	25	1.7	22	100	433	448	2	77	308
14	0.15	1.26	0.51	1.06	0.34	0.64	0.00	38	1.7	22	100	437	443	2	100	314
16	0.16	1.41	0.30	0.00	0.00	0.61	0.07	25	1.7	22	95	437	419	2	100	392
21	0.11	1.34	0.50	1.05	0.00	0.61	0.00	25	1.7	22	98	405	390	4	100	332
22	0.11	1.40	0.31	1.00	0.00	0.00	0.06	38	1.7	22	88	333	374	4	73	409
23	0.09	1.32	0.30	0.00	0.80	0.63	0.07	38	1.7	22	96	383	368	4	100	364
25	0.17	0.94	0.55	0.00	0.82	0.00	0.00	25	1.7	22	70	417	410	4	100	495
26	0.15	0.77	0.26	0.00	0.85	0.60	0.00	0	1.7	22	92	425	412	4	98	361

Poor Copy

TABLE XII

(continued)

ID NO.	C	Mn	Si	Ni	Cr	Mo	V	Plate Thickness	Heat Input	Pre-Heat Level	% Martensite	HAZ hardness Observed	HAZ hardness Predicted	Hydrogen Level	% Cracking	σ_{CR}
								mm	KJ/mm	°C		VHN 10Kg	VHN 10Kg	ppm		N/mm²
28	0.15	0.83	0.50	1.05	0.00	0.60	0.07	25	1.7	22	93	421	415	4	100	351
29	0.13	1.21	0.26	1.09	0.93	0.00	0.07	38	1.7	22	99	442	417	4	99	299
30	0.14	1.39	0.57	1.10	0.75	0.63	0.00	25	1.7	22	100	442	435	4	100	275
32	0.15	1.40	0.33	0.00	0.00	0.66	0.00	38	1.7	22	95	417	411	4	100	340
46	0.22	1.30	0.26	0.00	0.00	0.00	0.00	25	1.7	24	80	397	447	2	29	517
67	0.14	1.43	0.28	0.44	0.00	0.12	0.03	25	1.7	23	88	376	395	2	31	477
66	0.11	1.50	0.16	0.29	0.17	0.16	0.00	38	1.7	23	88	348	369	2	24	492
68	0.14	1.43	0.28	0.44	0.00	0.12	0.03	38	1.7	23	88	380	396	2	51	468
73	0.16	1.29	0.28	0.32	0.00	0.00	0.07	38	1.7	14	76	0	393	4	100	458
74	0.16	1.29	0.28	0.32	0.00	0.00	0.07	38	1.7	14	76	0	393	1	11	606

Poor Copy

TABLE XII

(continued)

ID NO.	C	Mn	Si	Ni	Cr	Mo	V	Plate Thick noss	Heat Input	Pre-Heat Levl.	% Mart ensi to.	HAZ hard-noss Obsvd.	HAZ Hydr hard-ogen noss Prodi	Hydr Levl	% Crac king	δ_{CR}
								mm	KJ/mm	°C		VHN 10Kg	VHN 10Kg	ppm		N/mm²
75	0.16	1.29	0.28	0.32	0.00	0.00	0.07	25	1.7	14	75	0	392	4	97	462
76	0.16	1.29	0.28	0.32	0.00	0.00	0.07	32	1.7	14	76	0	393	4	100	458
77	0.16	1.29	0.28	0.32	0.00	0.00	0.07	25	1.7	14	75	0	393	1	3	612
78	0.16	1.28	0.28	0.32	0.00	0.00	0.07	32	1.7	14	76	0	393	1	6	606
79	0.16	1.29	0.28	0.32	0.00	0.00	0.07	25	1.7	14	75	0	392	2	22	575
80	0.16	1.29	0.28	0.32	0.00	0.00	0.07	32	1.7	14	76	0	393	2	33	570
81	0.16	1.29	0.28	0.32	0.00	0.00	0.07	38	1.7	14	76	0	392	2	16	570
88	0.16	1.37	0.32	0.30	0.00	0.00	0.09	20	1.7	14	73	353	389	2	0	575
89	0.16	1.32	0.37	0.33	0.00	0.00	0.10	27	1.7	20	78	382	399	2	54	539
90	0.14	1.34	0.34	0.34	0.00	0.00	0.08	28	1.7	18	73	310	375	2	0	587

Poor Copy

TABLE XII

(continued)

ID NO.	C	Mn	Si	Ni	Cr	Mo	V	Plate Thick ness	Heat Input Lovl.	Pre-Heat Lovl.	% Mart ensi to.	HAZ hard-ness Obsvd.	HAZ hard-ness Prodr	Hydr ogen Lovl	% Crac king	CR
								mm	KJ/mm	°C		VHN 10Kg	VHN 10Kg	ppm		N/mm²
91	0.15	1.46	0.31	0.28	0.00	0.00	0.09	30	1.7	18	82	388	396	2	4	515
92	0.15	1.42	0.31	0.27	0.00	0.00	0.09	32	1.7	14	79	362	392	2	40	533
94	0.15	1.30	0.37	0.31	0.00	0.00	0.09	32	1.7	16	72	373	382	2	72	588
96	0.13	1.45	0.34	0.30	0.00	0.00	0.09	36	1.7	18	77	354	373	2	85	562
98	0.16	1.35	0.35	0.32	0.00	0.00	0.10	38	1.7	21	79	382	400	2	13	532
104	0.10	0.84	0.30	0.87	0.48	0.46	0.05	27	1.7	19	91	377	369	2	28	466
105	0.11	0.84	0.29	0.90	0.54	0.48	0.05	27	1.7	17	93	390	381	2	70	442
106	0.11	0.82	0.24	0.89	0.56	0.47	0.06	27	1.7	21	92	380	379	2	21	446
107	0.12	0.80	0.24	0.87	0.56	0.47	0.06	27	1.7	20	93	388	388	2	45	436
110	0.14	0.96	0.28	1.07	0.68	0.58	0.02	25	1.7	12	99	0	421	2	100	340

Poor Copy

TABLE XII

(continued)

ID NO.	C	Mn	Si	Ni	Cr	Mo	V	Plate Thick ness	Heat Input Lovl.	Pre-Heat Lovl.	% Mart ensi te.	HAZ hard- ness Obsvd.	HAZ hard-ness Prodl	Hydr ogen Lovl	% Crac king	6CR
								mm	KJ/mm	°C		VHN 10Kg	VHN 10Kg	ppm		N/mm2
122	0.17	0.82	0.47	0.00	1.18	0.52	0.06	25	1.7	12	95	0	447	2	100	356
123	0.14	0.61	0.28	0.00	1.06	0.46	0.00	25	1.7	17	84	0	396	2	92	500
124	0.15	0.69	0.34	0.00	1.06	0.47	0.08	25	1.7	17	90	0	415	2	94	433
125	0.15	0.70	0.37	0.00	1.05	0.50	0.03	25	1.7	17	91	0	417	2	100	427
126	0.14	0.59	0.30	0.00	1.12	0.47	0.05	25	1.7	17	85	0	399	2	95	486
135	0.12	0.99	0.29	0.00	0.35	0.45	0.08	50	1.7	15	76	401	382	2	45	571
138	0.11	1.50	0.16	0.29	0.17	0.16	0.00	50	1.7	23	88	351	369	2	50	486
139	0.14	1.43	0.28	0.44	0.00	0.12	0.03	50	1.7	23	88	382	396	2	77	468
146	0.07	0.87	0.51	1.05	0.81	0.61	0.07	50	1.7	22	95	357	359	2	100	438
147	0.08	1.29	0.53	1.03	0.00	0.61	0.00	50	1.7	22	96	383	360	2	100	437

Poor Copy

TABLE XII

(continued)

ID NO.	C	Mn	Si	Ni	Cr	Mo	V	Plate Thick ness	Heat Input Lovl.	Pre-Heat Lovl.	% Mart ensi to.	HAZ hard-ness Obsvd.	HAZ hard-ness Predi	Hydr ogen Lovl	% Crac king	6CR
								mm	KJ/mm	°C		VHN 10Kg	VHN 10Kg	ppm		N/mm²
149	0.16	1.44	0.55	0.00	0.00	0.00	0.00	50	1.7	22	71	413	395	4	100	488
151	0.09	1.44	0.34	0.00	0.87	0.63	0.08	50	1.7	22	98	383	374	4	100	342
152	0.17	0.91	0.30	1.09	0.00	0.00	0.00	50	1.7	22	80	370	409	4	100	432
153	0.17	1.40	0.29	1.11	0.88	0.00	0.07	50	1.7	22	100	442	459	4	100	248
167	0.13	1.29	0.24	0.00	0.00	0.60	0.00	38	1.7	20	91	0	384	3	92	400
168	0.16	1.30	0.29	0.30	0.00	0.00	0.08	38	1.7	20	75	0	392	1	7	616
169	0.11	0.77	0.23	0.96	0.61	0.52	0.03	38	1.7	20	93	0	380	1	29	507
170	0.12	0.68	0.15	0.83	0.52	0.44	0.02	38	1.7	20	88	0	378	1	1	554
171	0.42	0.56	0.26	0.00	1.07	0.48	0.05	38	1.7	20	76	0	369	1	24	655
194	0.14	1.36	0.32	0.00	0.00	0.63	0.00	25	1.7	22	93	0	398	2	4	439

Poor Copy

TABLE XII

(continued)

ID NO.	C	Mn	Si	Ni	Cr	Mo	V	Plate Thick ness	Heat Input	Pre-heat Level	% Mart ensite	HAZ hard-ness Obsvd.	HAZ hydr hard-ness Prodi	ogen Level	% Crac king	CR
								mm	KJ/mm	°C		VHN 10Kg	VHN 10Kg	ppm		N/mm²
195	0.15	1.35	0.30	0.00	0.00	0.63	0.00	25	1.7	22	93	0	408	2	19	427
197	0.18	1.28	0.30	0.00	0.00	0.31	0.00	25	1.7	22	87	0	424	2	0	468
198	0.18	1.30	0.32	0.00	0.00	0.30	0.00	25	1.7	22	88	0	426	2	52	460
199	0.17	1.48	0.37	0.00	0.00	0.00	0.08	25	1.7	22	78	0	407	2	0	548
9	0.15	1.35	0.30	0.00	0.00	0.63	0.00	25	1.7	50	93	0	406	2	9	433
11	0.18	1.28	0.30	0.00	0.00	0.31	0.00	25	1.7	50	85	0	420	2	5	489
12	0.18	1.30	0.32	0.00	0.00	0.30	0.00	25	1.7	50	85	0	422	2	28	483
13	0.17	1.29	0.27	0.00	0.00	0.31	0.00	25	1.7	50	83	0	408	2	12	513

TABLE XII

(continued)

ID NO.	C	Mn	Si	Ni	Cr	Mo	V	Plate Thick ness	Heat Input Lovl. mm	Pre-heat Lovl. KJ/mm	% Mart ensi to. °C	HAZ hard-ness Obsvd. VHN 10Kg	HAZ hard-ness Predl VHN 10Kg	Hydr ogen Lovl ppm	% Crac king	CR N/mm2
14	0.17	1.48	0.37	0.00	0.00	0.00	0.08	25	1.7	50	74	0	400	2	0	580
16	0.18	1.43	0.35	0.00	0.00	0.00	0.08	25	1.7	50	73	0	406	2	20	579
41	0.16	1.04	0.36	0.69	0.88	0.50	0.08	25	1.7	50	99	0	442	3	78	304
42	0.21	1.24	0.35	1.04	1.13	0.62	0.07	25	1.7	50	100	0	499	1	100	260
43	0.16	0.96	0.32	0.00	0.63	0.28	0.05	25	1.7	50	81	0	405	2	55	509
44	0.16	1.05	0.37	0.00	0.62	0.61	0.08	25	1.7	50	94	0	426	4	94	336
45	0.16	1.25	0.27	0.00	1.13	0.29	0.05	25	1.7	50	97	0	438	4	97	296
46	0.17	1.35	0.37	0.00	1.17	0.60	0.08	25	1.7	50	100	0	455	2	100	296
47	0.19	0.96	0.31	0.00	1.14	0.27	0.08	25	1.7	50	95	0	460	4	99	301
48	0.18	0.99	0.32	0.00	1.15	0.59	0.05	25	1.7	50	98	0	456	2	100	324

Poor Copy

TABLE XII
(continued)

ID NO.	C	Mn	Si	Ni	Cr	Mo	V	Plate Thickness	Heat Input Levl.	Pre-Heat Levl.	% Martensite.	HAZ hardness Obsvd.	HAZ hardness Predl	Hydrogen Levl	% Cracking	P_{cm}
								mm	KJ/mm	°C		VHN 10Kg	VHN 10Kg	ppm		N/mm²
49	0.19	1.42	0.37	0.00	0.79	0.31	0.08	25	1.7	50	98	0	464	2	100	307
50	0.17	1.07	0.22	0.00	0.85	0.59	0.05	25	1.7	50	0	438	96	5	97	285
56	0.15	0.68	0.33	0.36	0.61	0.44	0.04	25	1.7	50	0	410	88	4	55	367
61	0.15	0.83	0.31	0.31	0.35	0.43	0.04	25	1.7	50	0	390	80	2	77	525
62	0.15	0.74	0.33	0.31	0.73	0.28	0.04	25	1.7	50	0	394	78	5	45	428
77	0.16	1.29	0.28	0.32	0.00	0.00	0.07	38	1.7	50	0	384	70	4	79	495
78	0.16	1.29	0.28	0.32	0.00	0.00	0.07	38	1.7	50	0	384	70	1	8	657
103	0.16	1.35	0.35	0.32	0.00	0.00	0.10	38	1.7	50	0	395	76	2	10	532

CHAPTER 5

DETERMINATION OF PRACTICAL WELDING PROCEDURES ON THE BASIS OF IMPLANT TEST

5.1 General Remarks

A large number of small scale weldability tests (bead-on-plate, cruciform, Reeve, bend angle, CTS, Lehigh, Tekken, RRC, TRC) have been developed to cope with the urgent need of developing welding procedures that would prevent an occurrence of cold-cracking on actual welded structures. However, a method that would successfully permit us to transpose, in a quantitative manner, results of small scale cracking tests, is still lacking.

5.2 Relation Between Implant Test and Other Restraint Tests

Implant testing has an advantage of offering quantitative assessment of cold-cracking susceptibility in terms of the lower critical implant fracture stress. In order to transpose the results of the implant test to actual welding structures, Satoh et al[43] carried out experiments to find out the correlation of implant tests and RRC-TRC tests. They found that the lower critical stress obtained by implant tests is almost equal to the critical stress obtained by RRC and TRC tests (see Figure 32). This finding is quite important for transposing the implant test results to the actual welded structures. Thus, if based on weld joint geometry and restraint, one can estimate the reaction stresses in the critical region of the HAZ, a criterion that the

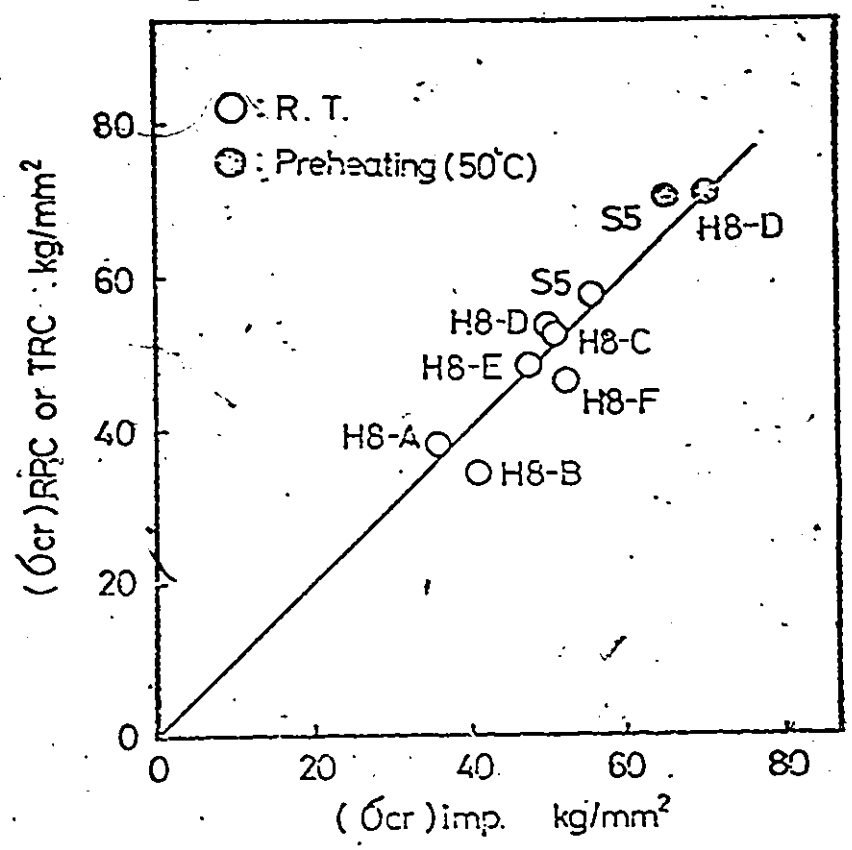

Figure 32. Comparison Between σ_{CR} Obtained from Implant Test and from RRC and TRC Tests (43)

reaction stress should not be greater than the lower critical implant fracture stress (σ_{CR}) can be used to recommend safe welding procedures.

5.3 Determination of Preheat To Avoid Cracking

With our ability to predict σ_{CR} for a given welding heat input, plate thickness, hydrogen level and plate composition (Chapter 3), we can have a complete system of establishing safe welding procedures.

Figure 33 shows the block diagram of our basic criterion to avoid cold-cracking in welded construction.

Figure 34 shows a schematic representation of the procedure we follow for presumption of preheating temperature to avoid cracking in actual weld joints from intensity of restraint, on the basis of implant test results. We assume that for multipass welds, first pass is critical and preheat temperature predicted for the first pass can be treated as mimimum interpass temperature.

There are two features which must be considered for predicting the preheat level for a given welded joint:

1) We must estimate the reaction stress developed in the joint as a function of weld configuration, joint geometry, and loading on the joint during the welding process or in service.

2) To arrive at a preheat - implant stress relationship, we have noted that preheat not only affects the cooling rate and hence HAZ microstructure, but it also allows more hydrogen to diffuse out of the joint. Thus, the effect of preheat is twofold:

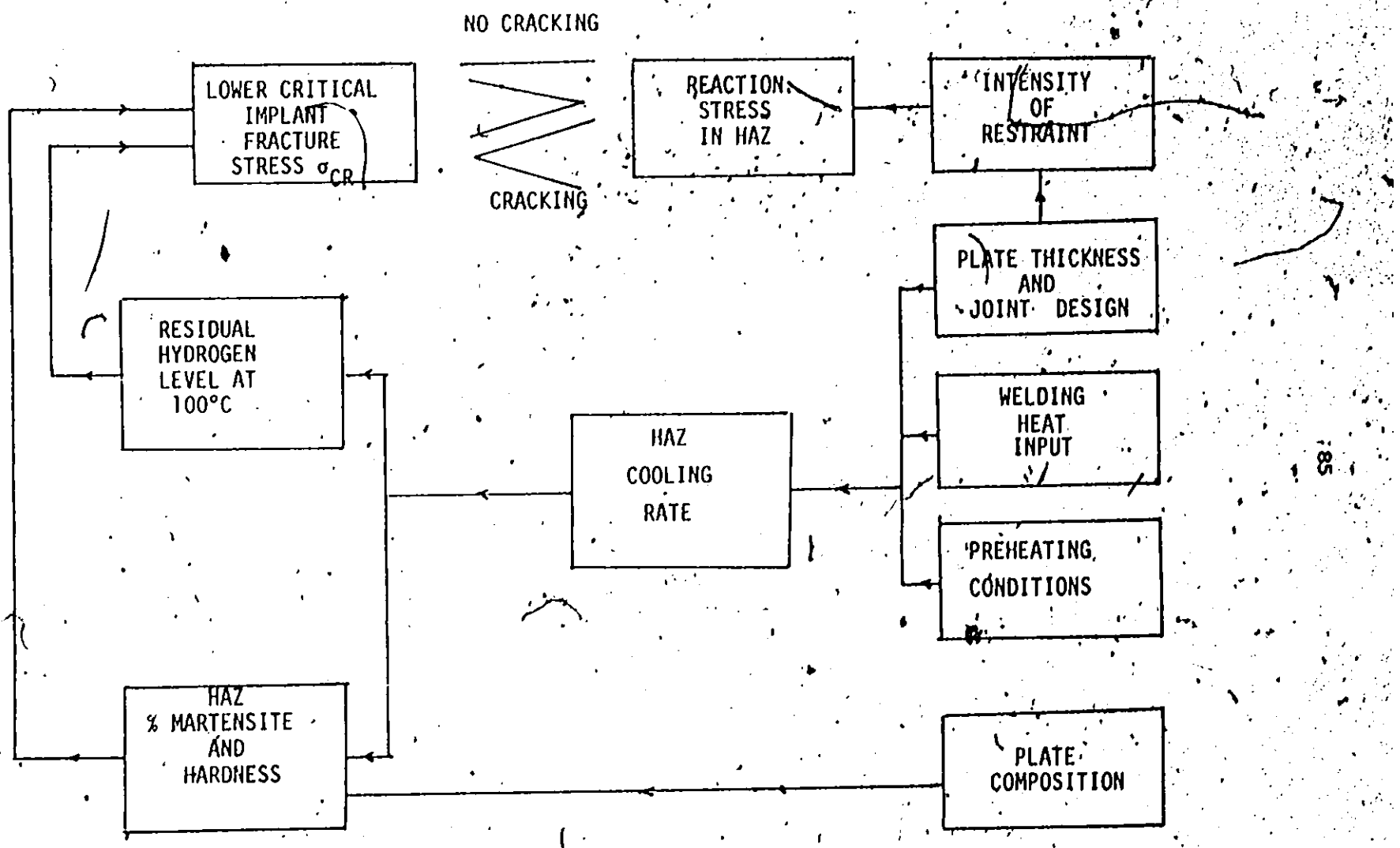

Figure 33 Criterion for Avoiding Cold-Cracks In Welded Structures

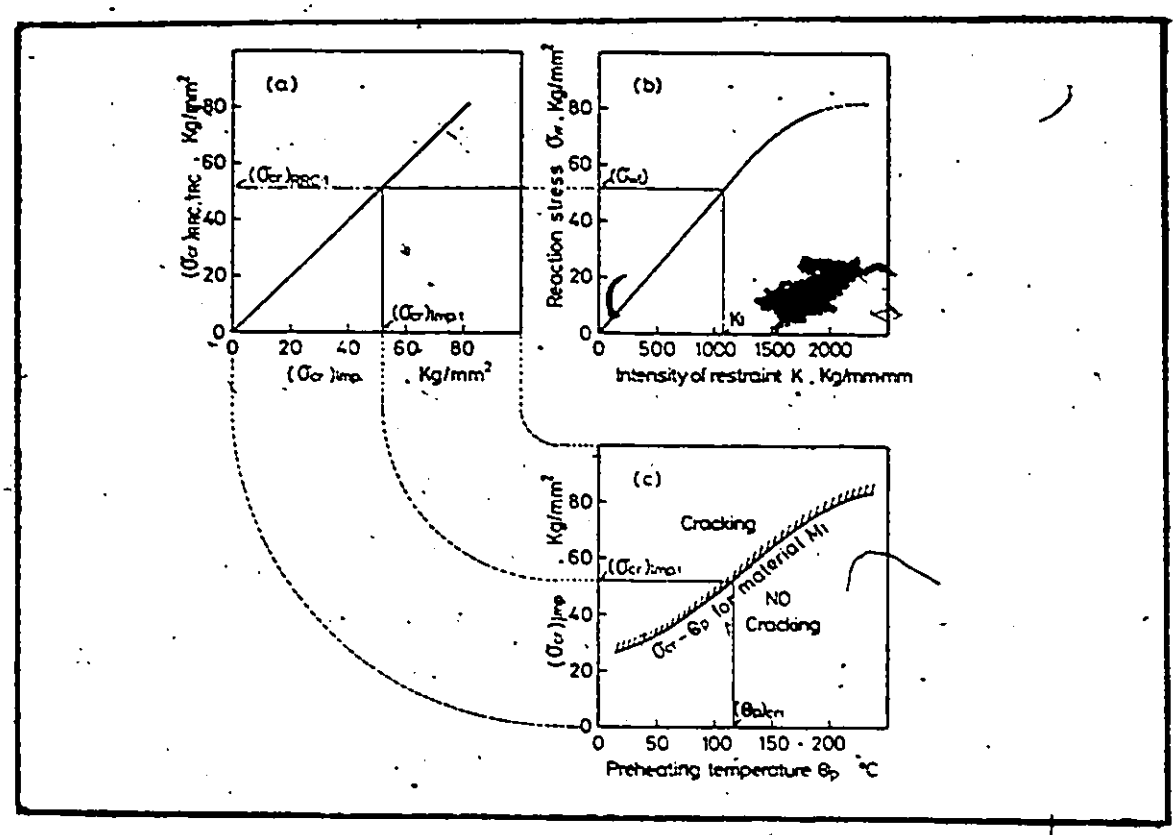

Figure 34 Procedure for Recommending Preheat to Avoid Cracking

(a) change of microstructure,

(b) reduction of residual hydrogen level in the HAZ.

5.3.1 Estimation of Reaction Stress Developed in the Weld

As for the aspect (1) above, we leave this to the design engineers. They can accurately estimate the reaction stresses that may develop in the joint. However, for a simple configuration of a butt weld, the reaction stress developed can be estimated by:(43)

$$\sigma_w = mK \tag{56}$$

where m is a numerical factor given by:

$$m = \alpha\left(\frac{HWS \cdot H \cdot \tan\theta}{C}\right)^{1/2}$$

α = coefficient of thermal expansion

HWS = maximum temperature of weld metal

C = specific heat

2θ = bevel angle

H = 1.2×10^3 to 2.5×10^3 cal/gm.

K = intensity of restraint in kg/mm^2

defined as the magnitude of the reaction force per unit weld length necessary to produce average elastic change of unit magnitude in the root gap along the weld line.

Under a high intensity of restraint, the final reaction stress σ_w deviates from the proportional relationship in Equation (56) and approaches a constant value nearly equal to the tensile strength of the weld metal. The actual measurements of the intesntiy of restraints on the welded joints in various constructions are shown in Figure 35.

If the K value is taken to be 40 x the plate thickness, it is usually considered to be safe. THus, if the plate thickness is known, we can have the worst condition estimate of the reaction stress in the HAZ.

5.3.2 Influence of Preheat on Residual Hydrogen Level

For the second aspect of the effect of the preheat on the residual hydrogen level, we proceed as follows: Tadaomi Fujii[44] has carried out a theoretical analysis of the diffusion of hydrogen through the weld. He substituted a single pass of weld metal by a model bead having rectangular cross-section of effective thickness (Le), as shown in Figure 36. He assumed, for simplicity, that hydrogen absorbed in the molten metal diffuses only to the upper surface of the weld during the cooling process, after the weld metal solidifies.

Thus, the boundary conditions for the diffusion problem are:

$$\left(\frac{\partial (C/Co)}{\partial (x/Le)}\right)_{\frac{x}{Le}=0} = 0 \qquad \text{No hydrogen diffuses into the plate} \qquad (57)$$

$$(C/Co)_{\frac{x}{Le}=1} = 0 \qquad \text{Hydrogen concentration at the top surface = 0} \qquad (58)$$

for uniformly constant initial hydrogen content Co. It can be shown that for

$$\tau = \frac{Dt}{Le^2} >> 0$$

where D = diffusion coefficient; t = time; Le = effective bead thickness, we get:

$$\bar{U} = \bar{C}/Co = \frac{8}{\pi^2} e^{-\frac{\pi^2}{4}\tau} \qquad (59)$$

where $\bar{C}$ is the average concentration of the residual hydrogen in the weld.

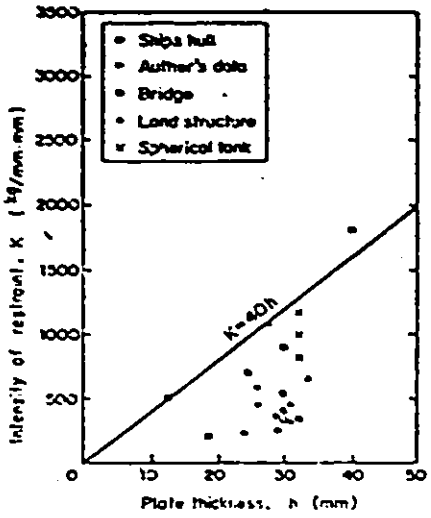

Figure 35 Intensity of Restraint vs Plate Thickness for Welded Construction[43]

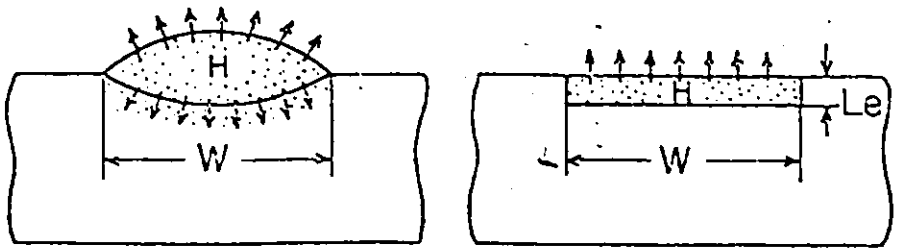

(a) Actual weld metal (b) Model weld metal

Figure 36 Bead Model For Hydrogen Diffusion Analysis

It is known that cracking occurs below 100°C and hence, the residual hydrogen content is important when the weld has cooled to 100°C. Thus, for the weld carried out without preheat; if $\bar{C}_{20°C}$ is the hydrogen content measured by the IIW procedure, we have:

$$\frac{\bar{C}_{20°C}}{Co} = \frac{8}{\pi^2} e^{-\frac{\pi^2}{4}} \times \tau_{20°C} \tag{60}$$

where $\tau_{20°C}$ is the time factor for weld without preheat.

If the $\bar{C}_{PH}$ is the residual hydrogen content in the case of preheat, we have:

$$\frac{\bar{C}_{PH}}{Co} = \frac{8}{\pi^2} e^{-\frac{\pi^2}{4}} \times \tau_{PH} \tag{61}$$

where τ_{PH} is the time factor in the case of preheat. Co is the same for both the cases because the initial hydrogen concentration is the same. Thus, from Equations (60) and (61), we have:

$$\ln \frac{\bar{C}_{20°C}}{Co} - \ln \frac{\bar{C}_{PH}}{Co} = \frac{\pi^2}{4} (\tau_{PH} - \tau_{20°C})$$

or

$$\ln \bar{C}_{PH} = \ln \bar{C}_{20°C} - \frac{\pi^2}{4} (\tau_{PH} - \tau_{20°C}) \tag{62}$$

Since $\bar{C}_{20°C}$ can be found from the IIW testing procedure, knowledge of $(\tau_{PH} - \tau_{20°C})$ can give us $\bar{C}_{PH}$.

From the preheat experiments with RRC tests, it is observed that the time interval between 300 and 100°C is important. Since the time spent in this interval is considerably longer than that spent above 450°C, we only need to evaluate $(\tau_{PH} - \tau_{20°C})$ in the range 450°C to 100°C.

For our range of calculations, the hydrogen diffusion coefficient varies as follows:[44]

$$D = 1.4 \times 10^{-3} \exp(-3200/RT) \quad (523°k \leq T < 773°k) \ cm^2/sec$$

$$D = 0.12 \exp(-7820/RT) \quad (T < 523°k) \quad cm^2/sec \qquad (63)$$

Thus, by dividing the weld cooling curve into small temperature segments and using the equation:

$$\tau = \sum Di\Delta ti/Le^2 = X/Le^2 \qquad (64)$$

where Di = diffusion coefficient for temperature Ti

Δti = time defined as ti-ti-1

ti = time to cool to Ti

X = thermal factor defined as $\sum Di\Delta ti$

For estimating Le for a given welding procedure, we use the relation developed by Bradstreet:[45]

$$A = \frac{(ES^{1/3})^{5/4}}{3310} \qquad (65)$$

where A is the area of the weld cross section in square inches

S is the weld travel speed in ipm

E is Heat Input (kJ/in.).

We then introduce

$$-Le^2 = \frac{2\pi Ax6.25 \ cm^2}{\pi} \qquad (66)$$

5.3.3 Prediction of Preheat Level to Prevent Cracking

Using the cooling cycle prediction as per the equations in Section 4.2, along with Equations (62) to (66), we can predict the residual level of hydrogen for a given preheat level. Thus, variation of σ_{CR} with preheat can be predicted.

Based on the analysis covered in Chapters 3 and 4, we have developed a computer programme (see Appendix II) to predict the preheat levels of safe welding for the heat input, plate thickness, plate composition, hydrogen level range covered in the completely empirical British Welding Standard[46] (BS 5135: 1974). The comparison between recommended (by B.S. Standard) and predicted (by our programme) preheats (Figures 37 to 44) shows the conservative nature of the British Standard recommended procedures. Tables XIII to XVI show the preheats predicted by our programme.

5.4 Discussion

It is important to note that presently we are predicting the influence of preheat on the weld cooling cycle by introducing initial plate temperature (T_o) as preheating temperature. This, however, is not precise because, industrially, the preheat is often applied in such a way that the preheating is done only before welding, using gas flames and/or an electric heater over a width including the weld line, until the plate temperature is raised to the required value.

We have also not considered the effect of tempering in the case of the high preheat levels. At higher preheat levels, the cooling process is delayed in the range of 400°C to 100°C, long enough to produce tempering effects.

Apart from the limitations cited for the prediction procedures used in determining cooling rates, HAZ microstructure and preheat effects, we can conclude that our system of establishing safe welding procedures to avoid HAZ cold-cracking, on the basis of the lower critical implant

fracture stress (σ_{CR}), presents an accurate, systematic approach to HAZ cold-cracking control in actual welded joints.

The HAZ cold-cracking susceptibility is assessed in terms of:

1) HAZ microstructure,

2) HAZ hydrogen level,

3) HAZ stress level,

and for a given welding heat input, plate thickness, plate composition, hydrogen level and joint restraint level, preheat level, if necessary, to avoid cold-cracking, is recommended.

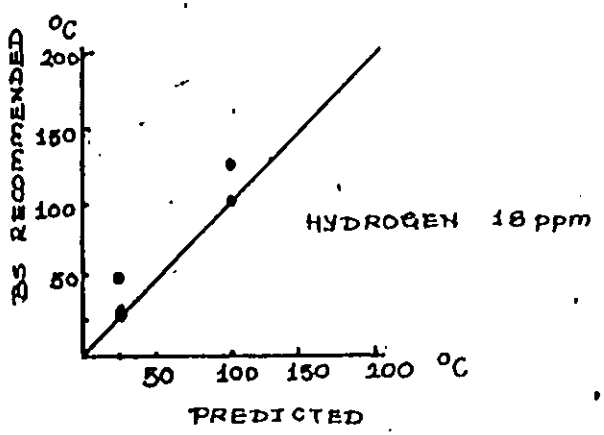

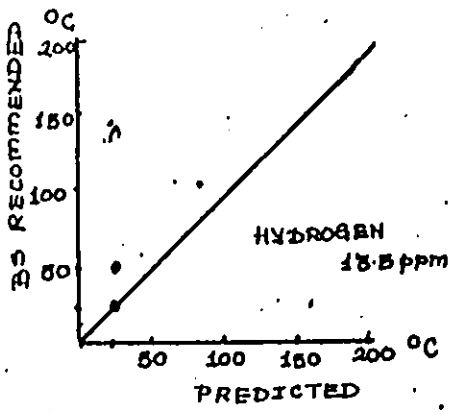

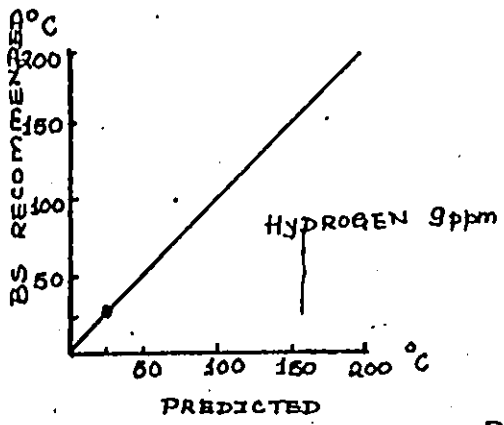

C Mn
0·20 1·2

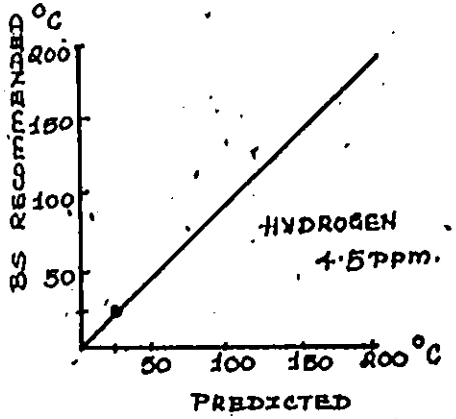

PLATE THICKNESS 26mm

Figure 37 Comparison Between Predicted Preheats and Recommended (BS standard) Preheats

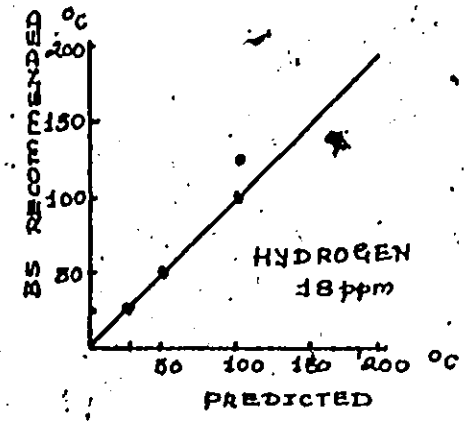

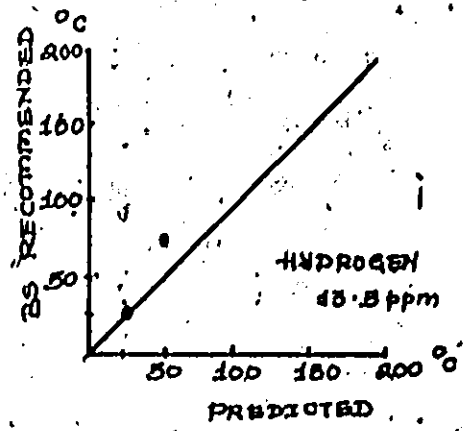

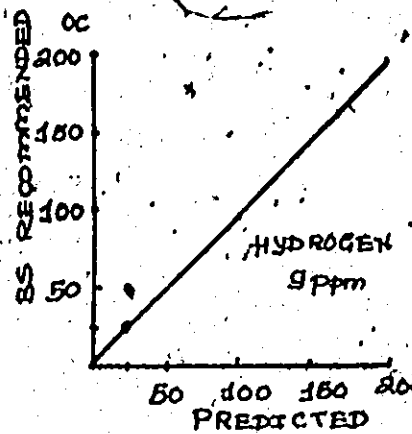

C Mn
0·21 1·2
PLATE THICKNESS 26 mm

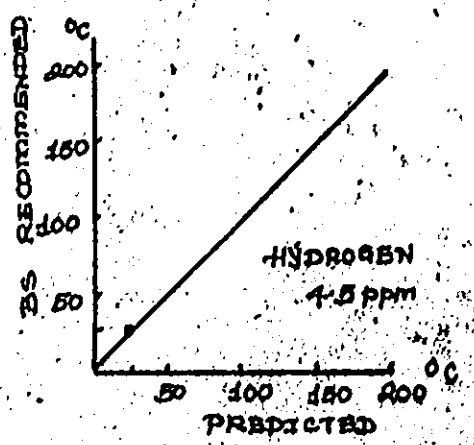

Figure 38 Comparison Between Predicted Preheats and Recommended (BS standard) Preheats

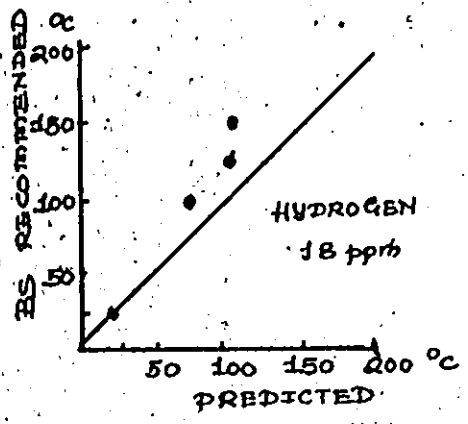

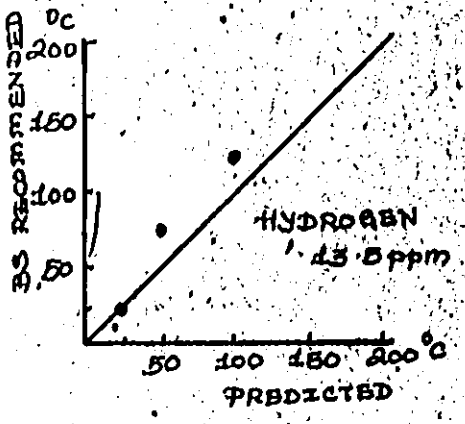

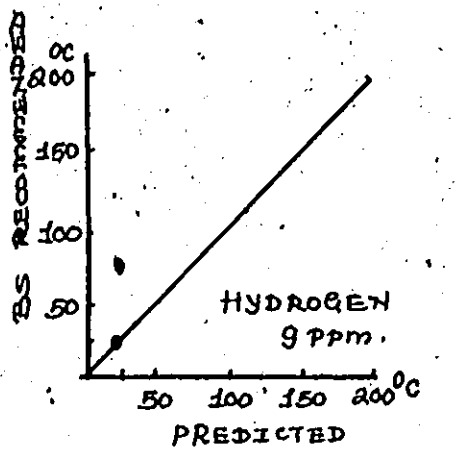

C Mn
0·23 1·2

PLATE THICKNESS 26mm

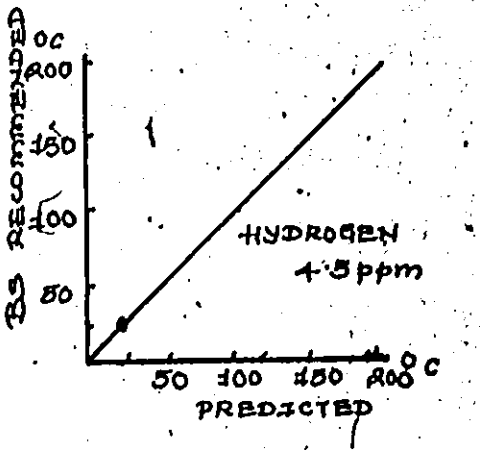

Figure 39 Comparison Between Predicted and Recommended (BS standard) Preheats

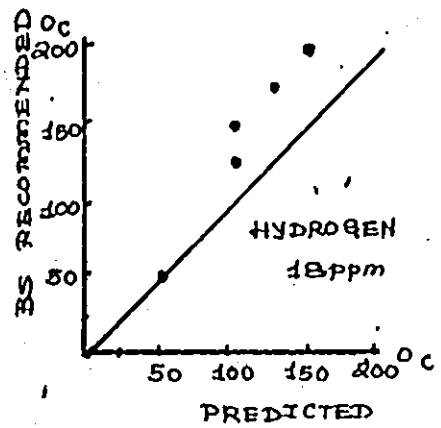

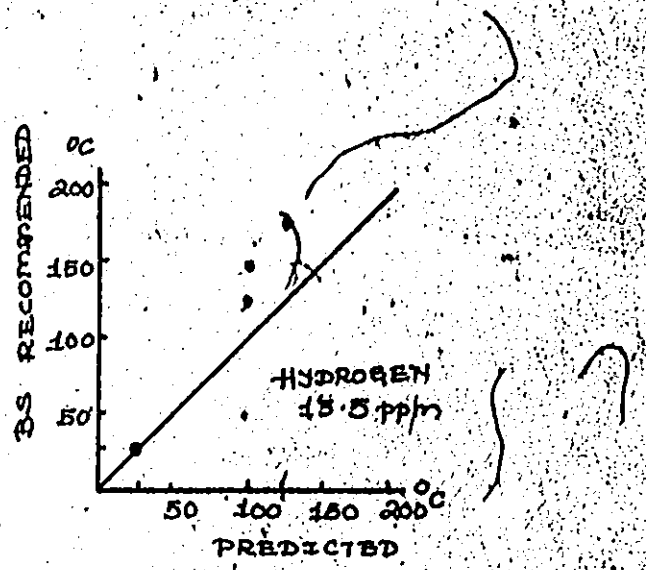

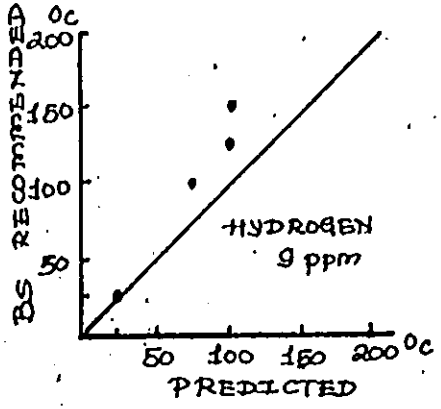

C Mn
0·29 1·2

PLATE THICKNESS 26mm

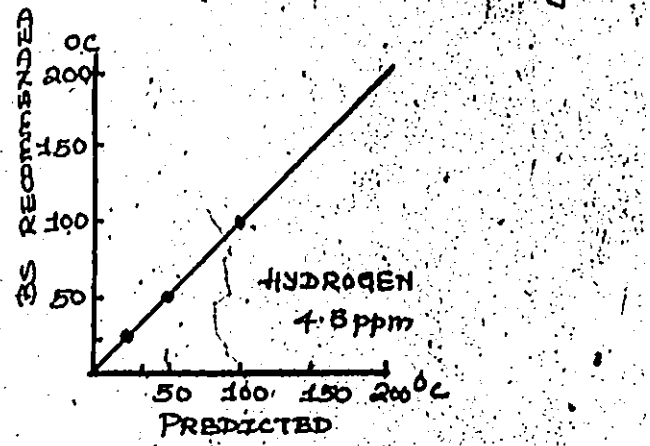

Figure 40 Comparison Between Predicted Preheats and Recommended (BS standard) preheats

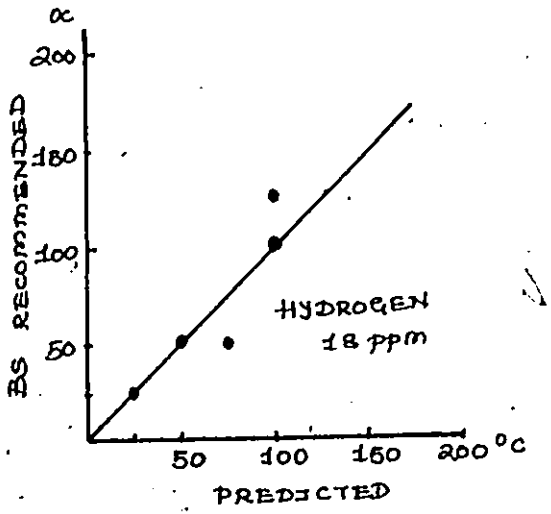

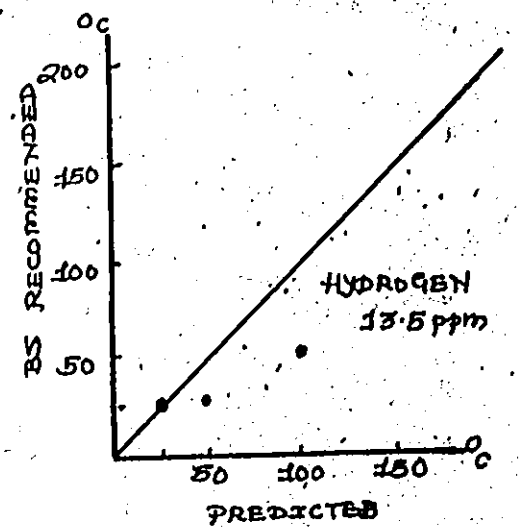

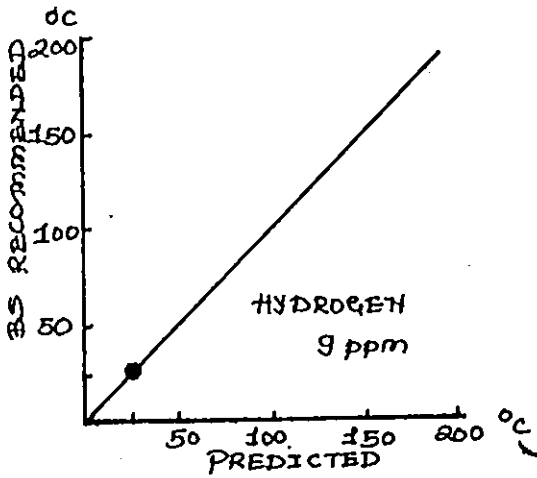

C Mn
0·20 1·2

PLATE THICKNESS 30 mm

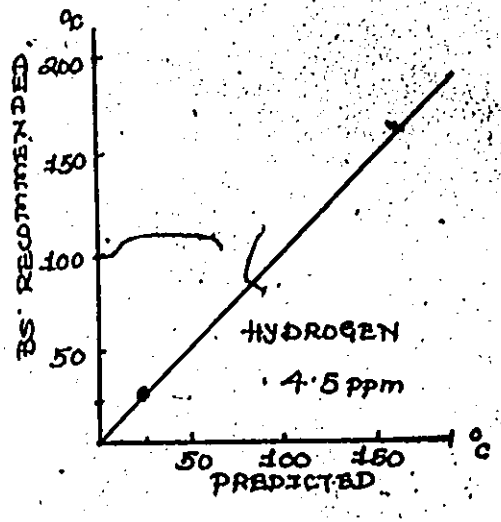

Figure 41 Comparison Between Predicted preheats and Recommended (BS Standard) Preheats

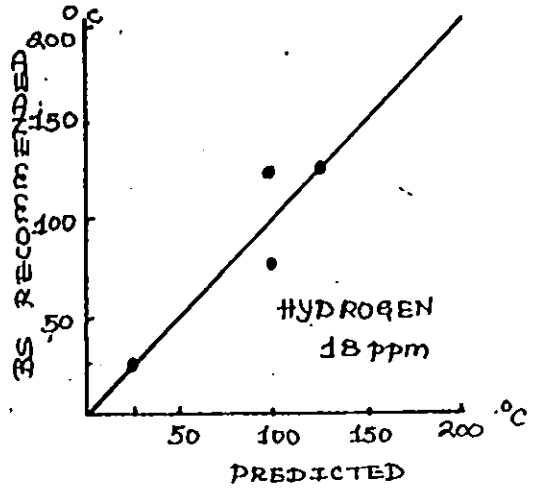

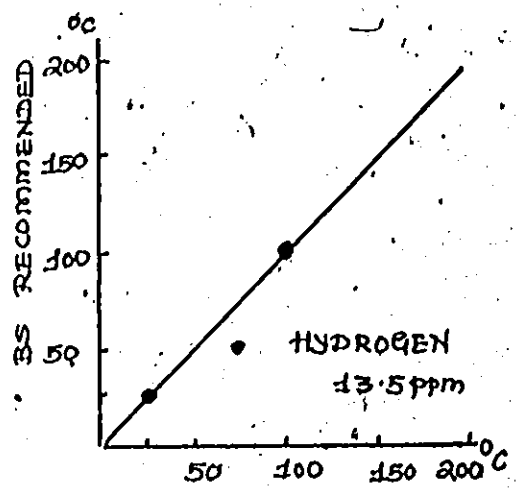

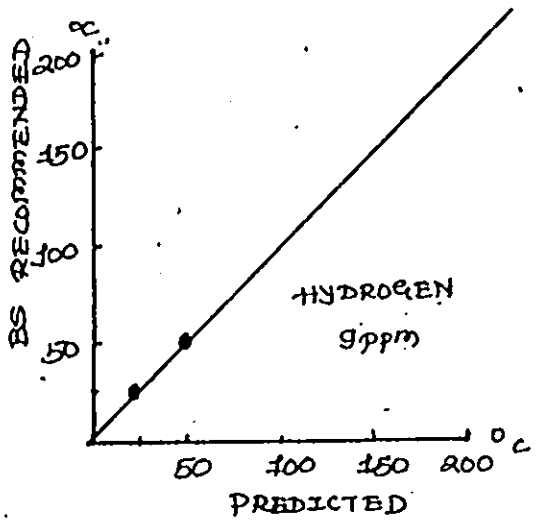

C 0·21 Mn 1·2

PLATE THICKNESS 30mm

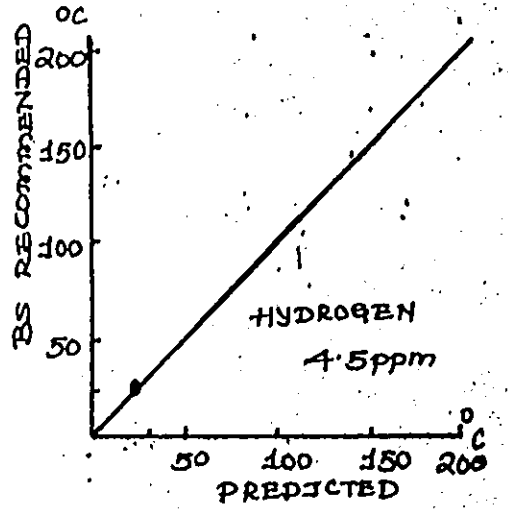

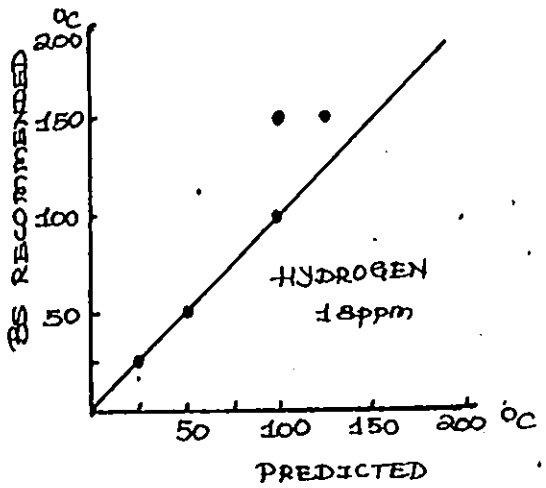

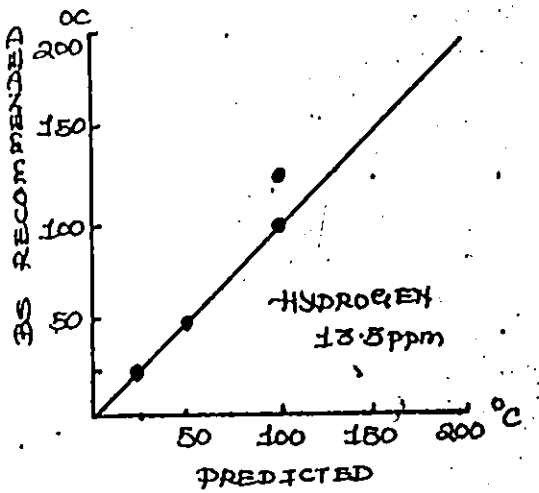

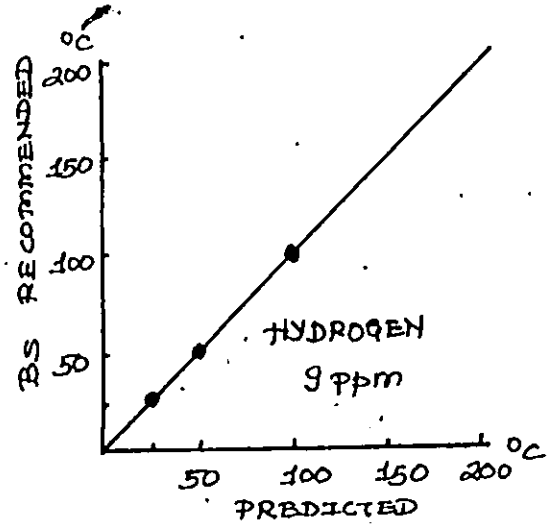

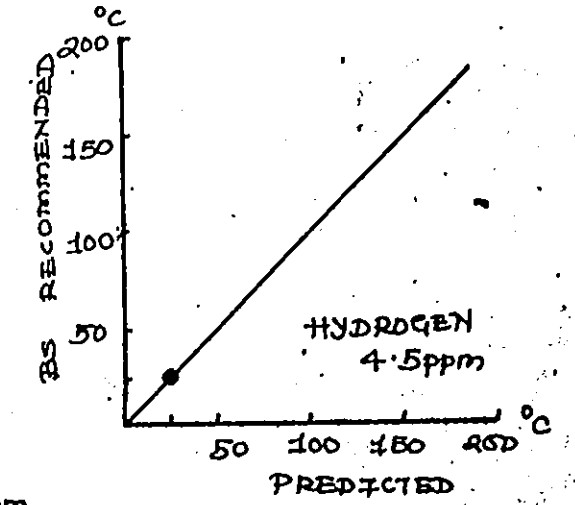

C Mn
0·23 1·2

PLATE THICKNESS 30mm

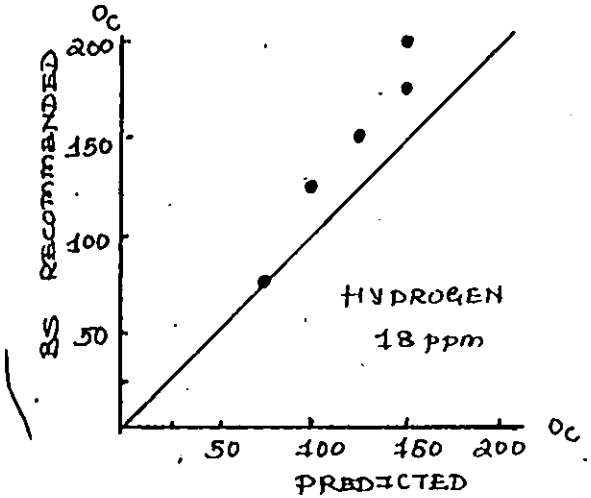

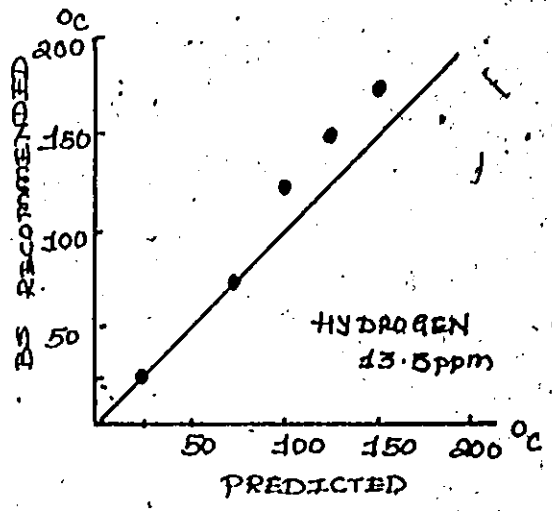

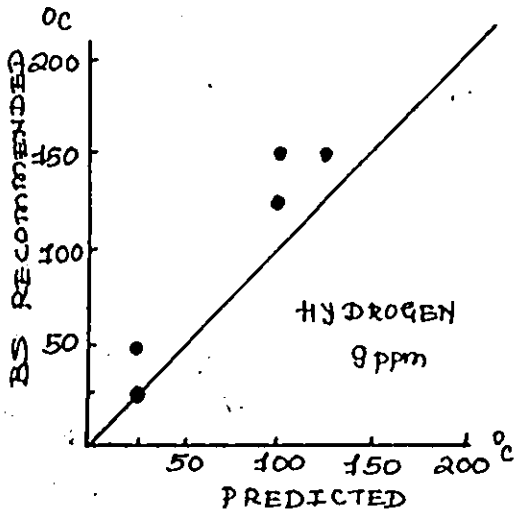

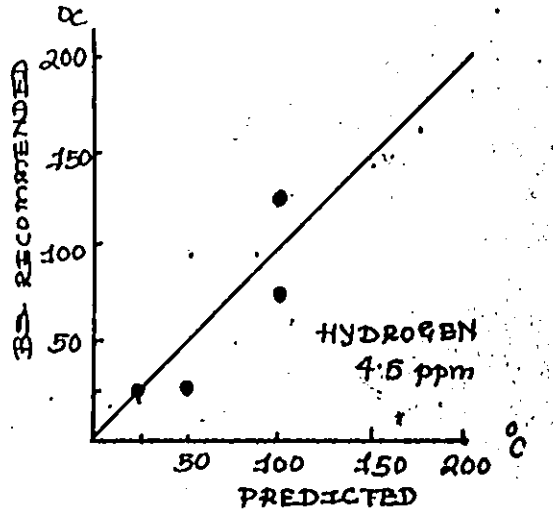

C Mn
% 0·29 1·2

PLATE THICKNESS 30mm

TABLE XIII

Preheat Levels Predicted for Various Steel Compositions, Plate Thickness, Heat Input, and Hydrogen Level with Fillet Weld Configuration

Heat Input KJ/mm	Hydrogen Level ppm	Preheating Temperature (OC) for following Thicknesses (mm)							
		7	10	13	16	20	23	26	30
0.9	13.5	0	0	0	0	0	0	50	100
1.1	13.5	0	0	0	0	0	0	0	75
1.5	13.5	0	0	0	0	0	0	0	0
2.3	13.5	0	0	0	0	0	0	0	0
3.3	13.5	0	0	0	0	0	0	0	0
0.7	18.0	0	0	0	0	0	50	100	100
0.9	18.0	0	0	0	0	0	50	100	100
1.3	18.0	0	0	0	0	0	0	50	100
1.9	18.0	0	0	0	0	0	0	0	0
2.5	18.0	0	0	0	0	0	0	0	0

C = 0.21 Mn = 1.2

Temperatures are quoted in 25^{0}C steps. " 0 " denotes a temperature less than 20^{0}C.

TABLE XIII

(continued)

Heat Input KJ/mm	Hydrogen Level ppm	Preheating Temperature (°C) for following Thicknesses (mm)							
		7	10	13	16	20	23	26	30
0.9	4.0	0	0	0	0	0	0	0	0
1.1	4.0	0	0	0	0	0	0	0	0
1.5	4.0	0	0	0	0	0	0	0	0
2.3	4.0	0	0	0	0	0	0	0	0
3.3	4.0	0	0	0	0	0	0	0	0
0.9	9.0	0	0	0	0	0	0	0	50
1.1	9.0	0	0	0	0	0	0	0	0
1.5	9.0	0	0	0	0	0	0	0	0
2.3	9.0	0	0	0	0	0	0	0	0
3.3	9.0	0	0	0	0	0	0	0	0

C = 0.21 Mn = 1.2

Temperatures are quoted in 25°C steps. " 0 " denotes a temperature less than 20°C.

TABLE XIV

Heat Input KJ/mm	Hydrogen Level ppm	Preheating Temperature (°C) for following Thicknesses (mm)							
		7	10	13	16	20	23	26	30
0.9	13.5	0	0	0	0	0	0	0	100
1.1	13.5	0	0	0	0	0	0	0	50
1.5	13.5	0	0	0	0	0	0	0	0
2.3	13.5	0	0	0	0	0	0	0	0
3.3	13.5	0	0	0	0	0	0	0	0
0.7	18.0	0	0	0	0	0	75	100	100
0.9	18.0	0	0	0	0	0	50	100	100
1.3	18.0	0	0	0	0	0	0	0	75
1.9	18.0	0	0	0	0	0	0	0	0
2.5	18.0	0	0	0	0	0	0	0	0

C = 0.20 Mn = 1.2

Temperatures are quoted in 25°C steps. " 0 " denotes a temperature less than 20°C.

Poor Copy

TABLE XIV

(continued)

Heat Input KJ/mm	Hydrogen Level ppm	Preheating Temperature (0C) for following Thicknesses (mm)							
		7	10	13	16	20	23	26	30
0.9	4.5	0	0	0	0	0	0	0	0
1.1	4.5	0	0	0	0	0	0	0	0
1.5	4.5	0	0	0	0	0	0	0	0
2.3	4.5	0	0	0	0	0	0	0	0
3.3	4.5	0	0	0	0	0	0	0	0
0.9	9.0	0	0	0	0	0	0	0	0
1.1	9.0	0	0	0	0	0	0	0	0
1.5	9.0	0	0	0	0	0	0	0	0
2.3	9.0	0	0	0	0	0	0	0	0
3.3	9.0	0	0	0	0	0	0	0	0

C = 0.20 Mn = 1.2

Temperatures are quoted in 25^{0}C steps. " 0 " denotes a temperature less than 20^{0}C.

TABLE XV

Heat Input KJ/mm	Hydrogen Level ppm	Preheating Temperature (°C) for following Thicknesses (mm)							
		7	10	13	16	20	23	26	30
0.9	4.0	0	0	0	0	0	0	0	0
1.1	4.0	0	0	0	0	0	0	0	0
1.5	4.0	0	0	0	0	0	0	0	0
2.3	4.0	0	0	0	0	0	0	0	0
3.3	4.0	0	0	0	0	0	0	0	0
0.9	9.0	0	0	0	0	0	0	0	100
1.1	9.0	0	0	0	0	0	0	0	50
1.5	9.0	0	0	0	0	0	0	0	0
2.3	9.0	0	0	0	0	0	0	0	0
3.3	9.0	0	0	0	0	0	0	0	0

C = 0.23 Mn 1.2

Temperatures are quoted in 25°C steps. " 0 " denotes a temperature less than 20°C.

Poor Copy

TABLE XV

(continued)

Heat Input KJ/mm	Hydrogen Level ppm	Preheating Temperature (°C) for following Thicknesses (mm)							
		7	10	13	16	20	23	26	30
0.9	13.5	0	0	0	0	0	50	100	100
1.1	13.5	0	0	0	0	0	0	50	100
1.5	13.5	0	0	0	0	0	0	0	50
2.3	13.5	0	0	0	0	0	0	0	0
3.3	13.5	0	0	0	0	0	0	0	0
0.7	18.0	0	0	0	0	75	100	100	125
0.9	18.0	0	0	0	0	50	100	100	100
1.3	18.0	0	0	0	0	0	0	75	100
1.9	18.0	0	0	0	0	0	0	0	50
2.5	18.0	0	0	0	0	0	0	0	0

C = 0.23 Mn = 1.2

Temperatures are quoted in 25°C steps. " 0 " denotes a temperature less than 25°C.

TABLE XVI

Heat Input KJ/mm	Hydrogen Level ppm	Preheating Temperature (°C) for following Thicknesses (mm)							
		7	10	13	16	20	23	26	30
0.9	4.0	0	0	0	0	0	50	100	100
1.1	4.0	0	0	0	0	0	0	50	100
1.5	4.0	0	0	0	0	0	0	0	50
2.3	4.0	0	0	0	0	0	0	0	0
3.3	4.0	0	0	0	0	0	0	0	0
0.9	9.0	0	0	0	0	75	100	100	125
1.1	9.0	0	0	0	0	0	75	100	100
1.5	9.0	0	0	0	0	0	0	75	100
2.3	9.0	0	0	0	0	0	0	0	0
3.3	9.0	0	0	0	0	0	0	0	0

C = 0.29 Mn = 1.2

Temperatures are quoted in 25°C steps. " 0 " denotes a temperature less than 20°C.

Poor Copy

TABLE XVI
(continued)

Heat Input KJ/mm	Hydrogen Level ppm	Preheating Temperature (°C) for following Thicknesses (mm).							
		7	10	13	16	20	23	26	30
0.9	13.5	0	0	0	0	100	100	125	150
1.1	13.5	0	0	0	0	75	100	100	125
1.5	13.5	0	0	0	0	0	75	100	100
2.3	13.5	0	0	0	0	0	0	0	75
3.3	13.5	0	0	0	0	0	0	0	0
0.7	18.0	0	0	0	100	100	125	150	150
0.9	18.0	0	0	0	75	100	100	125	150
1.3	18.0	0	0	0	0	75	100	100	125
1.9	18.0	0	0	0	0	0	50	100	100
2.5	18.0	0	0	0	0	0	0	50	100

Poor Copy

109

°C = 0.29 Mn = 1.2

Temperatures are quoted in 25°C steps. " 0 " denotes a temperature less than 20°C.

CHAPTER 6

DEVELOPMENT AND USE OF IMPLANT TESTING MACHINE

6.1 General Remarks

The ability of the implant test to offer a quantitative assessment of the cold-cracking susceptibility of the HAZ, in terms of the lower critical fracture stress (σ_{CR}), below which cracking would not occur for the given HAZ microstructural characteristics and hydrogen level, is very useful. The importance of the implant test data in determining cold-crack-free welding procedures is seen from the preceding chapters.

Considering the advantage of the implant test as a weldability test and the lack of extensive published implant test data, we undertook to develop an implant testing machine with an automatic welding and loading facility. Additional test data would be used to strengthen, improve and confirm correlations and predictions based on the test results.

6.2 Design of the Implant Testing Machine

As described in Chapter 2, a cylindrical specimen of the material under investigation, containing a circumferential notch at one end, is implanted in a base block and a weld is made over the end of the specimen (see Figure 4). The test further consists of constant load-rupture-testing of a series of implant specimens at decreasing loads, to establish the critical stress (σ_{CR}) below which rupture does not occur (see Figure 5).

The implant testing machine that we have developed consists of three major systems:

1) a system for automatic deposition of Manual Shielded Metal Arc Welding (MSMAW) electrodes,

2) the loading system,

and 3) the pressure system.

The design of these three systems is based on features of the implant testing machine at the British Welding Institute, U.K., as reported by Pedder and Hart.[47,48]

6.2.1 Automatic Deposition of MSMAW Electrodes

In considering the design of the equipment for the automatic deposition of MSMAW electrodes, the prime objective was to keep it simple and yet maintain adequate control of the welding from the moment when the arc was first established and adjusted to an appropriate arc length right through to the end of the test weld.

The design of the system is outlined in Figure 45. The drive system is powered by a d.c. motor, the speed of which is controlled by the supply voltage. The motor drives a lead screw through a reduction gear. The screw carries a saddle unit to which is attached the electrode holder. It was found possible to preset the speed of the motor so that the feed rate of the electrode was adequately matched to the burn-off rate of any setting of the welding current and the arc length.

Operation of the equipment is simple. Individual electrodes are held in the electrode holder which is moved vertically at a predetermined constant velocity, while the test piece being welded is moved horizontally under the welding head by means of a constant speed tractor.

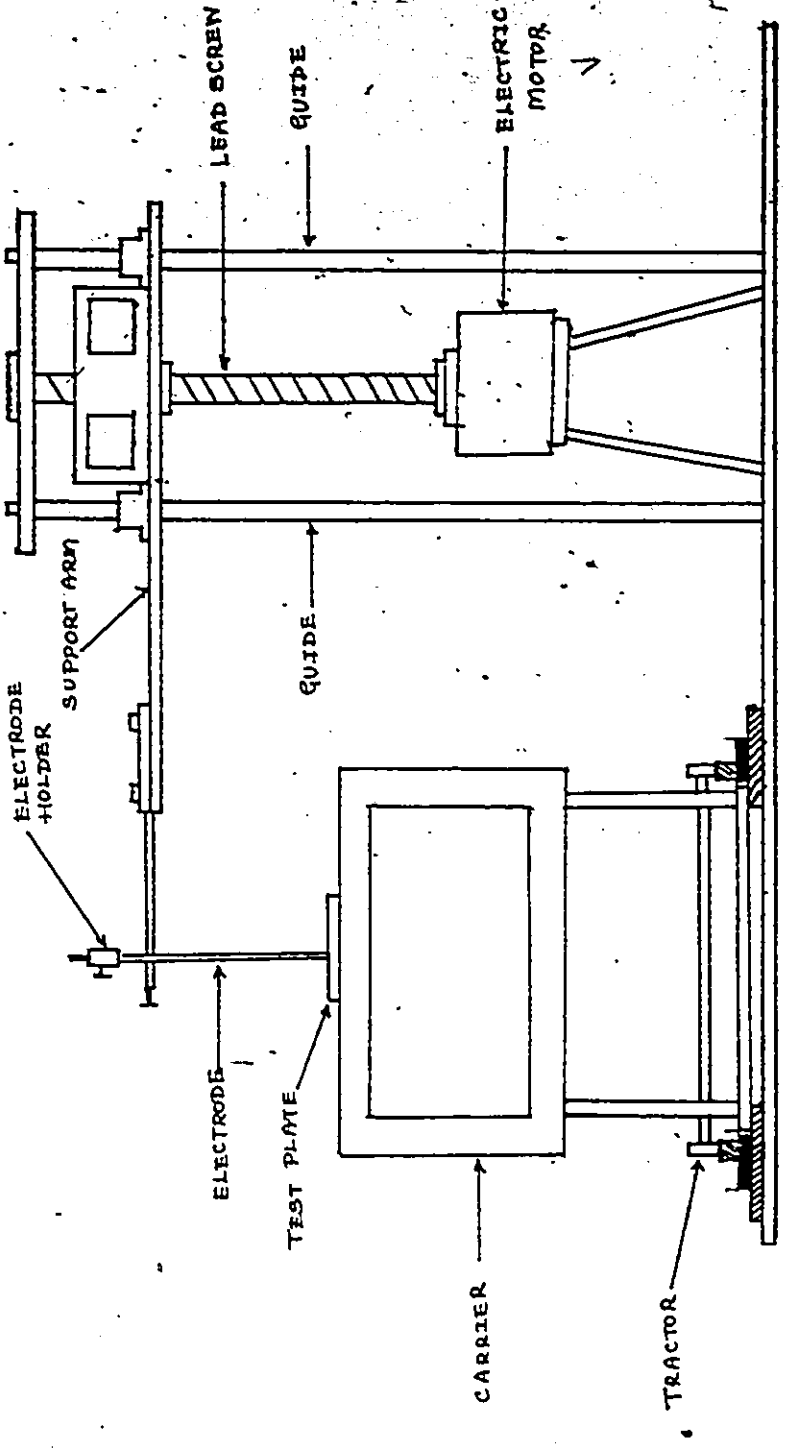

Figure 45 System for Automatic Deposition of MSMAW Electrodes

6.2.2 The Implant Loading System

The essential features of the loading system are shown in Figure 46. The load is applied through a pneumohydraulically operated lever system. The loading bar is positioned along the lever to give a lever ratio of 2:1, and this is attached to the implant specimen by a collect. Resistance gauges on the loading bar measure the actual load on the specimen. The stress at the implant notch section can be measured to an accuracy of 15 N/mm^2. The interval between the application of the load and complete rupture of the implant specimen is timed automatically.

The base block in which the implant specimen is welded is supported by rollers to allow a degree of self-alignment between the loading system and the implant specimen.

6.2.3 The Pressure System for the Implant Test

Pressure from a standard nitrogen gas cylinder is applied to an oil reservoir via a pressure regulator and a three-way solenoid valve, (see Figure 47). Before commencment of loading, the necessary gas pressure to give the required tensile load is set on the pressure gauge. When the pressure system is switched on, the solenoid valve opens. The gas pressure transfers to the oil cylinder through the flexible pressure hose and oil pressure activates the ram. The loading commences immediately after the solenoid is operated, and full load is achieved in about 2 seconds. The gas line is also equipped with a needle valve to allow any desired rate of loading to be used. The load applied to the notched section of the implant specimen can be adjusted if required, by manual adjustment of gas pressure. At the moment of failure of the implant

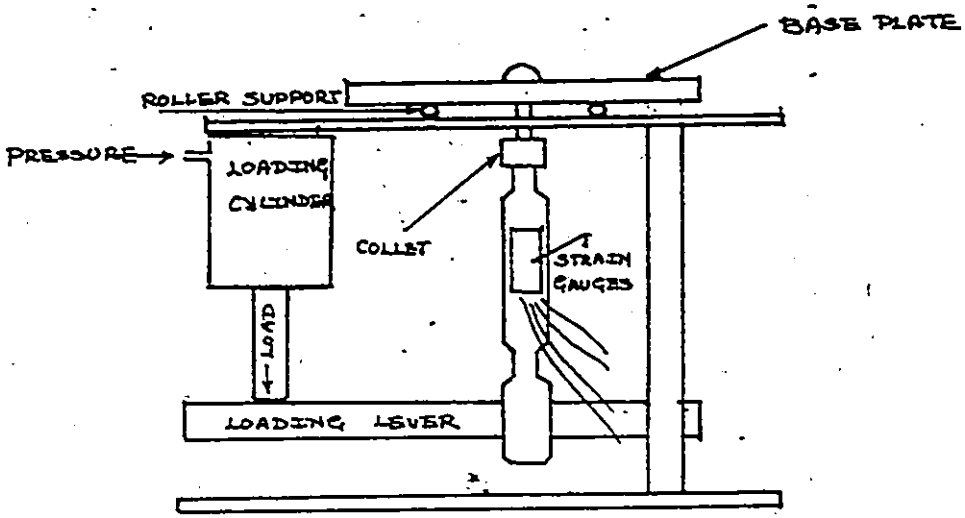

Figure 46 Implant Loading System

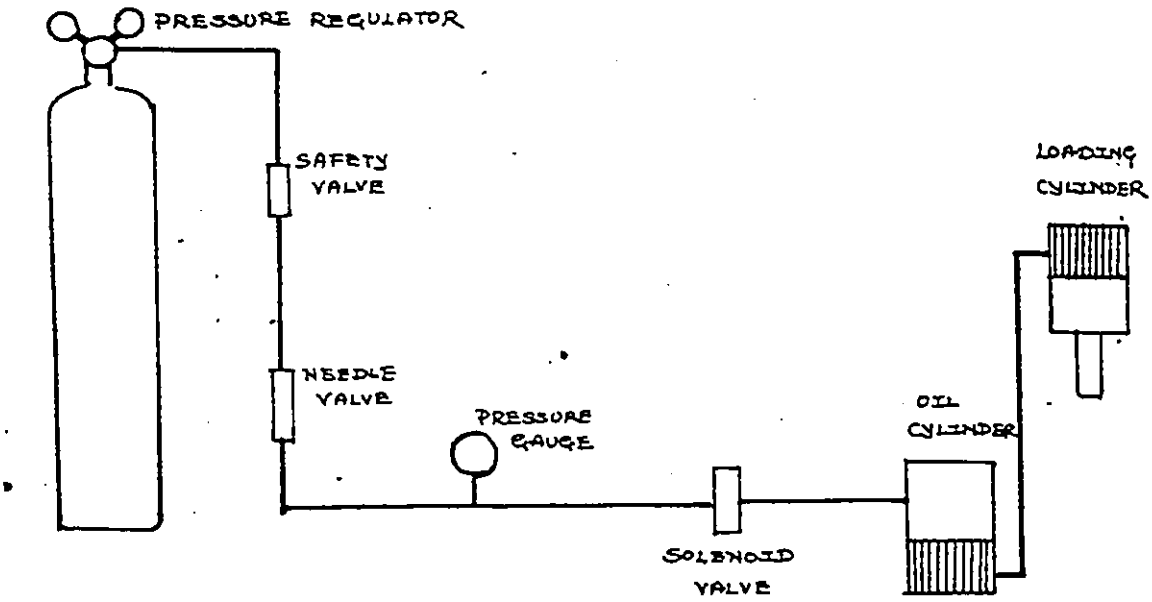

Figure 47 Pressure System for Implant Test

specimen, the timer stops and the gas solenoid valve closes.

Figure 48 shows the general view of the implant testing machine. Figure 49 gives the details of the arrangements for welding, and Figure 50 illustrates the loading system.

6.3 Standardization of the Implant Testing Procedure

The welding heat input, weld fusion zone shape, the location of the notch on the implant specimen relative to the fusion line, potential hydrogen level from the electrodes, and the notch geometry, affect the lower critical implant stress (σ_{CR}) considerably. Hence, the need for careful control and standardization of the testing procedure.

6.3.1 Welding Conditions

Three levels of heat inputs - 0.6, 0.9 and 1.2 kJ/mm, were selected for standardization. The welding speed was set constant and the heat input was altered through welding amperage selection. Several welds were made to determine the proper feed rate for the electrodes at each heat input level. During each weld, the arc voltage was controlled to ±1 volts and arc amperage to ±5 amperes.

After the weld was complete, the plate was sectioned to observe the shape and size of the fused zone to determine the location of the notch on the implant specimen for each heat-input level.

After a series of experiments, welding parameters, as shown in Table XVII, were selected. The Table also gives the bead size and the location of the notch from the end of the specimen for each heat-input level.

Figure 51 shows the sections of the weld bead for the three heat-

TABLE XVII

Welding Heat Input Details

Heat Input kJ/mm	Current amps.	Voltage volts	Welding Speed mm/sec.	Electrode inch (type)	Notch Distance mm
0.6	80	21	3	3/32" (7018)	0.90
0.9	130	20	3	1/8" (7018)	1.45
1.2	175	20	3	5/8" (7018)	2.00

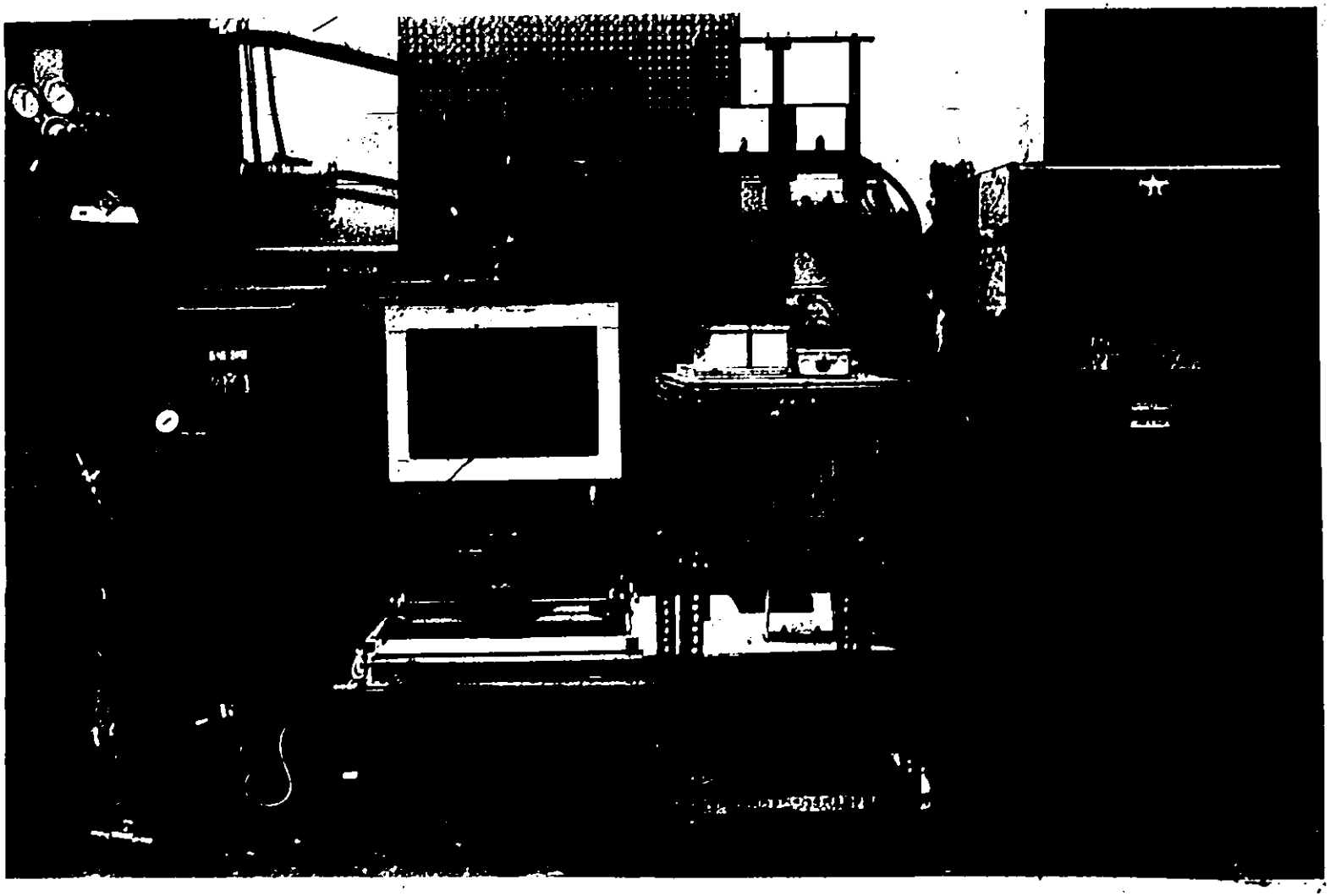

Figure 48 General View of the Implant Testing Equipment Complete with Automatic Welding and Loading Facility

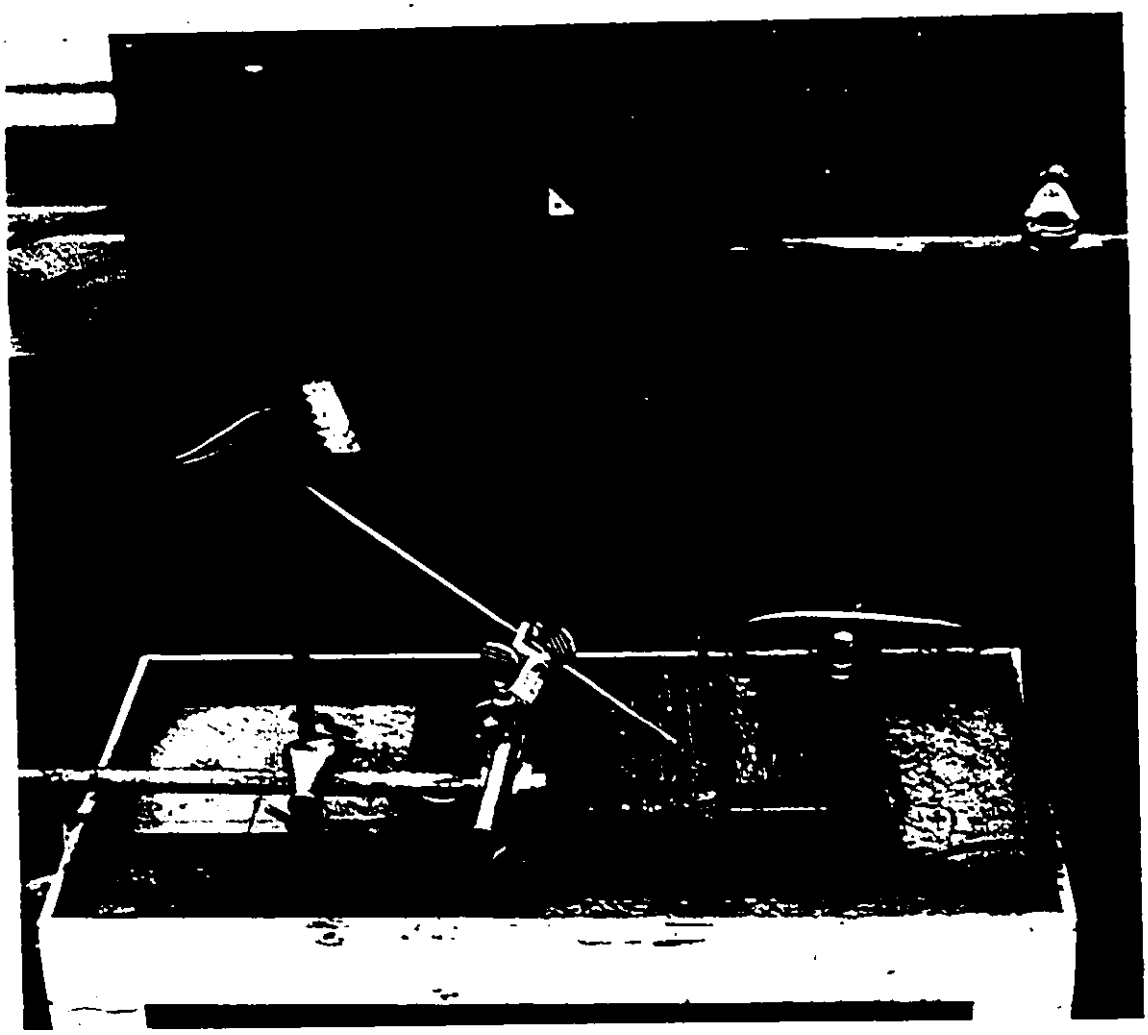

Figure 49 Details of the Welding Arrangement

Figure 50 Detailed View of The Loading System

input levels. Thermal cycles were also measured with Pt-Pt-10Rh Thermocouple placed next to the weld bead. Figure 52 shows a typical thermal cycle profile for 0.6 kJ/mm. Cooling time between 800°C and 500°C was calculated from the thermal cycle for each heat-input. Table XVIII compares the observed cooling times and the predicted cooling time at an arc-efficiency of 0.85.

Moisture level in the electrode coatings was controlled by storing them in an oven at 90°C.

6.3.2 Implant Test Details

In order to facilitate comparison with the draft recommendation prepared by sub-commission IXB of IIW, the description is itemized below:

1) Geometry of the Implant (see Figure 53)

Diameter of the implant: 5.6 mm

Notch: 40° vee, 0.5 mm deep, γ = 0.1 mm

Notch distance: dependent on heat input (see Table XVII)

2) Sampling Procedure

Specimens oriented with their axes in the direction of rolling.

Specimens machined from mid-plate thickness.

Ten specimens for each combination of steel hydrogen level and cooling programme.

3) Details of the Base Plate (see Figure 54)

Steel grade - C-Mn steel

Thickness: 30 mm

Dimensions: 250 mm by 175 mm

Five holes in each plate.

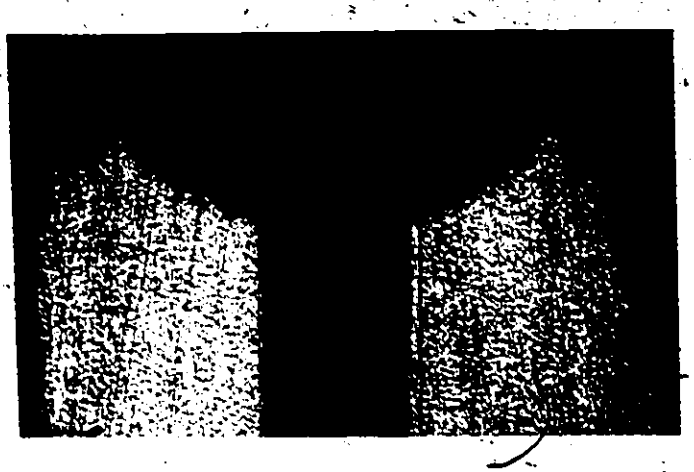

1.2 kJ/mm

0.9 kJ/mm

0.6 kJ/mm

Figure 51 Weld Bead Sections for Three Heat Inputs

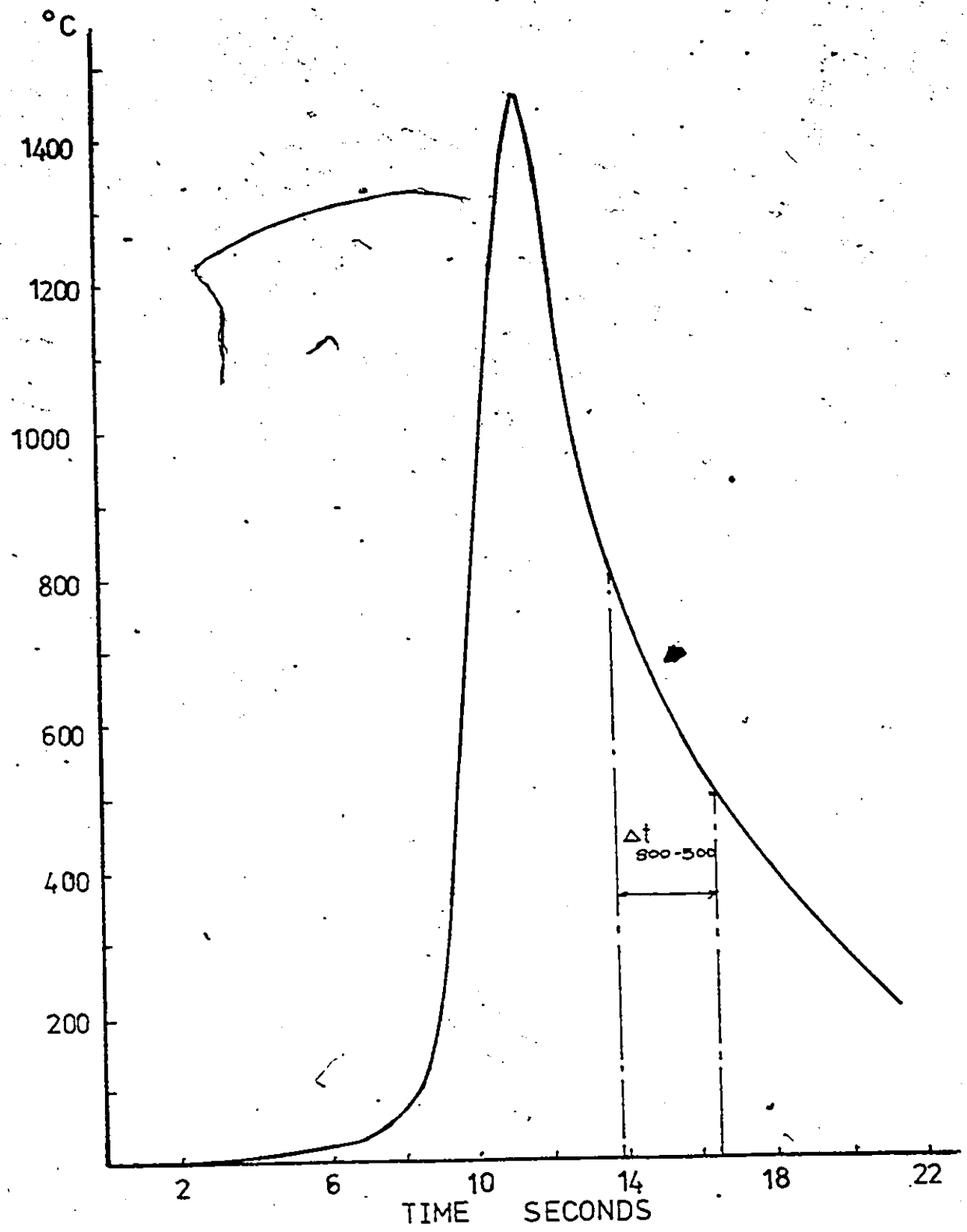

Figure 52 Typical Thermal Cycle Profile in Welding

TABLE VXIII

Comparison Between Observed and Predicted Cooling Times Between 800°C - 500°C

Heat Input	Predicted Cooling Time (sec.)	Observed Cooling Time (sec.)	Predicted Log (cooling rate) °C/hr	Observed Log (cooling rate) °C/hr
0.6	2.4	2.6	5.66	5.61
0.9	3.5	3.8	5.49	5.46
1.2	4.7	4.9	5.36	5.34

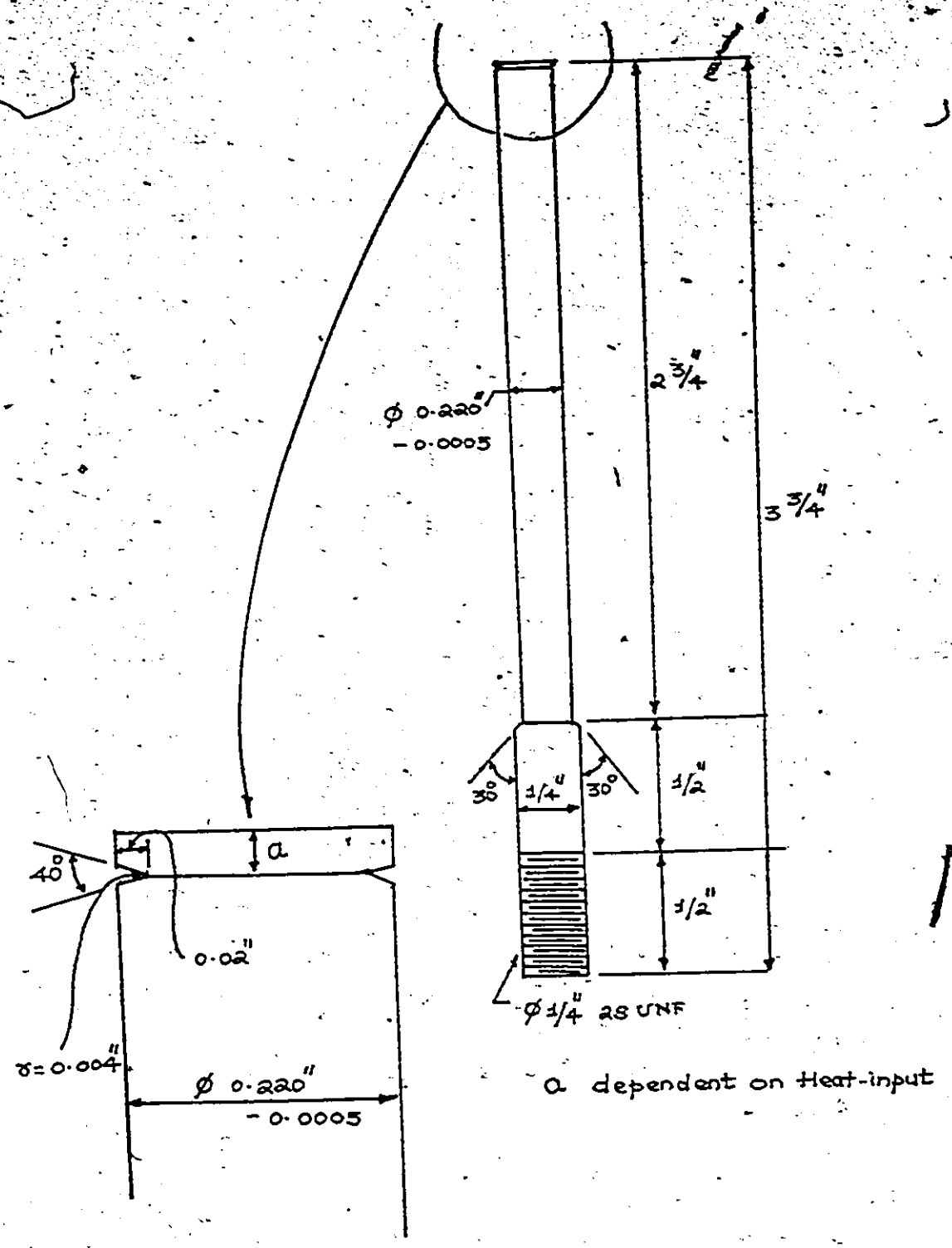

Figure 53 Implant Specimen Details

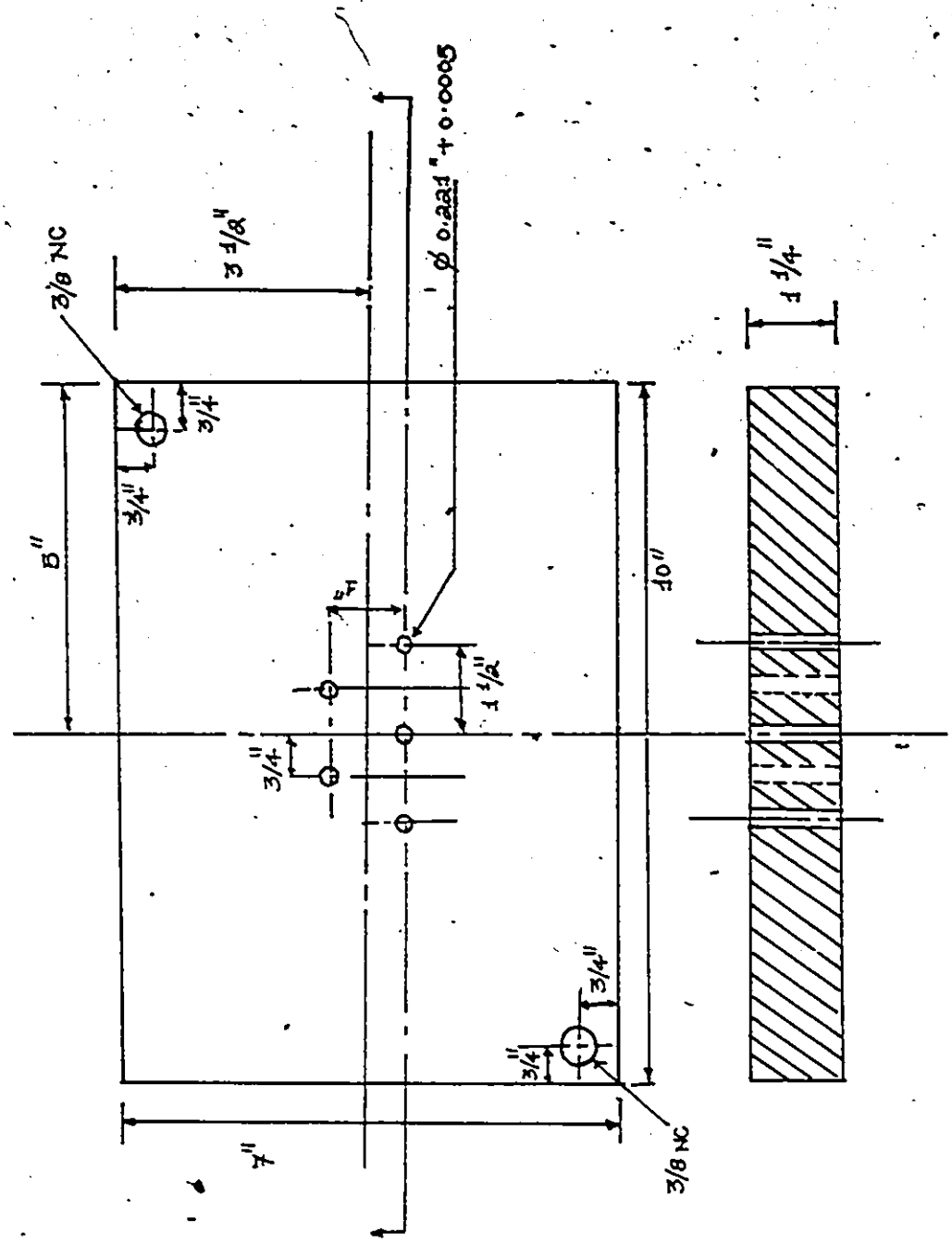

Figure 54 Base Plate Used for Implant Test

The step-by-step procedure to be used for the implant testing machine is given in Appendix III.

The specimens which do not fracture can be sectioned (Figure 55) for hardness measurements and microstructural features. Figure 56 shows the typical variation of hardness across the weld section. Maximum hardness in the coarse grained region of the HAZ (50 to 100 μm from the fusion line) is taken as the characteristic HAZ hardness.

6.4 Preliminary Tests

Preliminary experiments for evaluating the performance of the machine were carried out on two steels under the same welding conditions. The specimens were made to the specifications in Section 6.3.2. The chemical composition of the steels is given in Table XIX. The specimens were austenitised at 890°C for 1 hr and tempered at 400°C for 1 hr. The implant testing was done according to the procedure given in the Appendix at the heat-input level of 0.6 kJ/mm with low hydrogen 7018 electrodes. Figures 57 and 58 are the stress-fracture time diagrams for the two steels. Steel No. 1 was characterized by σ_{CR} of 471 N/mm^2, and Steel No. 2 was characterized by σ_{CR} of 429 N/mm^2.

6.5 Discussion

It is seen from the σ_{CR} values for the two steels that the implant test developed by us is able to distinguish the two steels under the same welding condition.

Steel No. 2, because of its higher carbon and manganese content, is indeed expected to have a lower σ_{CR} than for Steel No. 1. In principle,

Figure 55 Section of Implant Specimen Showing the Location of the Notch

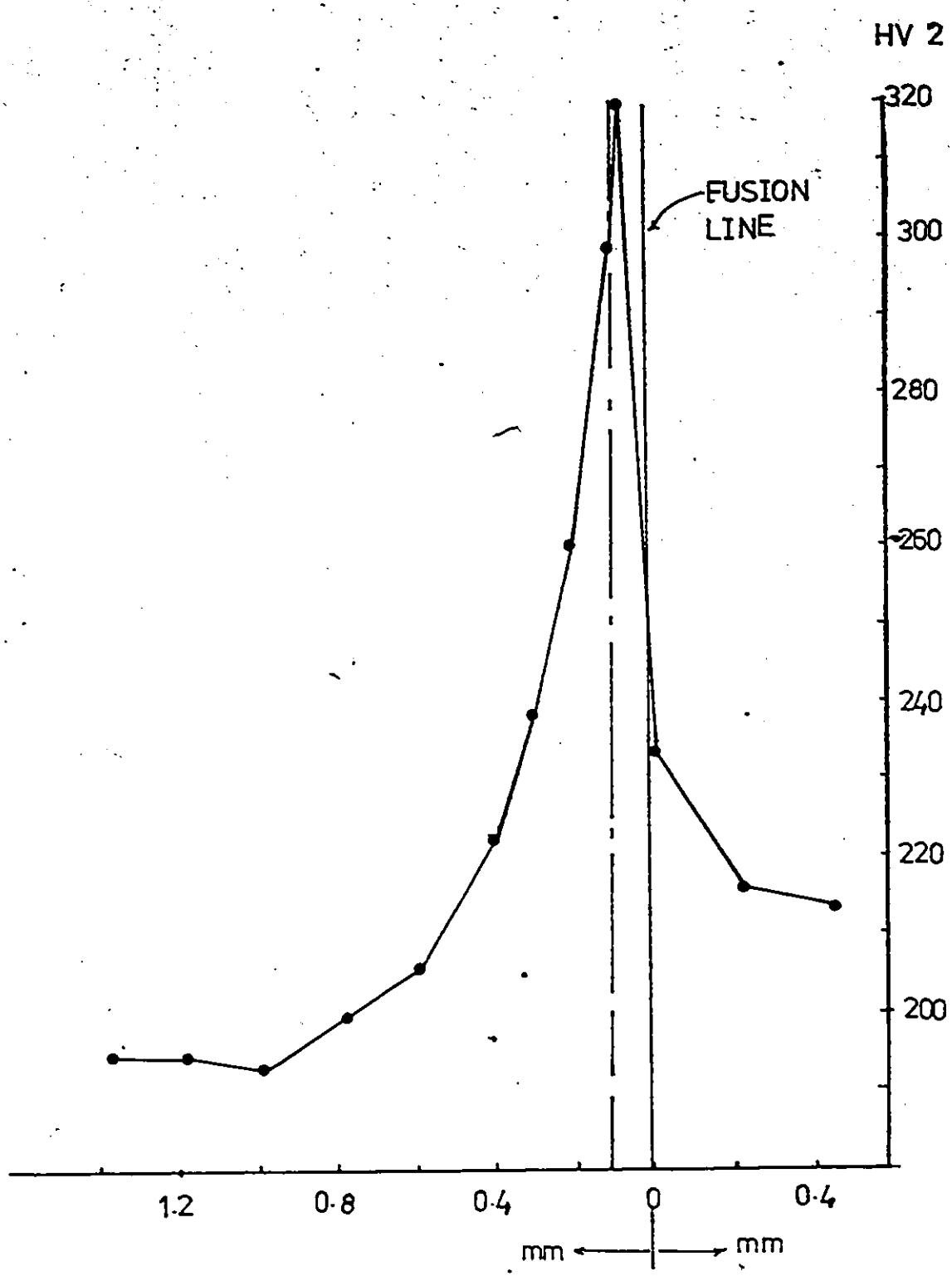

Figure 56 · Typical Variation of Hardness Across the Weld

TABLE XIX

Chemical Compositions of the Steels Used for Implant Testing

Steel	C	Mn	Si	P	S
1	0.185	0.31	0.02	0.010	0.028
2	0.223	0.49	0.07	0.006	0.037

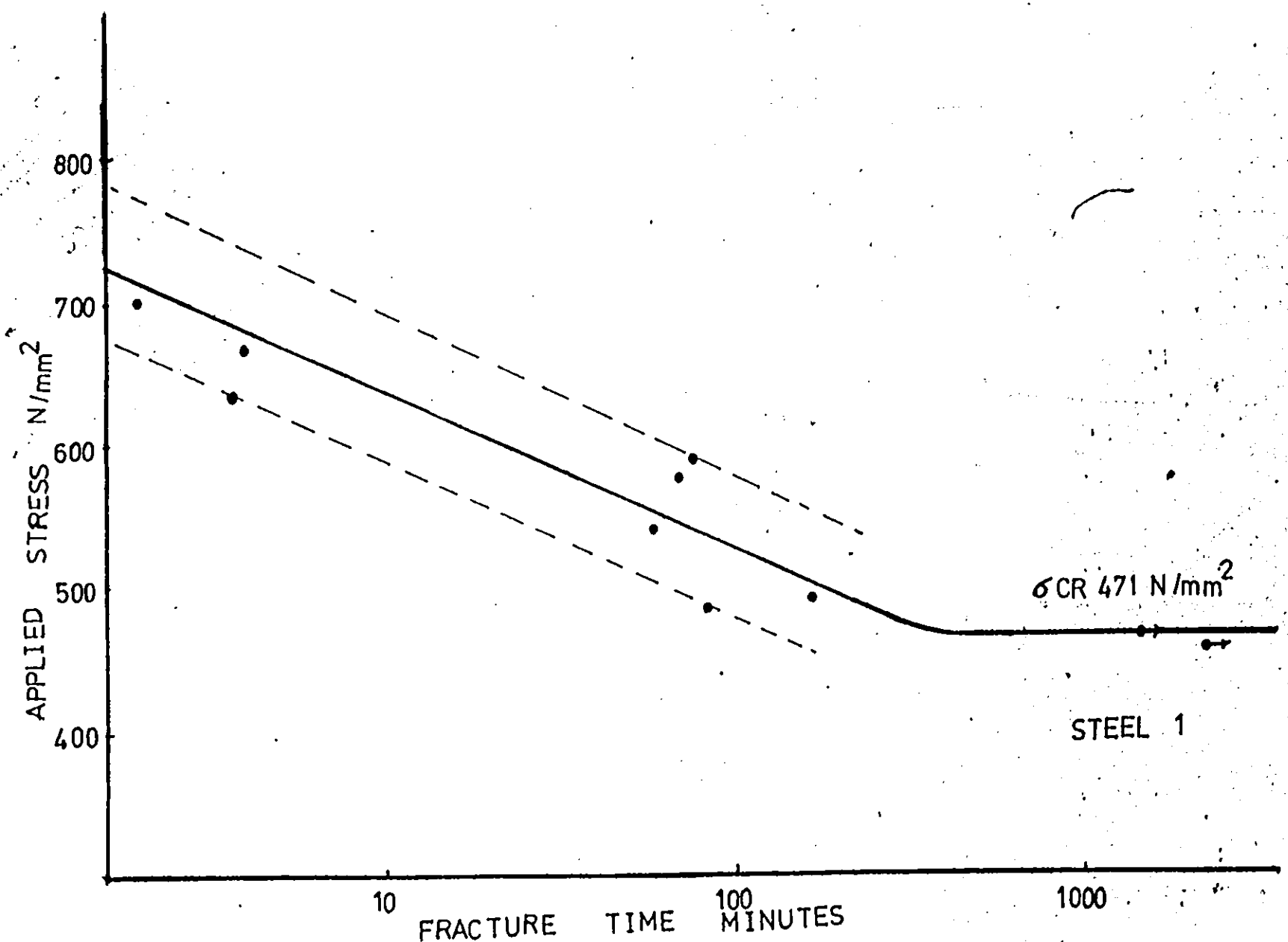

Figure 57 Stress-Fracture Time Diagram for Steel No. 1

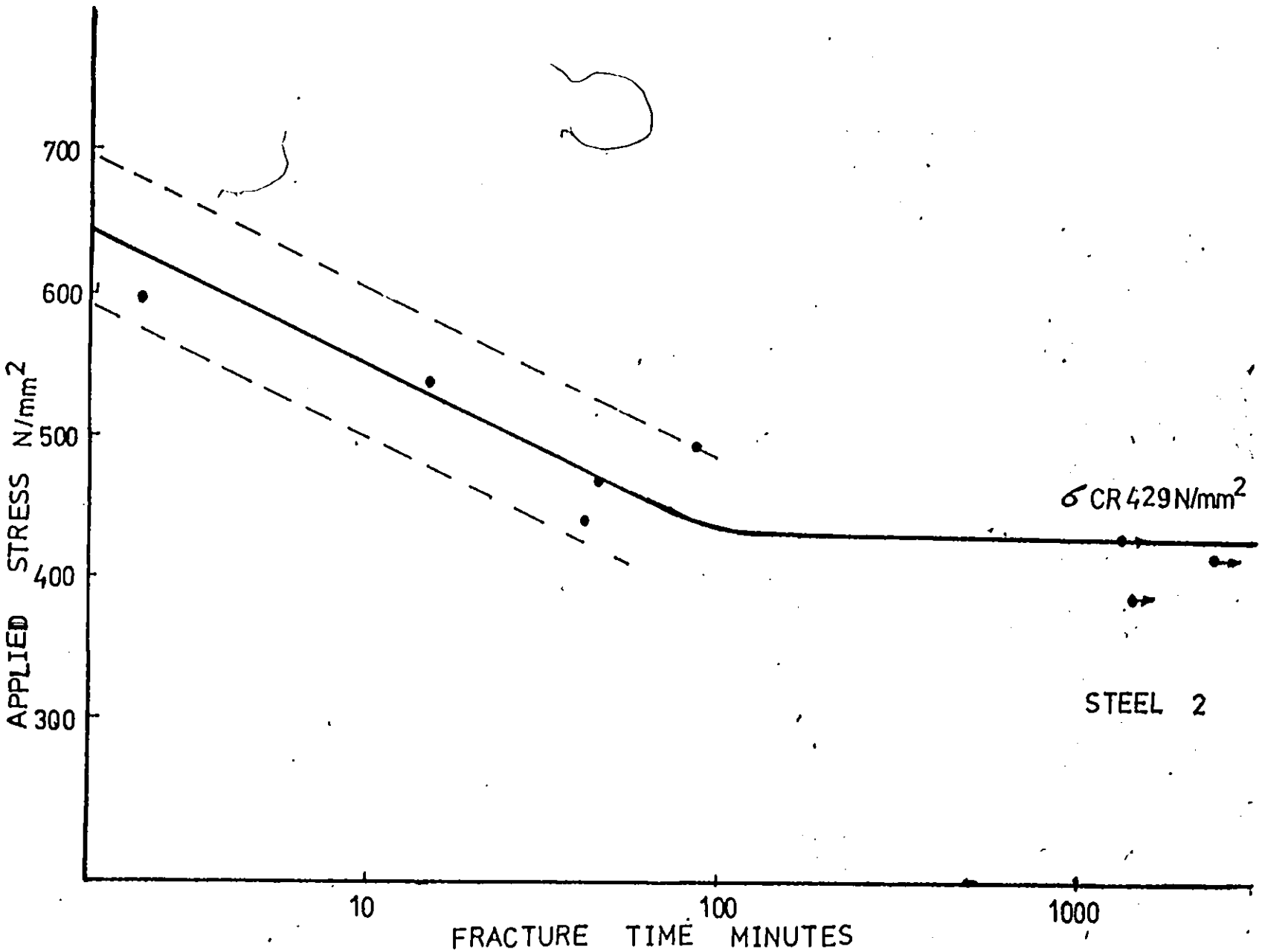

Figure 58 Stress-Fracture Time Diagram for Steel No. 2

we should be able to predict the difference in σ_{CR} for the two steels on the basis of prediction of HAZ % martensite and HAZ hardness. However, we are not yet in a position to compare the observed σ_{CR} with that predicted, since for the steels that we are using, for a heat input of 0.6 kJ/mm, HAZ % martensite is predicted to be less than 50%, which is our present prediction limit. The correlation formula also cannot be used with the observed % martensite and hardness as inputs, since the technique of quantitative estimation of the HAZ % martensite is yet to be developed. Comparison between predicted and observed σ_{CR} can be made in future by carrying out tests on higher carbon equivalent steels.

Another aspect to be noted for tests at 0.6 kJ/mm is that for this heat-input, the width of the weld bead approaches the diameter of the specimen. Under these circumstances, unless a very flat weld penetration profile can be obtained, all the circumference of the notch cannot be situated in the high temperature HAZ. Slight misalignment of the weld further aggravates this situation. In fact, at the side of the specimen, the notch is more likely to be situated in the lower temperature HAZ. Thus, it was seen in some cases that the fracture did not follow the notch around the whole circumference but preferred to propagate through coarse grained HAZ and ignored the notch on the side of the specimen. This type of fracture was associated with increased times to failure.

CHAPTER 7

CONCLUSIONS

1. On the basis of published implant test data, a correlation formula is developed to predict the influence of HAZ microstructure and hydrogen level on lower critical implant fracture stress (σ_{CR}) with % martensite, HAZ hardness and hydrogen levels as parameters.

2. Calculation of the stress intensity and hydrogen concentration in the region of maximum triaxiality in front of the notch on the implant specimen at σ_{CR}, shows that for a given microstructure, the hydrogen concentration attained in the critical region decreases with increasing stress intensity, and vice versa. This is opposed to the thesis that a fixed concentration of hydrogen, depending only on microstructure and not on stress level, has to be attained before cracking can occur.

3. Analysis of heat transfer during welding is used, together with % martensite - composition - cooling rate relations and hardness-composition - cooling rate relations to predict % martensite and HAZ hardness for given plate thickness, heat input and preheat level.

4. The predicted HAZ hardness and % martensite are in good agreement with observed hardness and % martensite for various welding conditions and plate compositions. Prediction of % martensite and hardness in the HAZ is employed together with the

correlation formula to predict σ_{CR}. It is shown that the predicted σ_{CR} effectively serves as a parameter for relating observed weld cracking % for various low alloy steel compositions.

5. With the criterion that the reaction stress developed in the weld should be less than σ_{CR} under the same welding conditions, to prevent cracking, an algorithm with hydrogen diffusion calculations is developed to predict preheat levels necessary to prevent cracking for given plate composition, joint design and restraint, heat input and initial hydrogen level without preheat.

6. Predicted preheats are compared with recommended (British Welding Standards) preheats for fillet welds showing the conservative nature of those standards.

7. An Implant Testing Machine with an automatic welding and loading facility has been developed and the testing procedure is outlined. Preliminary tests were made on two steels for the same welding conditions to assess the performance of the machine.

APPENDIX-I

STRESS INDUCED DIFFUSION OF HYDROGEN

The hydrogen concentration (H_{CR}) attained in the region of maximum triaxiality in front of the notch on the implant specimen is given by Urednicek[36] as follows:

$$\ln\left(\frac{H_{CR}}{H_I}\right) = \frac{V_H \alpha''(\delta y)_I}{RT}\left[\ln\left[(k_{TH})\frac{\alpha'}{\rho_o E} + 1\right] + \frac{1}{2}\right] \qquad (20)$$

To calculate (k_{TH}) from Implant Test Lower Critical fracture stress (σ_{CR}) we have, again from Urednicek's analysis:

$$(k_{TH}) = 0.259 \times (\sigma_N) \times (\pi DI)^{1/2} \qquad (67)$$

where DI is the diameter of the implant specimen, σ_N is the implant fracture stress calculated for the net cross section given by:

$$D_{Net} = \text{Net Cross Section DIA} = DN - 2 \times R_B \qquad (68)$$

where DN is the implant specimen diameter at the notch tip section, and R_B is the distance in front of the notch at which triaxiality is maximum.

For the implant test;

$$DN = 0.180"$$

$$DI = 0.220"$$

$$R_B = 1.52 \times 10^{-2}" \quad \text{(after Urednicek)}$$

Hence, $D_{Net} = 1.8 \times 10^{-1} - 2 \times 1.52 \times 10^{-2}$

$$= 14.96 \times 10^{-2} \qquad (69)$$

Also,

$$\sigma_N = \sigma_{CR} \times \frac{\pi}{4} \times DN^2 \times \frac{4}{\pi \times D_{Net}^2}$$

$$= \sigma_{CR} \times \frac{(0.180)^2}{(0.149)^2}$$

$$= 1.44 \times \sigma_{CR} \text{ KSI} \qquad (70)$$

Substituting the results in Equation (67), we have:

$$(k_{TH}) = 0.259 \times (1.44 \times \sigma_{CR}) \times (\pi \times 0.220)^{1/2}$$

$$= 0.31 \times \sigma_{CR} \text{ KSI}$$

$$= 0.31 \times 0.14 \ (\sigma_{CR}) \text{ N/mm}^2 \qquad (71)$$

Also,

$$\frac{\alpha'}{\rho_o E} = \frac{3}{13.01 \times 10^4 \times 29 \times 10^3}$$

$$= 0.07436 \ \frac{1}{\text{KSI}\sqrt{\text{INCH}}} \qquad (72)$$

$$\frac{RT}{V_H} = 1.22 \times 10^3 \text{ MPa} \quad \text{and} \quad \alpha'' = 2.$$

Hence,

$$\frac{V_H \alpha''}{RT} = \frac{2^{\alpha}}{1.22 \times 10^3} = 1.6393 \times 10^{-3} \frac{\text{mm}^2}{\text{Newtons}} \qquad (73)$$

Substituting Equations (67) to (73) into Equation (20), we have:

$$\ln \left(\frac{H_{CR}}{H_I}\right) = 1.6393 \times 10^{-3} (\sigma_y)_{N/mm^2} \left\{ \ln \left[3.23 \times 10^{-3} (\sigma_{CR})_{N/mm^2} + 1 \right] + \frac{1}{2} \right\}$$

APPENDIX II

Here, we present the flow chart for our programme to determine safe welding procedures on the basis of heat input, plate thickness, plate composition, joint design and restraint, and hydrogen level.

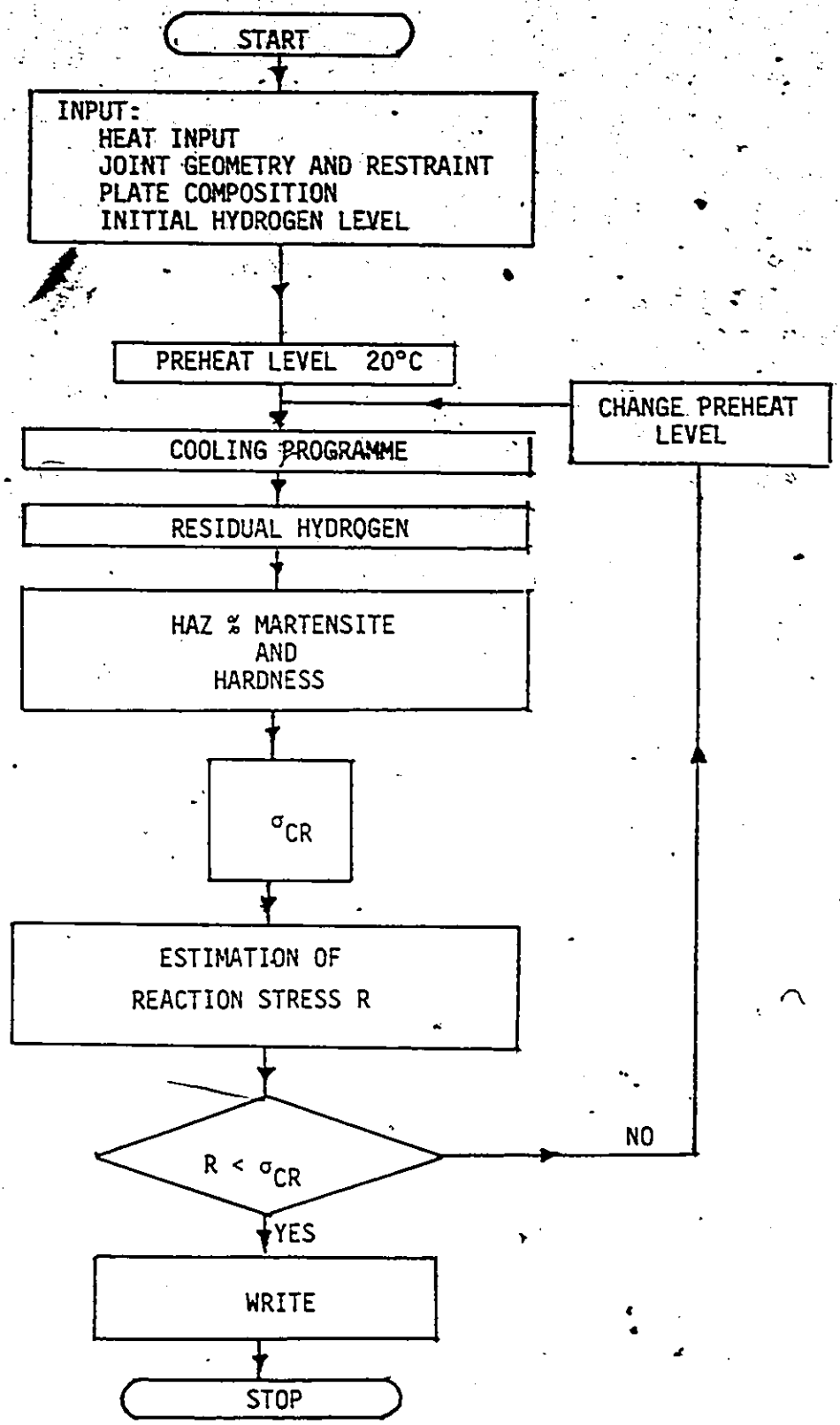

SCHEMATIC FLOW CHART OF THE COMPUTER PROGRAMME

APPENDIX III

IMPLANT TESTING PROCEDURE

1. Clean the notch on the specimen and ensure that the notch distance is appropriate for the heat-input under test.
2. Clean the implant hole in the plate.
3. Place the plate on the welding table such that the implant hole lies above the hole in the welding table platform.
4. Connect the ground cable to the rear right hand corner of the plate.
5. Connect the negative voltmeter lead to the front left hand corner of the plate.
6. Insert the specimen from below, into the plate and hold it in position with the clamp. Ensure that the specimen top is level with the plate surface.
7. Clamp the plate to the welding table.
8. Take out the appropriate electrode from the holding oven.
9. Grind the electrode tip to a cone shape.
10. Clip in the electrode into the appropriate hole in the electrode holding block.
11. Using table and feed controls, position the electrode such that it is just ahead of the specimen.
12. Adjust the electrode holder block to a position such that the electrode tip is approximately 1 mm left of the weld center line.
13. Position the welding table such that the electrode tip is 5 cm

ahead of the specimen.

14. Adjust the initial gap between the electrode tip and the plate to 1.2 mm.

15. Place a copper spacing strip (0.6 mm thick) below the electrode such that the electrode tip is just above the strip edge facing the specimen.

16. Place the line switch to the table and feed controls in "off" position.

17. Set the table and feed controls to the levels appropriate to the heat input under study.

18. Place the table and feed control switches in "forward" position.

19. Ensure that the generator is set for dc reverse polarity and is in appropriate amperage range, with the high frequency arc starter in "start" position.

20. Set the generator for the welding current level necessary for the heat input under study.

21. Place the main power switch for the generator in "on" position.

22. Switch on the generator and wait for 5 minutes.

23. Sit on the chair. Hold the welding shield in your left hand, with your right hand on the line switch for the table and feed controls. Place your right foot lightly over the "on-off" foot switch for the generator.

24. To start the arc, put the line switch for the table and feed controls in the "on" position and simultaneously press the foot switch.

25. Watch the arc through the welding shield. If the arc does not

get established, return the line switch for the table and feed controls to "off" position and release your foot from the foot switch.

26. When the arc becomes steady, note the arc voltage and the welding current.

27. When the arc approaches the plate edge, place the line switch for the table and feed controls in "off" position and release your foot from the foot switch.

28. Switch off the generator and note the time.

29. Place the table control switch in "off" position and feed control switch in "reverse" position.

30. Return the line switch for the table and feed controls to the "on" position. When the electrode butt clears above the plate, push the feed control switch to "off" position.

31. Remove the slag from the weld.

32. Remove the clamps holding the specimen and the plate.

33. Disconnect the negative voltmeter lead wire from the plate.

34. Lift up the plate with gloves on and place two rollers below the plate. Disconnect the ground cable from the plate.

35. Engage the loading bar attachment with the specimen.

36. Put the loading lever through the loading bar slot into the hinge slot.

37. Hold the lever in place by the holding pin.

38. Adjust the hydraulic jack arm such that is just touches the loading lever. Make sure that the loading bar is co-linear with the specimen.

39. Place the micro switch in "on" position and the line switch for the loading system in "off" position.

40. Adjust the gas pressure to the required level.

41. Put on the dc voltage source and increase the voltage to approximately 8.75 volts such that the digital voltmeter reads 14.00 mv.

42. Set the time on the digital clock to 12.00 position.

43. Put the recorder pen in "on" mode with the chart speed set at 300 mm/min.

44. When the time appropriate to the heat input under study has elapsed since the stopping of the arc in Step 28, put chart control "on".

45. Switch the line for the loading system to "on" position.

46. Note the steady voltage read on the digital voltmeter.

47. Allow the test to proceed. When the specimen fractures, the micro switch will be pressed to "off" position, releasing the pressure and stopping the digital clock.

48. Note the time of fracture. Switch the recorder pen and chart control "off".

49. If the specimen fractures before 2 min., calculate the time elapsed between the start of loading and fracture from the distance travelled by the chart.

50. If the specimen does not fracture in 2 min., switch the recorder pen and chart control "off" and allow the test to proceed.

51. If the specimen does not fracture for 24 hours, release the load by switching "off" the line for the loading system.

52. After the test is over (i.e., after fracture or 24 hours of load-

ing), remove the loading lever and loading bar attachments and release the residual pressure in the gas line.

REFERENCES

1. Dearden and O'Neill, H., "A Guide to the Selection and Welding of Low Alloy Structural Steels", Trans. Inst. Weld. (U.K.), Vol.3 (1940), No. 10, 203-214.

2. Kihara, H., Suzuki, H., and Kanatani, F., "Weld Hardening of High Strength Steels and Prediction of Optimum Welding Conditions", Trans. National Research Institute of Metals, 1, (1), 51-76, (1959).

3. Volrich, C.B., Martin, D.C., and Harder, O.E., "Notched Bead Slow Bend Tests of Carbon-Manganese Steels", Welding Journal, 26, (1977), Research Supp., 489S-507S.

4. William, R.D., Roach, D.B., Martin, D.C., and Volrich, C.B., "The Weldability of C-Mn Steels", Welding Journal, 28, (1949), Research Supp., 311S-325S.

5. Volrich, C.B. and Harder, D.E., "Review on WEldability of C-Mn Steels", Welding Journal, 28, (1949), Research Supp. 326S-336S.

6. Sims, C.E. and Banta, H.M., "Development of Weldable High Strength Steels", Welding Journal, 28, (1949), Research Supp., 178S-192S.

7. Reeve, L., "Weldability of N.D. Steels", British Welding Journal, 4, (9), Sept. 1957, 425-432.

8. Cottrell, C., Winterton, K., and Bradstreet, B.J., "The Weldability of High Tensile Structural Steels", Ministry of Supply Report W.R.(D), 1/55 BWRA, May 1956, 79-

9. Cottrell, C., "Assessment of Weldability by Rapid Dialatin Tests", Journal Iron and Steel Institute (U.K.), 173, (1953), 17-24.

10. Bradstreet, B.J., "Arc Welding Low Alloy Steels", British Welding Research Assoc., August 1956.

11. Winterton, K., "Weldability Prediction of Steel Composition to Avoid Heat-Affected Zone Cracking", Welding Journal, June (1961), Research Supp., 253S-258S.

12. Sub-Commission IX G, "Technical Report 1967", IIW DOC. IX, 535-67.

13. Bradstreet, B.J., "Methods to Establish Procedures for Welding Low Alloy Steels", The Engineering Journal, Nov. (1963), 37-41.

14. Bailey, N., "Establishment of Safe Welding Procedures for Steels", Welding Journal, April (1972), Research Supp., 169S-177S.

15. Ito-Bessyo, IIW Sub-Commission IX, IIW DOC. IX, 576-68.

16. Ito-Bessyo, "Prediction of Welding Procedure to Avoid Heat Affected Zone Cracking", IIW Sub-Commission IX, DOC. IX, 631-69.

17. Grajon, H., "The Implant Method for Studying the Weldability of High Strength Steels", Metal Construction and British Welding Journal, No.v (1969), 509-515.

18. Sawhill, J.M., Jr., Dix, A.W., and Savage, W.F., "Modified Implant Test for Studying Delayed Cracking", Welding Journal, Dec. (1974), Research Supp., 554S-560S.

19. Evans, G.M., Simansen, T, and Augland, B., "Implant Weldability Testing of Carbon-Manganese Steels", SINTER Report, Jan. (1970), brief presentation of results in Met. Constr. Br. Weld. J., 2, (1970), 108-109.

20. Evans, G.M., Christensen, N., "Correlation of Weld Metal Hydrogen Content with HAZ Embrittlement", Met. Constr. Br. Weld. J., July (1971), 188-189.

21. Hart, P, and Watkinson, F., "Development and Use of Implanting Cracking Test", Welding Journal, July (1972), 349S-357S.

22. Ronningen, J.A., Simonsen, T., and Christensen, N., "On the Assessment of HAZ Microstructure in C-Mn Steels", Scandinavian Journal of Metallurgy, 2, (1973), 87-90.

23. Evans, G.M. and Christensen, N., "Correlation of Microstructure with HAZ Embrittlement", Scandinavian Journal of Metallurgy, 2, (1973), 91-94.

24. Berry, J.T. and Allan, R.C., "A Study of Cracking Low Alloy Steel Welded Joints", Welding Journal, March (1960), 105S-116S.

25. Pfeil, L.B., Proc. Roy. Soc. London, Vol. A112, (1926), 182.

26. Petch, N.J. and Stables, P., Nature, Vol. 169, (1952), 842.

27. Uhlig, H.H., Corrosion and Corrosion Control, John Wiley, New York, 1963.

28. Zaffe, C. and Sims, C., Trans. A.I.M.E., Vol. 145, (1941), 225.

29. Smialowski, M., Hydrogen In Steel, Addison-Wesley, Reading, Mass. (1962).

30. Tetelman, A.S. and Robertson, W., Trans. TMS-A.I.M.E., Vol. 224, (1962), 775.

31. Tetelman, A.S., Fundamental Aspects of Stress Corrosion Cracking, p.446, NACE, Houston, 1969.

32. Weichselfelder, T., Liebigs Ann. Chem., Vol. 447, (1926), 64.

33. Westlake, D.G., Trans. ASM, Vol. 62, (1969) 1000.

34. Beachem, D.C., "A New Model for Hydrogen-Assisted Cracking (Hydrogen "Embrittlement")", Metallurgical Transactions, Vol. 3, Feb. (1972), 437-451.

35. Johnson, H.H., Morlet, J.G. and Troiano, A.R., "Hydrogen, Crack Initiation and Delayed Failure in Steel", Trans. A.I.M.E., Vol. 212, (1958), 526-536.

36. Private communication with M. Urednicek, Foothills Pipelines (Yukon) Ltd., Calgary, Alberta.

37. Rosenthal, D., "The Theory of Moving Sources of Heat and Its Application to Metal Treatments", Trans. A.I.M.E., Nov. (1946), 849-866.

38. Dorschu, "Control of Cooling Rates in Steel Weld Metal", Welding Journal, Feb. (1968), 49S-62S.

39. Signes, E.G., "A Simplified Method for Calculating Cooling Rates in Mild and Low Alloy Steel Weld Metals", Welding Journal, Oct. (1972), 473S-484S.

40. Graville, B.A., "Weld Cooling Rates and Heat-Affected Zone Hardness in a Carbon Steel", Welding Journal, Sept. (1973), Research Supp., 337S-385S.

41. Jhaveri, P., Moffatt, W.G. and Adams Jr., C.M., "The Effect of Plate Thickness and Radiation on Heat Flow in Welding and Cutting", Welding Journal, January (1962), Research Supp., 12S-16S.

42. Maynier, P., Dollet, J., and Jungmann, B., "Creusot-Loire System for the Prediction of the Mechanical Properties of Low-Alloy Steel Products", Hardenability Concepts with Applications to

Steel, Proceedings of A.I.M.E. Symposium, Oct. 24-26, 1977, 518-544.

43. Satoh, K. et al, "Correlation of the Implant Test With the RRC and the TRC Tests", IIW. DOC. NO. IX, 874-74.

44. Tadaomi, Fujii, "On the Prevention of Hydrogen Induced Weld Cracking in Steel Weldments", IIW DOC. No. IX, 876-74.

45. Bradstreet, B.J., "Effect of Welding Conditions on Cooling Rate and Hardness in the Heat Affected Zone", Welding Journal, Nov. (1969), Research Supp., 499S-504S.

46. Specification for Metal Arc Welding of Carbon and Carbon-Manganese Steels, BS 5135: December (1974), UDC 621, 791.753: [669.14 + 669.15'74-194], British Standards Institution, London, W1A 2BS.

47. Pedder, C., Watkinson, F., "Automatic Deposition of Manual-Metal Arc Covered Electrodes", Welding Institute Research Bulletin, 12, (1971), 253-254.

48. Pedder, C. and Hart, P., "Implant Cracking Test Equipment", Welding Institute Research Bulletin, 12, (1971), 339.